Diss. 2010 - 14
Oktober

Construction and Commissioning of a Collinear Laser Spectroscopy Setup at TRIGA Mainz and Laser Spectroscopy of Magnesium Isotopes at ISOLDE (CERN)

Jörg Krämer

(Dissertation der Johannes Gutenberg-Universität in Mainz)

GSI Helmholtzzentrum für Schwerionenforschung GmbH
Planckstraße 1 · D-64291 Darmstadt · Germany
Postfach 11 05 52 · D-64220 Darmstadt · Germany

Construction and Commissioning of a Collinear Laser Spectroscopy Setup at TRIGA Mainz

and

Laser Spectroscopy of Magnesium Isotopes at ISOLDE (CERN)

Dissertation

zur Erlangung des Grades
"Doktor der Naturwissenschaften"

im Promotionsfach Chemie
am Fachbereich Chemie, Pharmazie und Geowissenschaften
der Johannes Gutenberg-Universität
in Mainz

Jörg Krämer
geb. in Alzey

Mainz, den 22. Juli 2010

Dekan: Prof. Dr. Wolfgang Hofmeister

Erster Berichterstatter: Prof. Dr. Wilfried Nörtershäuser
Zweiter Berichterstatter: Prof. Dr. Klaus Blaum

Tag der mündlichen Prüfung: 07. Oktober 2010

Abstract

Collinear laser spectroscopy has been used as a tool for nuclear physics for more than 30 years. The model-independent extraction of nuclear ground-state properties from optical spectra delivers important physics results to test the predictive power of nuclear models. A study of the isotope shift allows the extraction of the change in the mean square nuclear charge radius as a measure for nuclear size. Odd-proton or odd-neutron number isotopes have a non-vanishing total nuclear angular momentum (spin) and therefore exhibit a hyperfine structure in the electronic transition. The detailed analysis of this property yields the nuclear spin I, the nuclear dipole moment μ, and in special cases also the electric quadrupole moment Q. Collinear laser spectroscopy combines this experimental method with the spectroscopy on fast ion or atom beams, which is ideally suited for the study of short-lived isotopes and can be readily adapted to specific experimental needs.

In this work the construction and the commissioning of a new collinear laser spectroscopy setup at the TRIGA research reactor at the University of Mainz is presented together with the experimental investigation of magnesium isotopes with this experimental method at the COLLAPS beamline at ISOLDE (CERN). In the neutron-rich regime of the magnesium isotopes the limits of the so-called "island of inversion" are situated, which marks a region with a significant amount of intruder configurations mixing to the nuclear ground states and leading to unexpected spins and moments on which the charge radii should shed more light on.

TRIGA-LASER is one of two main branches of the TRIGA-SPEC experiment. The goal of the laser branch is to study the evolution of the nuclear shape around $N \approx 60$ for elements with $Z > 42$. The neutron-rich isotopes will be produced by neutron-induced fission near the reactor core and transported to an ion source by a gas-jet system. The collinear laser spectroscopy beamline will be presented in detail and specified by extensive test measurements. A detection efficiency of 1 photon / 356 atoms is reached and the hyperfine structure and the isotope shift of the two stable rubidium isotopes could be determined with an uncertainty of 7 MHz and are in excellent agreement with literature values.

Besides the nuclear physics investigations the TRIGA-LASER setup serves as a development platform for the future LASPEC experiment at the FAIR facility and for other experiments, e.g. COLLAPS at ISOLDE (CERN) or BECOLA at NSCL (MSU).

The versatility of the collinear laser spectroscopy technique is exploited in the second part of this thesis to gain information on the ground-state properties of Mg isotopes. The nuclear spin and the magnetic moment of the neutron-deficient isotope ^{21}Mg were measured applying optical pumping and β-NMR. The results are in good agreement with shell-model calculations. In the region of the neutron-rich isotopes the isotope shifts of the isotopes $^{24-32}$Mg were determined. Therefore, several different detection methods had to be combined. Besides the classical fluorescence spectroscopy the photon-ion coincidence technique was applied. Furthermore, the β-asymmetry detection was for the first time used for the measurement of the isotope shift at low production rates. This requires a good understanding of the observed line profiles for the β detection to extract the centers of gravity of the hyperfine structures correctly. This allowed for the measurement of the isotope shift of ^{31}Mg with sufficient precision, which has a production rate of only $1.5 \times 10^5\,\mathrm{s}^{-1}$. The radii give an insight in the evolution of nuclear deformation at the transition to the "island of inversion" and will be discussed with respect to nuclear deformation and to nuclear model predictions.

Zusammenfassung

Die kollineare Laserspektroskopie ist seit über 30 Jahren ein wichtiges Instrument für die Untersuchung der Grundzustandseigenschaften kurzlebiger Atomkerne. Die Extraktion dieser Eigenschaften aus optischen Spektren ist kernmodellunabhängig und die so gewonnenen Daten besitzen ein besonders großes Gewicht beim Test der Vorhersagekraft von Kernmodellen. Die Messung der Isotopieverschiebung erlaubt es, die Änderung des mittleren quadratischen Kernladungsradius als Maß für die Kerngröße zu extrahieren. Die Analyse der Hyperfeinstruktur von Atomen ermöglicht die Bestimmung des Kernspins sowie des magnetischen Dipolmoments und des elektrischen Quadrupolmoments. Die kollineare Laserspektroskopie kombiniert diese Untersuchungsmethoden mit der für kurzlebige Isotope sehr günstigen und vielfältig variierbaren Technik der Spektroskopie am schnellen Ionen- bzw. Atomstrahl.

In dieser Arbeit werden der Aufbau und erste Testmessungen einer neuen Apparatur für die kollineare Laserspektroskopie am TRIGA Forschungsreaktor der Universität Mainz vorgestellt und experimentelle Untersuchungen an Magnesiumisotopen mit dieser Methode an der Strahlstrecke COLLAPS an ISOLDE (CERN) präsentiert. Im neutronenreichen Bereich der Magnesiumisotope liegen die Grenzen der "Island of Inversion", welche durch das Vorhandensein von sogenannten "intruder"-Zuständen im Grundzustand der zughörigen Isotope ausgezeichnet ist. Diese Grundzustände führen zu unerwarteten Spins und Momenten, über die die Ladungsradien weiter Aufschluss geben sollen.

TRIGA-LASER ist einer von zwei Zweigen des TRIGA-SPEC Experiments. Ein Ziel des Laserzweigs ist die Untersuchung der Kerndeformation bei $N \approx 60$ für Elemente mit $Z > 42$. Die neutronenreichen Isotope sollen dabei durch neutroneninduzierte Spaltung nahe am Reaktorkern produziert und durch ein Gas-Jet Transportsystem zu einer Ionenquelle transportiert werden. Der Aufbau der kollinearen Strahlstrecke wird hier im Detail vorgestellt und durch ausführliche Testmessungen mit stabilen Rubidiumisotopen spezifiziert. Dabei wird eine Nachweiseffizienz der Fluoreszenzphotonen von 1 Photon/356 Atome erreicht. Die Hyperfeinstruktur und die Isotopieverschiebung der beiden stabilen Rubidiumisotope konnte mit einer Genauigkeit von 7 MHz bestimmt werden und ist in ausgezeichneter Übereinstimmung mit Literaturdaten.

Neben den kernphysikalischen Untersuchungen bei neutronenreichen Kernen, stellt TRIGA-LASER auch eine Entwicklungsplattform für das zukünftige LASPEC Experiment bei FAIR und andere Experimente, z.B. COLLAPS bei ISOLDE (CERN) oder BECOLA am NSCL (MSU) dar.

Die ausgesprochene Vielseitigkeit der kollinearen Laserspektroskopie wird im zweiten Teil dieser Arbeit ausgenutzt, um Informationen über die Grundzustandseigenschaften von Mg Isotopen zu erhalten. Einerseits wurde der Kernspin und das magnetische Moment des neutronenarmen Isotops ^{21}Mg nach optischem Pumpen mittels β-NMR bestimmt. Die Ergebnisse sind in guter Übereinstimmung mit Schalenmodellrechnungen. Im Bereich der neutronenreichen Isotope wurden die Isotopieverschiebungen der Isotope $^{24-32}$Mg bestimmt. Dabei mussten mehrere Nachweismethoden eingesetzt werden: Neben der klassischen Fluoreszenzspektroskopie kam die Photon-Ion Koinzidenz-Methode zum Einsatz. Darüber hinaus wurde erstmals der Nachweis der β-Asymmetrie nach optischem Pumpen für die Messung von Isotopieverschiebungen eingesetzt. Dies setzt ein gutes Verständnis der beobachteten Linienprofile beim Asymmetrienachweis voraus, um die Schwerpunkte der Hyperfeinstruktur korrekt zu extrahieren. Damit konnte die Isotopieverschiebung noch für das Isotop ^{31}Mg mit einer Produktionsrate von $1.5 \times 10^5\,\mathrm{s}^{-1}$ ausreichend genau bestimmt werden. Die gewonnenen Kernladungsradien geben Einblick in die Entwicklung der Kerndeformation beim Übergang in die "Island of Inversion" und werden im Hinblick auf die Vorhersagen bestehender Kernmodelle diskutiert.

Contents

List of Figures

List of Tables

1. Introduction

The nuclear shell model has proven to be well suited for the description of nuclear properties with excellent predictive power for stable nuclear systems. The predictions of the magic numbers, marking shell closures, are experimentally confirmed in many cases. The experimental two-neutron separation energy for example can be used to study the energy level structure and it usually shows a significant drop when a magic neutron number is crossed, corresponding to a larger shell gap at the transition from one shell to the next. The total angular momentum of the unpaired nucleon for the even-odd case or the coupled momentum of the two unpaired nucleons in the case of odd-odd nuclei, referred to as the nuclear spin, can be probed experimentally and in the most cases agrees with the shell-model predictions.

However, in the case of the $N = 20$ magic number, irregularities have been found in different experiments, suggesting that for the elements from $Z = 10 - 13$ the shell gap between the lower *sd*- and the pf-shell is reduced, masking the expected shell closure and giving rise to unexpected spectroscopic data and nuclear properties. First hints came from a mass measurement on neutron-rich sodium isotopes carried out in 1975 by Thibault *et al.* [Thi75] where the extracted two-neutron separation energy did not indicate a shell closure at the $N = 20$ magic neutron number. In this so-called "Island of Inversion" [War90] the neutrons start to fill the pf-shell before the *sd* shell is closed, these configurations are often referred to as intruder configurations. In the case of the magnesium isotopes only these intruder configurations can explain the anomalous spin and magnetic moment of ^{31}Mg and ^{33}Mg determined recently at ISOLDE (CERN) with the collinear laser spectroscopy setup COLLAPS [Ney05, Yor07a]. The isotopes that exhibit intruder configurations in the ground state are marked in the section of the nuclear chart presented in Fig. 1.1

There are two main mechanisms used to explain the lowering of the $\nu\, f_{7/2}$ orbit with respect to the $\nu\, d_{3/2}$ orbit. At first, the spin-isospin interaction between protons and neutrons [Ots01] leads to a lowering of the $\nu\, d_{3/2}$ orbit for the heavier elements because of the attractive interaction with the partially filled $\pi\, d_{5/2}$ orbit, increasing the shell gap to the $\nu\, f_{7/2}$ orbit. For the lighter elements in the island of inversion this interaction is much weaker because less protons are in the $\pi\, d_{5/2}$ orbit, lifting the $\nu\, d_{3/2}$ towards the $\nu\, f_{7/2}$ orbit. A second interaction between protons and neutrons is the tensor force due to a meson exchange [Ots05]. This repulsive interaction between the $\pi\, d_{5/2}$ orbit and the $\nu\, f_{7/2}$ is weak for the constituents of the island of inversion and thus allows the $\nu\, f_{7/2}$ orbit to come lower compared to the heavier isotones which makes particle-hole excitations and mixed ground-state configurations more probable.

Proton-neutron interactions and the strongly-mixed ground-state configurations are also supposed to have an impact on nuclear deformation [Fed79] as a bulk property of the nucleus and are an example for how the shell model can empirically be related to geometrical nuclear properties. The mean squared nuclear charge radius $\langle r^2 \rangle$ is sensitive to static deformations and because of the nuclear-model independent connection to the optical isotope shift in atomic transitions it can be probed by laser spectroscopy with high sensitivity. Laser spectroscopic isotope shift studies in the region of Ne and Na isotopes have been performed earlier at CERN [Gei02, Hub78]. The measurement of the changes in the mean square nuclear charge radii of the magnesium isotopes

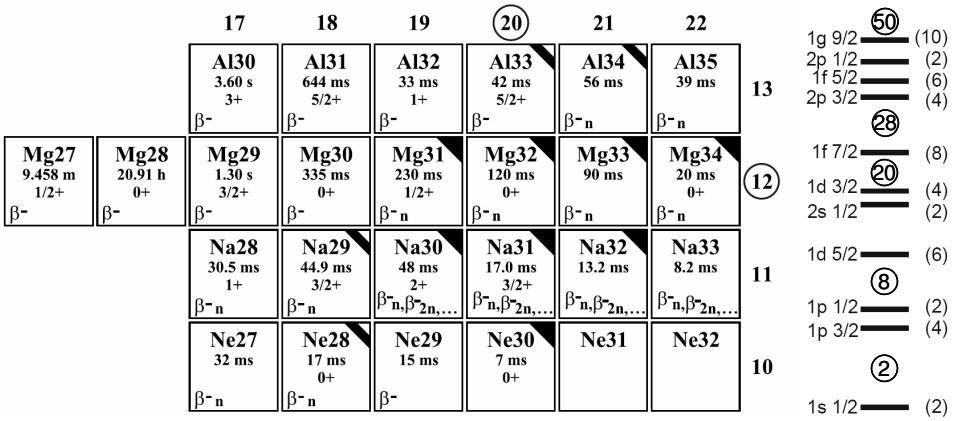

Figure 1.1.: The "Island of Inversion". Isotopes marked with a black triangle in the top right corner show pure intruder ground-state configuration. Mixed configurations are indicated by the black bar. Isotopes outside the region or without conclusive evidence are without mark. The level structure for neutrons up to $N = 50$ is shown to the right. Taken from [Yor07b].

from ^{24}Mg to ^{32}Mg will shed more light on the onset of deformation and the relation of this deformation to their known intruder configurations.

In the region of the medium-heavy elements starting from molybdenum, the $N = 60$ sub-shell gap has been found to be less clear cut than it is for the lighter isotopes. This has recently been shown in a measurement of the charge radii of neutron-rich molybdenum isotopes [Cha09] that show no sudden shape transition from a spherical to a deformed shape and a significantly higher increase in radius when $N = 60$ is approached, but a very gradual change over a broader range from $N = 50 - 60$. This disappearance of a shell gap has also been confirmed for the heavier elements Tc, Ru, Rh, and Pd by the two-neutron separation energy [Aud03].

However, measurements of observables directly related to the nuclear shape have not been performed for these elements, which will become accessible by the induced-fission production scheme at the TRIGA reactor Mainz presented in this thesis. The study of the charge radii and, where existing, the magnetic moments and the spins, will give an insight in the degree of deformation and in how far the shell structure is related to these shape changes by the degree of configuration mixing of the ground state.

This work will give a short introduction to the TRIGA-SPEC experiment currently being set up at the TRIGA research reactor at Mainz and will present in detail the laser spectroscopic branch TRIGA-LASER, for which the experimental ion and atom beam setup was designed and built during this PhD work. The results of laser spectroscopic test measurements for the commissioning of the setup will conclude this part.

The second part of this thesis is devoted to nuclear structure studies of magnesium isotopes carried out at ISOLDE (CERN) with the existing collinear laser spectroscopy setup. The spin and the magnetic moment determination of the neutron-deficient ^{21}Mg is presented and discussed. Furthermore, charge radii along the isotope chain $^{24-32}$Mg are evaluated from isotope-shift measurements and the results will be discussed and compared to theory in terms of the liquid droplet model.

2. Theory

This section will give the main theoretical background and the basis for the experimental part of this thesis and the discussion of the results.

2.1. Atomic Physics and Laser Spectroscopy

The experimental method described in this thesis shows in an impressive way the link between atomic and nuclear physics. At first glance, laser spectroscopy is a probe for the atomic structure and therefore restricted to the extraction of observables referring to the electronic states of the atom. However, electron-nucleus interactions, beyond the point-nucleus Coulomb potential, modify the atomic properties in a subtle way. Laser spectroscopy is sensitive to these changes and allows to extract nuclear structure information.

2.1.1. Hyperfine Structure

The main contribution to the hyperfine structure is a splitting and an energy shift of the electron levels because of the interaction of the electrons with the nuclear-spin induced magnetic dipole moment of the nucleus which is defined as

$$\mu_I = g_I \mu_N I/\hbar\,, \tag{2.1}$$

with the nuclear total angular momentum I and the nuclear magneton $\mu_N = e\hbar/2m_p$, where m_p denotes the proton mass. The nuclear g factor relates the experimental magnetic moment to the expected magnetic moment of a structureless point particle with spin I. Together with the electron total angular momentum J (spin+orbit) a new coupled angular momentum

$$\vec{F} = \vec{I} + \vec{J} \tag{2.2}$$

can be defined [Her08]. Let the states $|Im_I\rangle$ and $|Jm_J\rangle$ be the eigenstates of the operators $\hat{I}^2$ and $\hat{J}^2$ and of the z components $\hat{I}_z$ and $\hat{J}_z$ fulfilling the eigenvalue relations

$$\hat{I}^2\,|Im_I\rangle = \hbar^2 I\,(I+1)\,|Im_I\rangle \tag{2.3}$$

and

$$\hat{I}_z\,|Im_I\rangle = \hbar m_I\,|Im_I\rangle \tag{2.4}$$

and the same with J instead of I for the electron shell eigenstates. According to the theory for the coupling of angular momenta the coupled eigenstates can be derived from the individual states by the Clebsch-Gordan expansion [Sch00]

$$|I, J, Fm_F\rangle = \sum_{m_I m_J} (Im_I, Jm_J|Fm_F)\,|Im_I\rangle\,|Jm_J\rangle\ , \tag{2.5}$$

with the Clebsch-Gordan (CG) coefficients

$$C^{IJF}_{m_I m_J m_F} = (Im_I, Jm_J|Fm_F)\ . \tag{2.6}$$

From the general rules for the CG coefficients follows

$$F = |J - I|, |J - I| + 1, \cdots J + I, \tag{2.7}$$

which can be easily interpreted as vector addition of the two angular momenta. The Hamilton operator describing the atomic system can now be written as the sum of the undisturbed Hamiltonian plus the contribution from the magnetic dipole interaction

$$\hat{H} = \hat{H}_0 + \hat{H}_{\mathrm{mHFS}}. \tag{2.8}$$

Where the index $_{\mathrm{mHFS}}$ denotes "magnetic hyperfine structure" and emphasizes that only the magnetic contribution is taken into account. The orbital motion and the intrinsic spins of the electrons produce a mean magnetic field at the location of the nucleus $\hat{B} = -\beta_J \hat{J}/\hbar$ and thus the interaction energy with the nuclear magnetic moment becomes

$$\hat{H}_{\mathrm{mHFS}} = -\hat{\mu}_I \cdot \hat{B}_J = g_I \mu_N \beta_J \frac{\hat{I} \cdot \hat{J}}{\hbar^2}. \tag{2.9}$$

Since the coupled states $|I, J, Fm_F\rangle$ are neither eigenstates of the I nor of J but of I^2 and J^2 one can use the definition

$$\hat{F}^2 = \left(\hat{I} + \hat{J}\right)^2 = \hat{I}^2 + \hat{J}^2 + 2\hat{I} \cdot \hat{J} \tag{2.10}$$

to replace the operator product $\hat{I} \cdot \hat{J}$ and to obtain the final result for the hyperfine Hamiltonian

$$\hat{H}_{\mathrm{mHFS}} = g_I \mu_N \beta_J \frac{\hat{F}^2 - \hat{I}^2 - \hat{J}^2}{2\hbar^2}. \tag{2.11}$$

Letting this Hamiltonian act on the $|Fm_F\rangle$ eigenstates yields the eigenvalues of each of the operators

$$\hat{H}_{\mathrm{mHFS}} |Fm_F\rangle = \Delta E |Fm_F\rangle = \frac{A}{2} \left(F(F+1) - I(I+1) - J(J+1)\right) |Fm_F\rangle, \tag{2.12}$$

with the hyperfine A factor

$$A = \frac{g_I \mu_N B}{J} \hbar. \tag{2.13}$$

The result is an energy shift ΔE to the total energy of the electron depending on the quantum numbers F,I and J. An example for an energy level diagram showing how the degeneracy of the states with different angular momenta is lifted because of the spin-orbit interaction (fine structure) and the interaction with the nuclear magnetic moment (hyperfine structure) is shown in Fig. 2.1 for a sodium atom.

Nuclei with angular momenta $I \geq 1$ can exhibit a spectroscopic quadrupole moment Q_s which leads for electronic states with $J \geq 1$ to an electric hyperfine interaction. However, for the experiments discussed in this thesis it is not of relevance.

2.1.2. Isotope Shift

The isotope shift was discovered experimentally in 1932 [Ure32] as a shift in the line positions of characteristic spectral lines between two isotopes of a specific element defined as $\delta\nu^{A,A'} = \nu^{A'} - \nu^{A}$. This effect can be explained if the approximation of an infinitely heavy and point-like nucleus is abandoned. Two contributions add to the total isotope shift: The mass shift and the field shift.

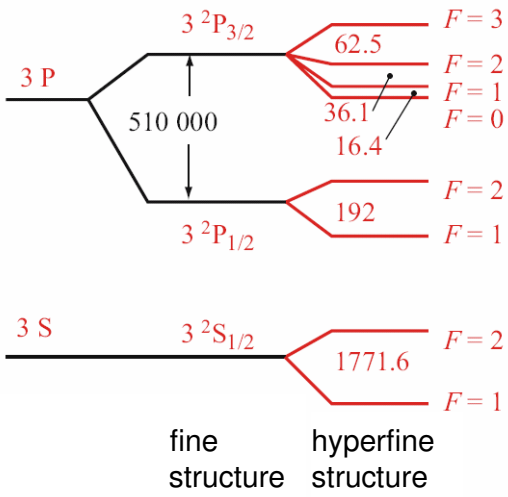

Figure 2.1.: Energy level diagram of the lowest lying electronic states of a Na atom with nuclear spin $I = 3/2$ [Her08]. The numbers for the splittings are given in MHz. The diagram is not to scale. The hyperfine splitting is scaled up.

Mass Shift

The effect of the reduced mass of the electron-nucleus system on the solutions of the Schrödinger equation leading to a center-of-mass motion is referred to as the "normal mass shift" (NMS). The reduced mass enters the Hamilton operator linearly and thus leads to a linear shift in the energy level or the transition frequency ν. The relative shift between the isotopes with mass numbers A and A' is

$$\frac{\delta\nu}{\nu} \propto \frac{\mu' - \mu}{\mu'} = 1 - \frac{\mu}{\mu'}\,, \tag{2.14}$$

with the reduced mass $\mu = \frac{m_e}{1+\frac{m_e}{M}}$, where m_e is the electron mass and M the mass of the nucleus. Eq. 2.14 can be modified to

$$\frac{\delta\nu}{\nu} = \frac{\frac{m_e}{M} - \frac{m_e}{M'}}{1 + \frac{m_e}{M}} \approx m_e \frac{M' - M}{M'M}\,, \tag{2.15}$$

with the approximation that $m_e/M \ll 1$ and thus negligible in the denominator. Therefore the normal-mass shift contribution is

$$\delta\nu_{\mathrm{NMS}} = k_{\mathrm{NMS}} \frac{M' - M}{MM'}\,, \tag{2.16}$$

with the normal mass shift constant $k_{\mathrm{NMS}} = -\nu m_e$.

The calculation of the specific mass shift is not straightforward, it originates in many-electron systems from the fact that one center-of-mass motion solely gives an incomplete description of the whole system. The Hamilton operator needs to be adapted and additional mass polarization terms of the form

$$\hat{H}_{mp} = \frac{1}{M} \sum_{j<k} \hat{p}_j \cdot \hat{p}_k \tag{2.17}$$

have to be added [Dra06], where $\hat{p}_j$ is the momentum of the j th electron. This is quite obvious in the case of a two-electron system, where the kinetic energy is proportional to $(\hat{p_1} + \hat{p_2})^2 =$

$\hat{p_1}^2 + \hat{p_2}^2 + 2\hat{p_1} \cdot \hat{p_2}$. The first two terms are responsible for the normal mass shift while the last term is the mass-polarization term giving rise to the so-called specific mass shift (SMS). An accurate calculation of this contribution is very complicated also for atoms with a single valence electron as it is the case in our experimental work. The mass dependence of the specific mass shift is the same as for the NMS:

$$\delta\nu_{\mathrm{SMS}} = k_{\mathrm{SMS}} \frac{M' - M}{MM'} \,. \tag{2.18}$$

Field Shift

Due to the finite size of the nucleus the electrostatic potential felt by the electrons which have a high probability density at the nucleus, particularly the s electrons, is no longer strictly $\propto 1/r$. This field shift is to first order expressed by

$$\delta\nu_{FS} = F \times \delta \left\langle r^2 \right\rangle^{A,A'} \tag{2.19}$$

and is proportional to the change in the mean-square nuclear charge radius from one isotope to the other and to the electronic factor F, which describes the change in the electron density at the nucleus $\Delta \left|\psi\left(0\right)\right|^2$ between the initial state and the final state of an atomic transition. From perturbation theory follows

$$F = -\frac{Ze^2}{6\epsilon_0} \Delta \left|\psi\left(0\right)\right|^2 \,, \tag{2.20}$$

which is an excellent approximation for light and medium-heavy atoms. The measurement of the isotope shift therefore provides a unique tool to extract information on the nuclear size in a nuclear model-independent way.

However, care has to be taken how the electronic factor F and the specific mass shift constant k_{SMS} are derived. Purely theoretical calculations are often not sufficiently accurate even for simple atomic systems and therefore one has to rely on the combination of different experimental approaches and a special combined analysis, for example the King plot with radii from muonic atom experiments [Fri92]. Moreover, for heavy nuclei the electron density cannot be assumed constant across the whole nucleus and, thus, higher-order radial moments are not negligible any more.

2.1.3. Atoms in External Magnetic Fields

Closely related to the hyperfine structure, the magnetic interaction between the nucleus and the electron shell, is the interaction with external magnetic fields. The energy correction to the hyperfine energy due to a weak magnetic field will be derived in analogy to the description of the hyperfine structure itself. The evolution of the atomic levels in strong magnetic field will be discussed with the Breit-Rabi formula for arbitrary field strengths.

Weak Magnetic Fields - Zeeman Effect

With a weak external field, the hyperfine structure Hamiltonian from Eq. 2.11 is disturbed by

$$\hat{H}_{\mathrm{mag}} = g_J \mu_B \frac{\hat{J}_z}{\hbar} B. \tag{2.21}$$

The matrix element for first order perturbation theory is then defined as

$$g_J \mu_B \left\langle F m'_F \right| \frac{\hat{J}_z}{\hbar} \left| F m_F \right\rangle B \,, \tag{2.22}$$

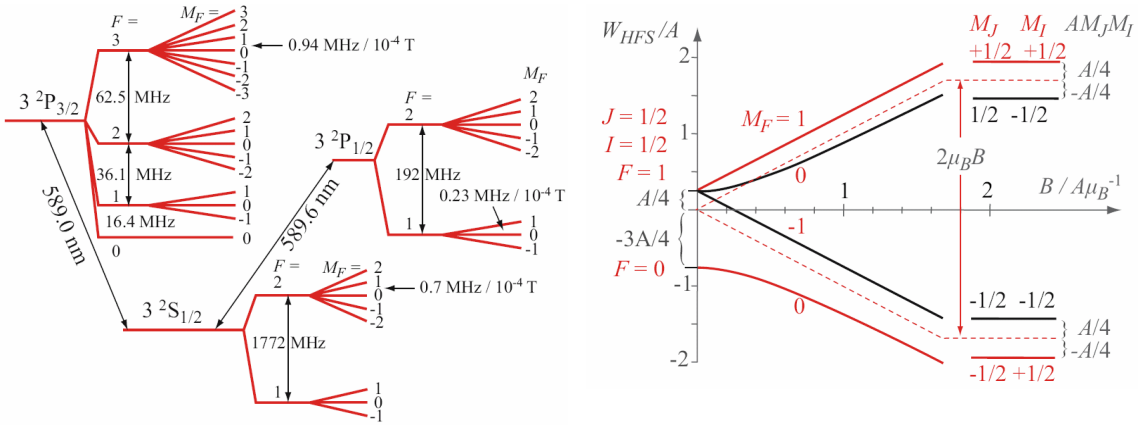

Figure 2.2.: Energy level diagram of the Na D lines in a weak magnetic field to the left. Transition from the weak to strong fields to the right with an energy scale in units of the hyperfine A factor [Her08].

with the eigenstates of the hyperfine operator from Eq. 2.5. Using the projection theorem based on the Wigner-Eckart theorem one can write [Her08]

$$g_J \langle Fm'_F| \frac{\hat{J}_z}{\hbar} |Fm_F\rangle = \frac{\langle Fm_F| \hat{J}\cdot\hat{F} |Fm_F\rangle}{F(F+1)\hbar^2} \langle Fm'_F| \hat{F}_z |Fm_F\rangle = g_F m_F \,. \tag{2.23}$$

Here the binomial relation

$$\hat{J}\cdot\hat{F} = \frac{\hat{F}^2 + \hat{J}^2 - \hat{I}^2}{2} \tag{2.24}$$

and the known eigenvalues from Sec. 2.1.1 were used. The g_F factor is defined as

$$g_F = g_J \frac{F(F+1) + J(J+1) - I(I+1)}{2F(F+1)}. \tag{2.25}$$

The Zeeman shift in a weak external magnetic field becomes now

$$\Delta E_{\text{Zee}} = g_F \mu_B B m_F \,. \tag{2.26}$$

The effect of the Zeeman splitting on a typical atomic level scheme is shown in Fig. 2.2

In the strong field limit (Paschen-Back regime) the coupling between I and J breaks down because the interaction energy with the external field exceeds the hyperfine coupling energy. Now the energy splitting is dominated by the interaction of the electron magnetic moment $g_J \mu_B B m_J$ on which the small correction caused by the nuclear magnetic moment $g_I \mu_N B m_I$ is superposed.

Arbitrary Field Strength - Breit-Rabi Formula

The level shift in an arbitrarily strong external magnetic field can be derived with a similar approach but one has also to take the interaction of the nuclear spin I with the external field into account. In the case of $J = 1/2$ this can be solved analytically and the result is the Breit-Rabi formula

$$W_\pm = \frac{A}{4} \pm \frac{A}{2}\sqrt{1 + \frac{8m_F}{2I+1}\mu_B\frac{B}{A} + \left(2\mu_B\frac{B}{A}\right)^2}\,, \tag{2.27}$$

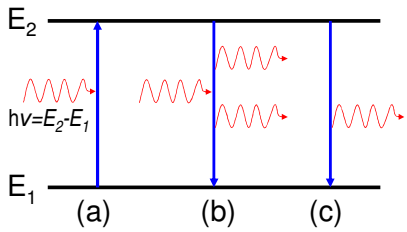

Figure 2.3.: Interaction of a two-level system with a laser. The processes are: (a) induced absorption, (b) induced (or stimulated) emission, (c) spontaneous emission of a photon.

which combines the cases for the weak and the strong field and is also exact in the intermediate region. The positive sign has to be used for the $m_J = 1/2$ case and the negative sign applies for the $m_J = -1/2$ case. The evolution of the m_F levels as a function of the magnetic field is shown in Fig. 2.2.

2.1.4. Rate Equations and the Interaction of Atoms with Laser Light

If we consider a simple two-level electronic system, which is a valid first-order approximation for many transitions, the interaction with the radiation field from a laser can be described by a rate model. The processes that occur are shown schematically in Fig. 2.3. The probability for the absorption of a photon per time unit is proportional to the spectral energy density $\rho(\nu)$ of the radiation field, *i.e.*, the number of photons with the energy $h\nu = E_2 - E_1$ at the atomic site:

$$p_{12} = B_{12}\rho(\nu) \,, \tag{2.28}$$

with the Einstein A coefficient B_{12} of the induced absorption. The spectral energy density $\rho(\nu)$ is given by Planck's radiation law [Dem93].

$$\rho(\nu) = \frac{8\pi\nu^2}{c^3}\frac{h\nu}{e^{h\nu/kT} - 1} \,. \tag{2.29}$$

An excited atom can be stimulated by an already existing photon to emit another photon which increases the number of photons in the relevant mode by one. In analogy to the absorption and with the Einstein coefficient of the induced emission, the probability is

$$p_{21} = B_{21}\rho(\nu) \,. \tag{2.30}$$

The third process does not require an interaction with the field and is explained in terms of QED by interactions with a vacuum field that lead to a decay of the excited state [Her08]. The probability for this spontaneous emission is given by the Einstein coefficient

$$p_{21}^{sp} = A_{21} \,. \tag{2.31}$$

In the steady state of a closed two-level scheme the absorption rate must be equal to the total emission rate giving the rate equation

$$A_{21}N_2 + B_{21}\rho(\nu)N_2 = B_{12}N_1\rho(\nu) \tag{2.32}$$

where N_i is the number of atoms in the state E_i. The population numbers N_i follow the Boltzmann distribution for thermal equilibrium

$$N_i \propto g_i e^{-E_i/kT}\,, \tag{2.33}$$

with the statistical weight g_i of the state E_i being a measure for the degeneracy of the state with respect to other quantum numbers, like angular momenta, for example. Using this distribution in the rate equation allows to extract important relations for the Einstein coefficients:

$$B_{12} = \frac{g_2}{g_1} B_{21} \tag{2.34}$$

and

$$A_{21} = \frac{8\pi h\nu^3}{c^3} B_{21}\,. \tag{2.35}$$

The number of atoms in the state i decaying to the ground state k per time interval dt in the absence of a light field is given by

$$dN_i = -A_{ik} N_i dt\,. \tag{2.36}$$

The solution for this differential equation is an exponential decay

$$N_i = N_{i0} e^{-t/\tau} \tag{2.37}$$

with the life time

$$\tau_i = 1/A_{ik}\,. \tag{2.38}$$

The natural linewidth of this fluorescence process, which can be deduced by treating the atom in a classical oscillator model, is a Lorentz profile

$$I_L(\omega) = I_0 \frac{\delta\nu_n/\pi^2}{4(\nu-\nu_0)^2 + (\delta\nu_n)^2} \tag{2.39}$$

with a linewidth (FWHM=full width half maximum)

$$\delta\nu_n = \frac{1}{2\pi\tau_i}\,. \tag{2.40}$$

Doppler Broadening

The observed resonance lines in laser spectroscopy are usually subject to various broadening mechanisms with the Doppler broadening, due to the thermal energy distribution in the atomic ensemble, often as the dominant case. While the natural linewidth of an allowed dipole transitions from the ground state is typically of the order of a few ten MHz, laser spectroscopy on atomic gases at room temperature can result in observed resonances with a width of a few GHz. The laser frequency ν_L to excite a single atom in a gas with the velocity $\vec{v}$ with $|\vec{v}| \ll c$ is Doppler shifted against ν_0, the resonance frequency at rest, according to

$$\nu_L = \nu_0 + \vec{k}\cdot\vec{v}/2\pi\,, \tag{2.41}$$

where $\vec{k}$ with $\left|\vec{k}\right| = 2\pi/\lambda$ is the wave vector of the laser light. Let the wave vector be oriented along the z axis. The velocity distribution of a thermal gas in one dimension is then given by a Boltzmann distribution

$$n(v_z)\,dz \propto e^{-(v_z/v_w)^2} dv_z\,, \tag{2.42}$$

with the most probable velocity $v_w = (2kT/m)^{1/2}$. v_z can now be expressed by the velocity in Eq. 2.41 and the result is the number of atoms that absorb light in the frequency interval $[\nu, \nu + d\nu]$, which is proportional to the emitted light intensity

$$I_G(\nu) = I_0(\nu_0)\, e^{-\left(c\frac{\nu-\nu_0}{\nu_0 v_w}\right)^2}. \tag{2.43}$$

This is a Gaussian profile with a Doppler width, the FWHM of the Gauss profile, given by

$$\delta\nu_D = \frac{2\pi\nu}{c}\sqrt{8kT\ln 2/m}\,. \tag{2.44}$$

If one additionally allows the atoms with a certain velocity to absorb and to emit photons not only at a fixed Doppler shifted frequency but according to the natural linewidth of the state, then the resulting line profile describing a Doppler broadened transition is a convolution of a Lorentz profile and a Gaussian profile [Dem93], a so-called Voigt profile

$$I_V = \int I_G\left(\nu'\right) I_L\left(\nu - \nu'\right) d\nu'\,. \tag{2.45}$$

Selection rules for Optical Transitions

In the analysis of experimental spectra it is necessary to assign the individual resonances to atomic transitions, for example to extract the center of gravity of the hyperfine spectrum. Selection rules facilitate the work considerably by limiting the number of possible transitions in a given atomic system excited by a laser with known polarization. The fact that the photon is a boson with spin $s_{\mathrm{ph}} = 1$ allows to apply the rules for the coupling of angular momenta as discussed in Sec. 2.1.1 with the consequence that for a given state with angular momentum quantum number j_a only states with the quantum numbers $j_b = j_a \pm 1$ or $j_b = j_a$ can be accessed. Transitions between states $j_a = j_b = 0$ are forbidden.

The projections of the angular momenta obey the following rules, depending on the polarization of the laser light [Her08]:

- $\Delta m = 0$; π light, linear polarization
- $\Delta m = +1$; σ^+ light, left circular polarization
- $\Delta m = -1$; σ^- light, right circular polarization.

2.1.5. Optical Pumping with Lasers and Atomic Polarization

Optical pumping is the process of selective population or depopulation of atomic states, deviating from the occupation in thermal equilibrium, by successive absorption and emission of photons. The interaction with circularly polarized σ light in a hyperfine transition populates projection states of angular momenta with the highest m_F value (σ^+) or the lowest m_F (σ^-) and depopulates all other states with originally thermal occupation. In Fig. 2.4 the process is shown for σ^+ light. As the m_F denotes the projection of the angular momentum $\vec{F}$ onto the quantization axis defined by an external magnetic field, $\vec{F}$ then has a defined orientation concerning the direction of the magnetic field and the $\vec{k}$ vector of the incident light. The atom is *polarized*. The rate equations for the change in the ground-state population $N_i(F_g, m_{F,i})$ in the optical pumping process applied in this work are given by

$$\frac{d}{dt}N_i(F_g, m_{F,i}) = \sum_i P(F_g, m_{F,i}, F_j, m_{F,j})\,(N_j - N_i) + \sum_j A_{ij}N_j\,. \tag{2.46}$$

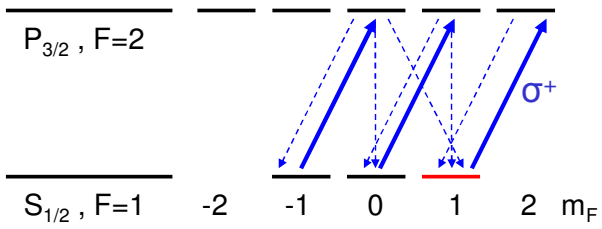

Figure 2.4.: Optical pumping with σ^+ light. The excitation follows the selection rule $\Delta m_F = +1$, while the states can decay to substates with $\Delta m_F = \pm 1$ or 0.

Here $P\left(F_g, m_{F,i}, F_j, m_{F,j}\right)$ is the probability for induced absorption or emission and A_{ij} is the spontaneous decay probability of the excited state j with population N_j. The polarization of the coupled angular momentum $\vec{F}$ leads inherently to a nuclear polarization which can be decoupled from the atomic shell by switching on a strong external magnetic field (Paschen-Back effect). The effect of this nuclear polarization on the β decay will be discussed in the next section.

2.2. Nuclear Physics - Nuclear Ground State Properties

Laser spectroscopic studies on exotic isotopes reveal important information on nuclear ground state properties like spins, nuclear magnetic moments and electric quadrupole moments. The definitions and the basic models describing these physical quantities will be summarized in this section.

2.2.1. The Nuclear Shell Model

Experimental hints like the discrete energy of γ rays emitted from excited nuclei and the existence of "magic numbers", *i.e.* neutron or proton numbers at which the separation energy or the excitation energy for a nucleon is large compared to neighboring nuclei, suggest a shell structure of the nucleus in analogy to the atomic structure. However, the nucleons do not move in a central Coulomb potential but in an effective mean field produced by the nucleons. One possible potential to describe the mean interaction between the nucleons in a spherical nucleus is the Woods-Saxon potential [Pov06]

$$V_{\text{centr}}\left(r\right) = \frac{-V_0}{1 + e^{(r-c)/a}}, \tag{2.47}$$

deduced from the two-parameter Fermi distribution for the nuclear matter. The parameters c and a describe the size and the skin thickness of the nucleus as it will be discussed in Ch. 2.2.2. The solution of the Schrödinger equation for this potential leads to discrete energy levels described by the set of quantum numbers nl_j. As nucleons have an intrinsic spin of 1/2 an additional spin-orbit interaction term has to be added to the potential. While the spin-orbit term in atomic physics causes only small corrections to the energy given by the main quantum number N, the $\hat{l} \cdot \hat{s}$ term in nuclear physics leads to correction of the same order of magnitude as the main quantum number. This results in new shell closures that very successfully describe the observed magic numbers. The properties of the nucleus can now be explained by the properties of individual nucleons outside closed shells. The nuclear spin of odd-A nuclei for example is given by the total angular momentum of the unpaired nucleon. For odd-odd nuclei the angular

momenta of the unpaired proton and the unpaired neutron can couple to a total spin I which is resricted by

$$|I_p - I_n| \leq I \leq I_p + I_n \,, \tag{2.48}$$

according to the coupling rules for angular momenta.

For the description of deformed nuclei the Nilsson model [Nil55] has proven to be a very good model to study the evolution of single-particle orbitals with increasing deformation. An anisotropic harmonic oscillator potential is used to describe the mean field with deformation

$$V_N = \frac{m}{2}\left(\omega^2\left(x^2+y^2\right)+\omega_z^2 z^2\right) + C\left(\hat{l}\hat{s}\right) + D\hat{l}^2 \,, \tag{2.49}$$

with the modified frequency

$$\omega_z^2 = \omega_0^2\left(1-\frac{4}{3}\epsilon_2\right) \,. \tag{2.50}$$

The parameter ϵ_2 describes the nuclear deformation and can be transformed into the commonly used β parameter. The single-particle states as a function of the deformation are shown in Fig. 2.5. Negative deformation parameters refer to an oblate deformation while positive deformation parameters denote prolately deformed nuclei. For vanishing deformation, the level structure from the spherical shell model is reproduced. The individual levels are assigned by their projection of the single-particle angular momentum Ω^π with parity π, the principal quantum number of the major shell N, and the number of nodes of the z-axis wavefunction n_z.

2.2.2. The Nuclear Charge Radius

The nuclear charge radius was already mentioned in Ch. 2.1.2 in the field-shift contribution of the isotope shift. Formally, the mean square nuclear charge radius is defined as [Pov06]

$$\left\langle r^2 \right\rangle = 4\pi \int_0^\infty r^2 \rho\left(r\right) r^2 dr \,, \tag{2.51}$$

with the radial charge distribution of the protons $\rho\left(r\right)$. For the description of medium-heavy nuclei the two parameter Fermi distribution

$$\rho\left(r\right) = \frac{\rho\left(0\right)}{1+e^{(r-c)/a}} \tag{2.52}$$

gives good agreement with experimental radii. At the radius $r = c$ the charge density reaches half of the total value. An empirical value for a spherical nucleus with mass A is

$$c = 1.12\,\mathrm{fm}\, A^{1/3} \,. \tag{2.53}$$

For deformed nuclei with quadrupole deformation parameter β the half-density radius can be parametrized as

$$c = R_0\left(1+\beta Y_{20}\left(\Theta,\Phi\right)\right) \,, \tag{2.54}$$

with the monopole radius R_0 and the spherical harmonic $Y_{20}\left(\Theta,\Phi\right)$. The parameter a is connected to a skin thickness t, which is the distance on which the charge density varies from 90% to 10% of the maximum value via

$$a = \frac{t}{2\ln 9} \,. \tag{2.55}$$

Fig. 2.6 shows the two parameter Fermi distribution for a medium-heavy nucleus.

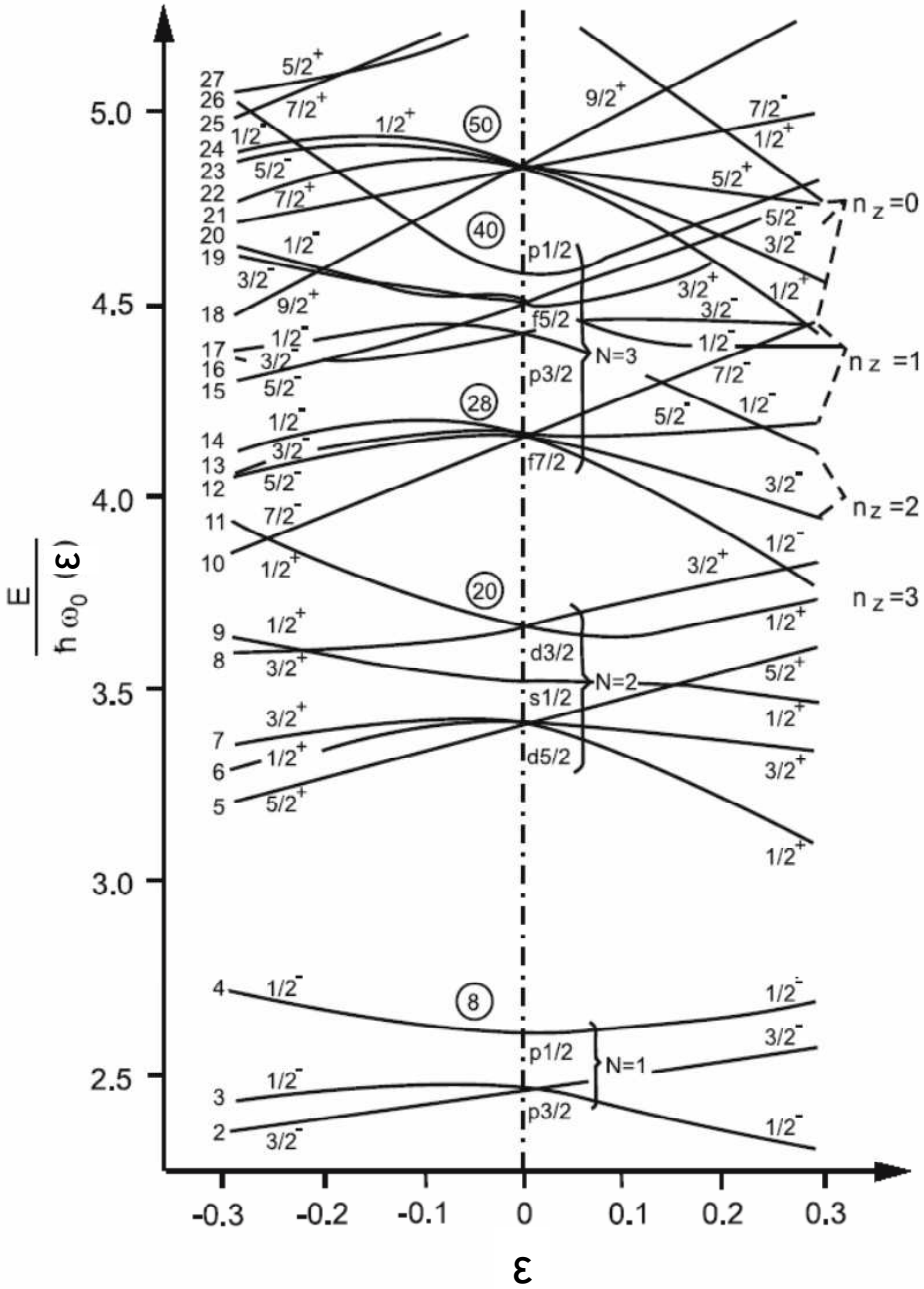

Figure 2.5.: Single-particle levels in the Nilsson model [Bet08]. The deformation lifts the degeneracy of different angular momentum projections on the z axis. The deformation is oblate for $\epsilon < 0$ and prolate for $\epsilon > 0$. Without deformation ($\epsilon = 0$) the spherical shell model is reproduced.

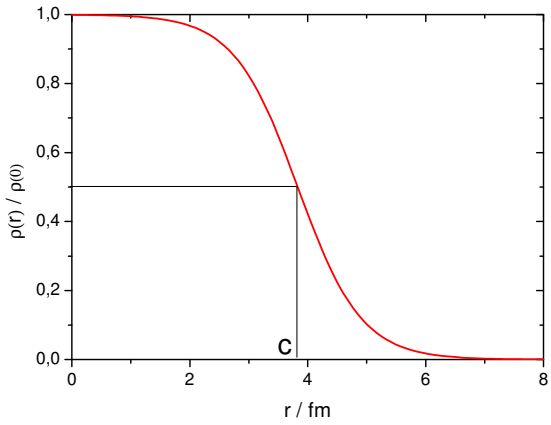

Figure 2.6.: Fermi distribution of the nuclear charge for $A = 40$ and a skin thickness of $t = 2.37\,\mathrm{fm}$.

2.2.3. Nuclear Moments

The magnetic dipole moment μ and the electric quadrupole moment Q of the nucleus are important observable quantities accessible with different experimental techniques and predicted by nuclear models.

Magnetic Dipole Moment

In the classical picture the motion of a charged particle causes a magnetic field with a vector potential [Bet08]

$$\vec{A}(\vec{r}) = \frac{\mu_0}{4\pi} \int \frac{\vec{j}(\vec{r}')}{|\vec{r} - \vec{r}'|} d^3r' \,, \tag{2.56}$$

with the current density $\vec{j}(\vec{r})$ of the charged particle motion. The potential can be rewritten with the multipole expansion

$$\frac{1}{|\vec{r} - \vec{r}'|} = \frac{1}{r} \sum_{l=0}^{\infty} \left(\frac{r'}{r} \right)^l P_l(\cos\alpha) \,, \tag{2.57}$$

where the P_l denote the Legendre polynomials. The first non-vanishing term of this expansion is the dipole term ($l = 1$), which can be expressed as

$$\vec{A}(\vec{r}) = \frac{\mu_0}{4\pi} \frac{\vec{\mu} \times \vec{r}}{r^3} \,. \tag{2.58}$$

$\vec{\mu}$ is the magnetic dipole moment defined as

$$\vec{\mu} = \frac{1}{2} \int \left(\vec{r} \times \vec{j}(\vec{r}) \right) d^3r \,. \tag{2.59}$$

For the motion of charged particles with the mass m the current density can be expressed by the charge density $\rho(\vec{r})$ and the linear momentum $\vec{p}(\vec{r})$ by

$$\vec{j}(\vec{r}) = \frac{\rho(\vec{r})\,\vec{p}(\vec{r})}{m} \,. \tag{2.60}$$

Inserting this in Eq. 2.59 the magnetic moment gets connected to the angular momentum $\vec{L}(\vec{r}) = \vec{r} \times \vec{p}(\vec{r})$:

$$\vec{\mu} = \frac{1}{2} \int \rho\left(\vec{r'}\right) \frac{\vec{L}(\vec{r'})}{m} d^3r' \,. \tag{2.61}$$

The quantum mechanical analogon, the magnetic dipole operator $\hat{\mu}$, is defined as

$$\hat{\mu} = \frac{e}{2m} \int \psi^*(r)\, \hat{L}\psi(r)\, d^3r \,. \tag{2.62}$$

In the case of the nucleus, $\hat{\mu}$ is composed of a contribution from the orbital angular momentum $\vec{l}$ and the nucleonic spin $\vec{s}$. In the single-particle model (Schmidt model) only the quantum numbers of the unpaired nucleon determine the magnetic moment and a g_s factor needs to be defined to connect the intrinsic spins of the nucleons to a classical angular momentum and, hence, to their magnetic moments. The g_l factor is only introduced to distinguish between protons and neutrons. The magnetic moment is now given as

$$\hat{\mu} = \mu_N \left(g_l \hat{l} + g_s \hat{s}\right) \,, \tag{2.63}$$

with the g factors in units of the nuclear magneton $\mu_N = \frac{e\hbar}{2m_p}$ [Pov06]:

- $g_l(p) = 1 \quad g_s(p) = 5.58522$
- $g_l(n) = 0 \quad g_s(n) = -3.8256\,.$

For a nucleus with the coupled angular momentum $\hat{I} = \hat{L} + \hat{S}$ and the eigenstates $|Im_I\rangle$ the expectation value is

$$\mu_{\text{nucl}} = \frac{\mu_N}{\hbar} \langle\psi_{\text{nucl}}|\, g_l \hat{l} + g_s \hat{s}\, |\psi_{\text{nucl}}\rangle \tag{2.64}$$

which can be rewritten with the Wigner Eckart theorem [Pov06] to

$$\mu_{\text{nucl}} = \frac{\mu_N}{\hbar^2} g_{\text{nucl}} \left\langle \hat{I} \right\rangle \,, \tag{2.65}$$

with the nuclear g factor g_{nucl}. The magnetic moment as an observable is the value obtained for the maximum projection of the nuclear spin with $M_I = I$. In the single-particle model the magnetic moment then reduces to

$$\mu_{\text{nucl}} = \mu_N \left(g_l \pm \frac{g_s - g_l}{2l+1}\right) I, \;\; I = l \pm 1/2\,. \tag{2.66}$$

The values obtained by this model can be regarded as boundaries for the observed experimental values. In most nuclei the ground state is not defined by only one configuration, correlations and mixing between different configurations have to be taken into account and also contribute to the magnetic moment.

Electric Quadrupole Moment

In analogy to the treatment of the current density of the moving charges in the nucleus to derive the magnetic moment, the multipole expansion of the scalar potential $\Phi(\vec{r})$ with the charge density $\rho(\vec{r})$ is used to get an expression for the electric quadrupole moment. The scalar potential produced by the static charge density of the nucleus is given by

$$\Phi(\vec{r}) = \frac{1}{4\pi\epsilon_0} \int \frac{\rho(\vec{r'})}{|\vec{r} - \vec{r'}|} d^3r' \tag{2.67}$$

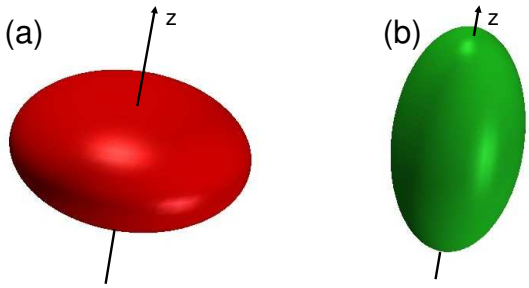

Figure 2.7.: Oblate and prolate deformation of a nucleus. The oblate deformation results in a negative quadrupole moment (a). Prolately deformed nuclei have a positive quadrupole moment (b).

and the first three orders of the expansion [Bet08] are the monopole term

$$\Phi_0(r) = \frac{Q}{r}, \tag{2.68}$$

with the total charge Q, the dipole term, which in the nucleus vanishes due to symmetry reasons and the quadrupole term

$$\Phi_2(r) = \frac{Q_0}{2r^3}, \tag{2.69}$$

with the electric quadrupole moment

$$Q_0 = \int \rho(\vec{r}') \left(3z'^2 - r'^2\right) d^3r' . \tag{2.70}$$

The quadrupole moment is connected to nuclear deformation. A negative Q refers to oblately deformed nuclei (Fig. 2.7 (a)) while prolate deformation causes a positive Q as depicted in Fig. 2.7 (b).

3. Experimental Techniques

In this chapter the basic experimental techniques applied during this PhD work will be presented and discussed, starting from different approaches for the production of exotic nuclei and reaching out to the principle of collinear laser spectroscopy and the different detection methods.

3.1. Production of Radioactive Isotopes

Radioactive nuclei can be produced mainly in three different ways: by charged-particle induced fragmentation, spallation or fission in accelerator facilities, by neutron-induced fission in a nuclear research reactor, or by spontaneous fission. The first method has been employed to study magnesium isotopes in the framework of this thesis and the second one will be the technique used in near future at the TRIGA reactor for which a laser spectroscopy experiment was designed and installed during this work.

3.1.1. Ion Beam Production at ISOLDE

The ISOL technique (Isotope Separator On Line) [Rav79] has been exploited for many years to produce intense beams of radioactive ions. A solid target made of *e.g.* uranium carbide (UC_2) or silicon carbide (SiC) is exposed to the high energy proton beam from an accelerator. The energy of a proton or another light ion hitting a target nucleus is distributed over all nucleons and thus produces a highly-excited nucleus. De-excitation happens by the emission of single protons or neutrons (spallation) or by induced fission of the target nucleus. As a third alternative production channel light nuclei from the mother nucleus are separated by fragmentation. The different reactions are shown in Fig. 3.1. Because of the combination of these processes the proton bombardment allows to produce a large variety of isotopes of different elements, which can be modified by the choice of the target material and the energy of the incident beam.

Several types of ion sources can now be coupled to the target container to allow the reaction products to be ionized. Some elemental selectivity can be obtained by choosing an appropriate way of ionization. The alkali elements and other metals for example can be ionized in a surface ion source, while noble gases require a plasma ion source due to their high ionization potential. A major improvement in element selectivity and thus in the reduction of isobaric background, which cannot be separated by magnetic dipole separators, was obtained by the application of element selective resonant laser ionization in a hot cavity ion source [Mis93]. The unique atomic structure of an element is used as a fingerprint and resonant excitation with lasers in two or three steps with a final ionization step is used to ionize only the element of interest. Contamination from other ionization processes can be suppressed by *e.g.* the choice of the transfer tube material or by choosing a more elaborate source design, for example the laser ion source trap LIST [Sch08]. The schematic of the laser ion source used at ISOLDE (CERN) is shown in Fig. 3.2 [Iso10]. The reaction products effuse out of the hot target in a heated transfer line and arrive in the ionizer tube, where the interaction with the laser and the ionization takes place. The target and the transfer line temperature are important parameters for proper performance of the source with respect to stable ion output and moderate isobaric contaminations. However, the fact that the

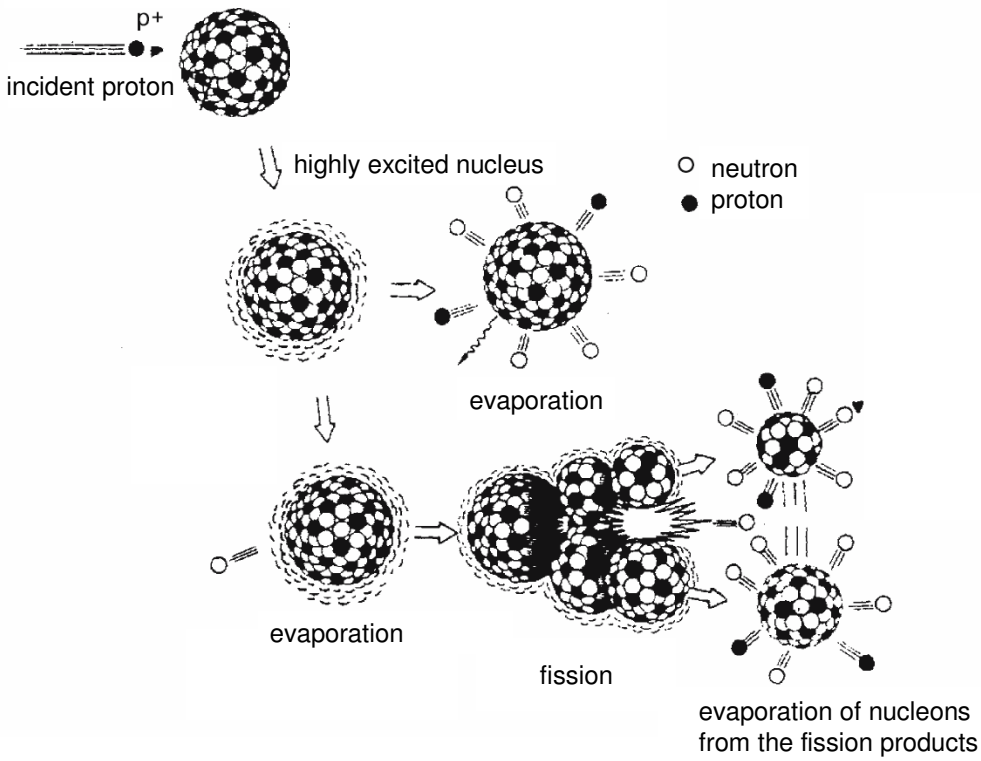

Figure 3.1.: Different reactions induced by high-energy proton bombardment [Bet08]. The fragmentation process is similar to the fission process but with large mass asymmetry and therefore not shown separately.

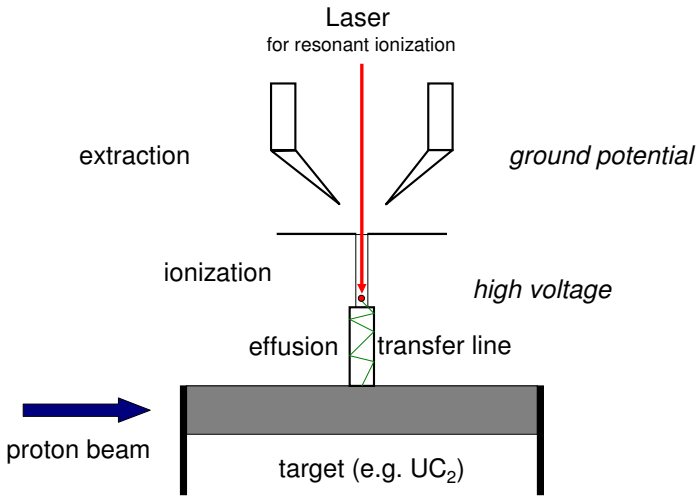

Figure 3.2.: Schematic view of the ISOLDE laser ion source, according to [Iso10].

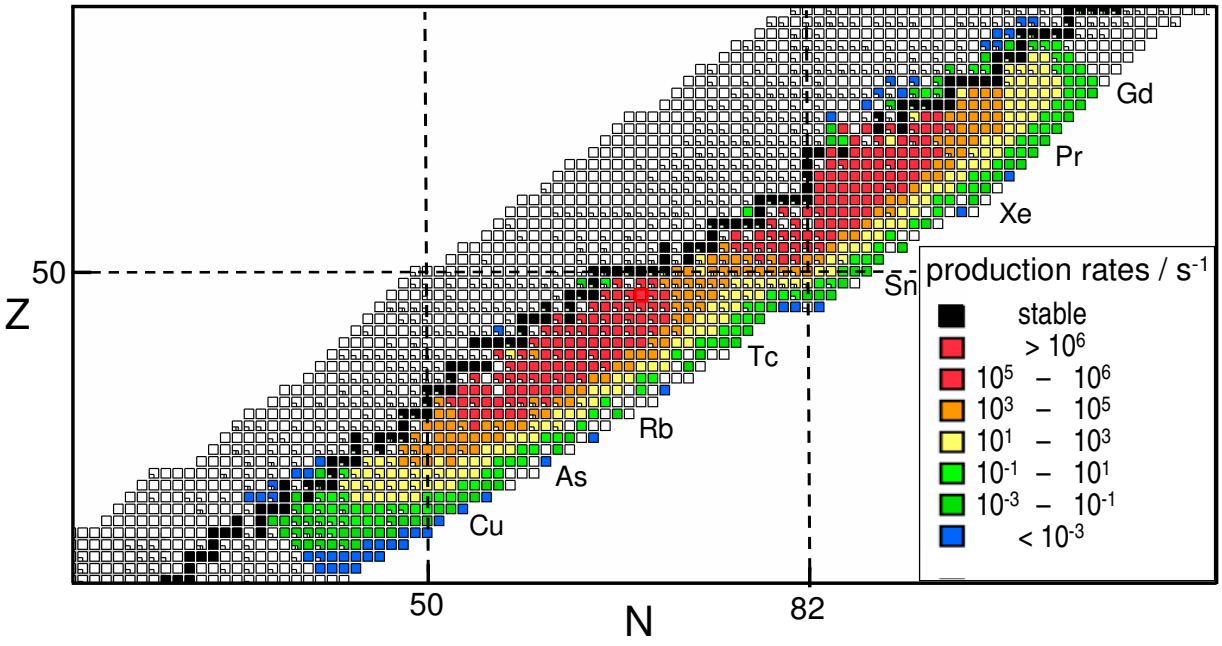

Figure 3.3.: Yield distribution for induced fission of a 300 μg ^{249}Cf target with thermal neutrons with a flux of $1.8\times10^{11}\ s^{-1}$. The yields were taken from [Fir10].

reaction products effuse out of the target and have contact with the target housing and the transfer line surface excludes the extraction of the refractory elements, *i.e.* metals with very high melting points like tungsten, molybdenum or vanadium. This is one of the constraints of the classical ISOL sources.

Operation of the ion source on high voltage up to 60 keV and extraction of the ions towards ground potential results in a rather monoenergetic ion beam which is transported by electrostatic ion-optical devices to a magnetic mass separators. The ISOLDE facility offers two separate ion sources with subsequent mass separator, the general-purpose mass separator (GPS) and the high-resolution mass separator (HRS) with optional isobaric separation. The beams from both sources can be merged into one common distributing beam line, transporting the ions to the various experiments in the ISOLDE hall. The HRS was recently equipped with a gas-filled radiofrequency quadrupole (RFQ) to capture and accumulate the ions and cool them down by gas collisions.

A complementary approach for the production of radioactive ion beams is the production of a charged-particle beam with the IGISOL technique. In such facilities, *e.g.* the IGISOL at Jyväskylä, the primary particle beam hits a thin target and the reaction products recoil out of the target and are stopped in a helium filled gas cell. A multipole ion guide is used to transport and cool the ions before they reach a mass separator [Ä01]. An advantage of this production scheme is the accessibility of the refractory elements.

3.1.2. Ion Beam Production for the TRIGA-SPEC Experiment

In the TRIGA-SPEC experiment the intense neutron flux inside the nuclear research reactor at the University of Mainz is used to produce short-lived isotopes from a solid ^{249}Cf target by

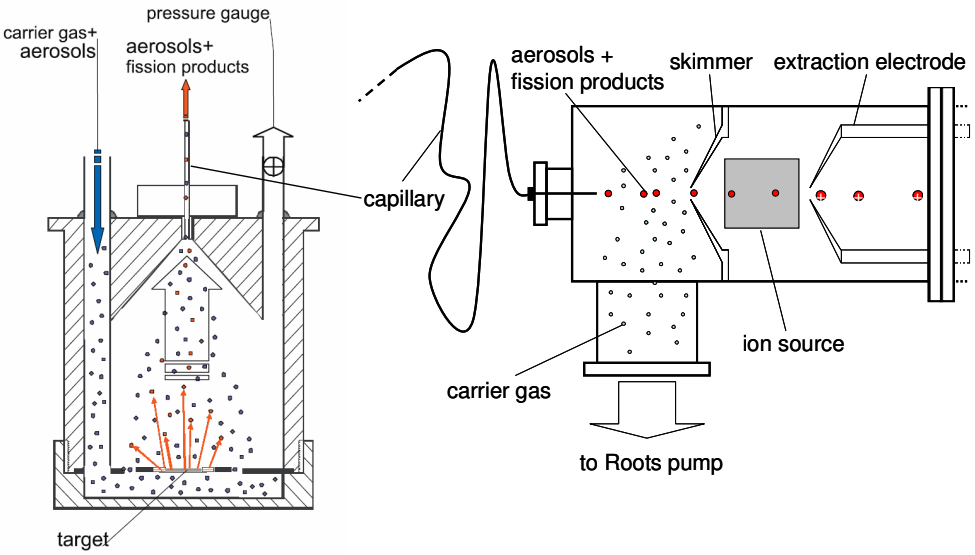

Figure 3.4.: Basic principle of the gas-jet transport and ionization system. The fission products are stopped in the target chamber shown on the left and guided by the gas jet to the ion source setup shown on the right.

neutron-induced fission. The fission fragments show an asymmetric distribution with a lighter mass and a heavier mass branch both situated on the neutron-rich side of the nuclear chart. The yield distribution in the nuclear chart is shown in Fig. 3.3. A target chamber is placed near the reactor core in one of the beam ports and exposed to the flux of the thermal neutrons of $1.8 \times 10^{11}\,\mathrm{cm}^{-2}\mathrm{s}^{-1}$. The fission products are transported from the chamber to an ion source by an aerosol-interspersed He gas jet [Ste80]. This method has already been applied earlier for an online mass separator for γ-ray studies of radioactive alkaline earth and lanthanide isotopes [Bru85]. The recoil nuclei leaving the target material are thermalized inside the target chamber in the helium transport gas at a pressure of typically 2 to 5 bar and attach to aerosol clusters of *e.g.* KCl or carbon. A laminar flow through a polyethylene capillary with ≈ 1 mm inner diameter allows several meters of transport length with low losses. In Fig. 3.4 the basic principle of the production and transport method is shown schematically. Before the reaction products enter the ion source, the essential part of the carrier gas is separated by the expansion in a pressure gradient created by a strong Roots pump and a skimmer in front of the ion source's entrance aperture. In earlier experiments the stable operation of surface and plasma ion sources coupled to a gas jet has been demonstrated [Bru85, Maz76].

3.2. Collinear Laser Spectroscopy with Fast Beams

In the classical approach of collinear laser spectroscopy a laser beam is superimposed with an ion or atom beam with an energy of several keV to several ten keV. The particles are excited in flight and the resulting fluorescence light can be detected with a photomultiplier tube. One big advantage compared to the spectroscopy in a gas cell is the compression of the longitudinal velocity component because of the acceleration of the thermally distributed ion ensemble in the external electric field between the ion source and the extraction optics. This effect can be understood if we consider two ions of the ensemble to be accelerated. Let the first ion's velocity

component in the direction of extraction (z direction) be zero. The second ion should have the full thermal velocity $v_z = \sqrt{2kT/m}$. Both particles undergo acceleration a in the potential difference U between two electrodes with the spacing d. The final velocity of the first ion is according to basic kinematics

$$v_1' = at_1 = \sqrt{2da} = \sqrt{2eU/m}\,, \tag{3.1}$$

where the expression $d = \frac{1}{2}at_1^2$ was used to eliminate the time t_1. The second particle's velocity is given by

$$v_2' = v_z + at_2 \tag{3.2}$$

and the time can be eliminated by the expression

$$d = \frac{1}{2}at_2^2 + v_z t_2\,, \tag{3.3}$$

giving $t = -v_z/a + \sqrt{v_z^2/a^2 + 2d/a}$. Inserting this in 3.2 gives the velocity of the ion with initial component v_z

$$v_2' = \sqrt{2eU/m}\sqrt{1 + \frac{v_z^2}{2eU/m}} \approx \sqrt{2eU/m} + \frac{v_z^2}{2\sqrt{2eU/m}}\,, \tag{3.4}$$

which can now be compared to the velocity of the first ion. While the initial velocity difference was the thermal velocity $v_{\text{therm}} = \sqrt{2kT/m}$, the difference after acceleration becomes

$$\delta v_z = \sqrt{2kT/m} \times 1/2\sqrt{\frac{kT}{eU}} \tag{3.5}$$

and is hence reduced by a factor proportional to $\sqrt{1/U}$ which is referred to as a *velocity bunching effect*. The line width of an optical transition probed by a laser in the z direction is therefore reduced by the same factor since the residual Doppler width is proportional to the velocity distribution (see Ch. 2.1.4). For a typical case with a surface ion source as used in our test experiment with a temperature of 1500 K and an acceleration voltage of 10 keV the compression factor for the line width becomes ≈280. This means that the linewidth obtained by spectroscopy in a gas of typically several GHz reduces to several tens of MHz which is of the order of the natural linewidth of the allowed optical dipole transitions and therefore allows to perform high-resolution measurements giving access to hyperfine structures even of excited atomic levels.

The Doppler shift on the laser frequency in the rest frame of the moving particles allows to perform *Doppler tuning*: The ion velocity is changed by applying an additional voltage gradient before the optical detection setup, changing the frequency in the rest frame of the atom. The laser frequency can be kept fixed, allowing even the use of fixed-frequency lasers in special cases. Generally, it is much easier to stabilize a laser to a fixed, well-known frequency than to tune it with high reproducibility of every frequency along the scan range. The Doppler-shifted frequency ν' for an ion with charge e and rest mass m accelerated with the total voltage difference U is given by (see App. A)

$$\nu' = \nu_{\text{laser}} \frac{(eU + mc^2)}{mc^2} \left(1 \pm \sqrt{1 - \left(\frac{mc^2}{eU + mc^2}\right)^2}\right) \tag{3.6}$$

where the $-$ has to be used for collinear and the $+$ has to be used for anti-collinear laser-ion geometry. The high accuracy of the laser spectroscopic technique requires a relativistic

calculation even at these relatively low energies. With the commonly used high-voltage amplifiers to apply the tuning voltage, a typical maximum scanning range of 1000 V can be obtained, which in the case of magnesium at $\nu_{\text{laser}} = 280\,\text{nm}$ for example, with total voltages of 50 keV and a mass of 30 u corresponds to a frequency range of 20 GHz. This is sufficient to scan hyperfine structures also with greater interval factors. For isotope shift measurements, however, an additional static offset voltage is commonly used to jump from one isotope to the other.

3.2.1. Specialized Applications

The optical detection of the fluorescence photons with a scanning voltage applied to the optical detection setup can be considered as the classical approach of collinear laser spectroscopy. However, restrictions concerning the sensitivity of the detection setup, limiting the lowest-possible particle yield of the species of interest or limited access with commercially available laser systems have led to the development of specialized techniques to enhance the capabilities of the experimental method.

Charge Exchange and Spectroscopy with Fast Atoms

The field of usage of collinear laser spectroscopy can be expanded to neutral atoms if the second acceleration or deceleration stage in the setup is equipped with a charge exchange cell (CEC). Further details about the principle of the CEC and the neutralization will be given in Ch.5.5 and Ch. 6.1.2.

Photon-Ion Coincidence Detection

Laser straylight produces a considerable amount of background on the photomultiplier in the classical optical detection scheme, limiting the sensitivity at very low yields of radioactive isotopes. This background can be reduced if the photomultiplier is gated to the signal of a destructive particle detector at the end of the beamline. The idea is that only photon events are counted that produce a particle signal after the time of flight to the detector [Eas86]. In order to trigger the gate on the particle signal, an appropriate way to delay the photon signal has to be chosen to avoid dead-time losses. The width of the gate has to be chosen according to the length of the optical setup. An increase in signal to noise of a factor of 1600 has been demonstrated in past experiments [Eas86]. At TRIGA-LASER a particle detector for the coincidence technique was recently built and tested during a diploma thesis [Sie10].

An alternative to the destructive detection of single ions or atoms is to gate on the release pulse of the ion bunch from an RFQ cooler and buncher. In this special case all fluorescence events occur during a short period corresponding to the length of the ion bunch.

β-Asymmetry Detection by Optical Pumping and β-NMR

The sensitivity of the standard optical fluorescence detection even with the coincidence technique is limited by the laser-induced background to about 10^4 ions s^{-1} to obtain a reasonable signal-to-noise ratio within a short time. For more exotic short-lived isotopes with lower yields, a different method can be applied. Circularly polarized σ laser light is used to polarize the ions by optical pumping (see Ch. 2.1.5). The nuclear polarization achieved by optical pumping and decoupling of the nuclear and the atomic spin in a strong magnetic field leads to a spatial anisotropy in the emission of the positrons/electrons from the β decay. This anisotropy can therefore be detected and used as a probe for the resonant pumping process. The intensity of emitted electrons or

positrons is given by the projection of the β particle velocity $\vec{v}$ on the spin $\vec{I}$ of the polarized nuclei [Kon59]

$$I(\Theta_{eI}) = 1 + A\frac{\vec{I}}{|\vec{I}|} \cdot \vec{v}/c = 1 + Av/c\cos\Theta_{eI}\,, \tag{3.7}$$

with a parameter $A = a \times P_I$ that can directly be linked to the degree of nuclear polarization P_I and an angle dependence. In the implanted crystal the polarization decays with time due to the interaction with the host medium (spin-lattice relaxation). The easiest way to experimentally detect such an asymmetry is a setup with two opposing particle detectors, *e.g.* scintillators, arranged in two planes perpendicular to the nuclear spin direction. The difference of the count rates of both detectors yields the asymmetry.

Instead of just detecting the asymmetry as a function of the applied Doppler tuning voltage, a resonant destruction of the polarization and hence, the asymmetry, can be achieved by applying a radio-frequency field to the nuclei implanted in the crystal. In the process of this nuclear magnetic resonance (NMR) the polarization is reduced resonantly by induced transitions between individual magnetic substates m_I. The energy shift of a level with the quantum number m_I in a strong magnetic field is given by

$$\Delta E(m_I) = -m_I g_I \mu_N B = -m_I \hbar\omega_L \tag{3.8}$$

(see Eq.2.27 in the strong field approximation), with the Larmor frequency $\omega_L = g_I\mu_N B/\hbar$. A disturbing oscillating magnetic field, tuned to the Larmor frequency and applied perpendicularly to the strong magnetic field axis, mixes the substates by transitions with the selection rule $\Delta m_I = \pm 1$ and leads to an equally distributed population of the states and a destruction of the β-decay asymmetry. From the Larmor frequency the nuclear g_I factor can be deduced if the magnetic field B is known accurately or is eliminated from Eq. 3.8 with a reference measurement. A schematic view of a collinear laser spectroscopy setup summarizing the different possible detection methods is shown in Fig. 3.5.

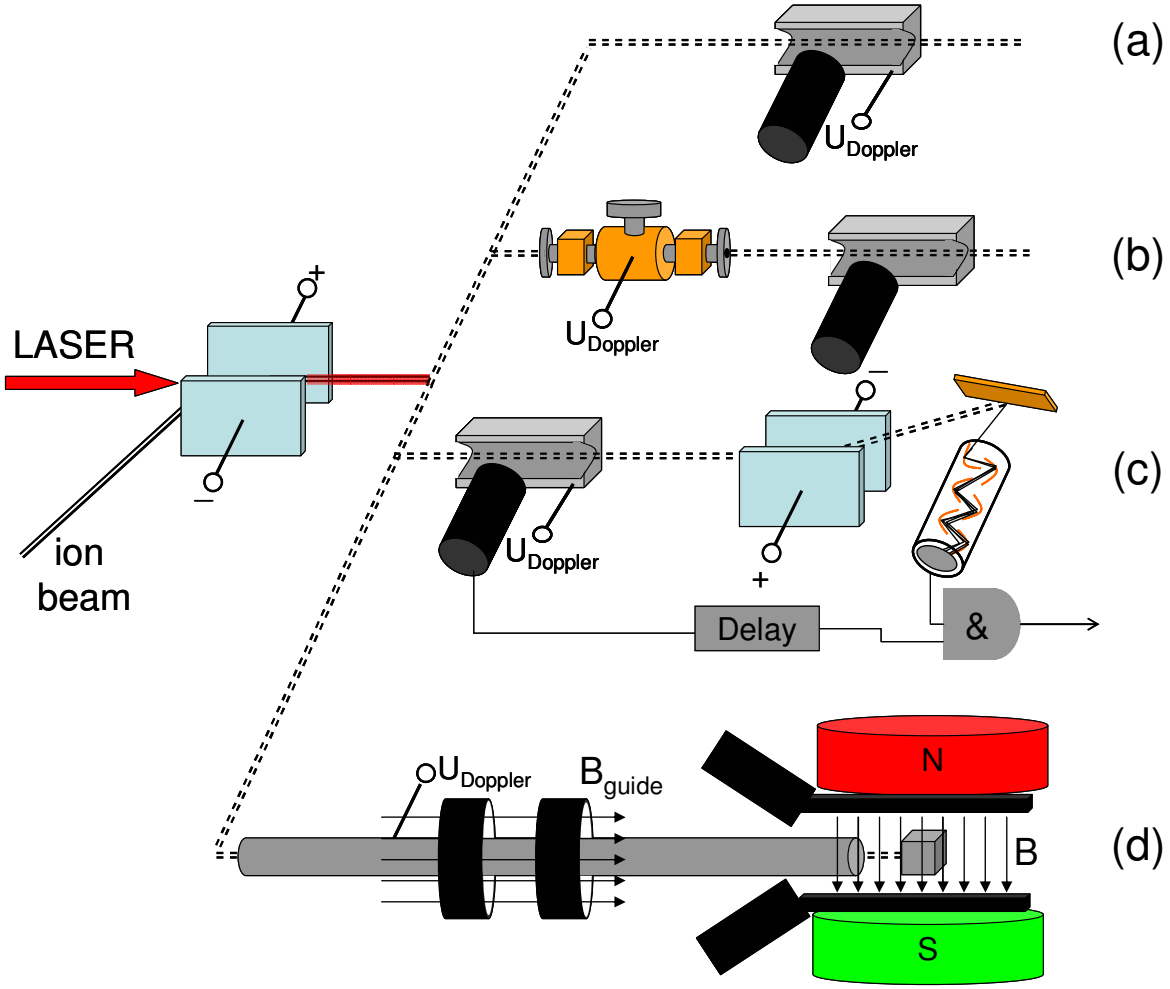

Figure 3.5.: Principle of collinear laser spectroscopy and the different possible extensions. (a) shows the classical optical detection with ions. The tuning voltage is applied to the mirror in the optical detector. (b) combines the optical detection with a charge exchange to perform spectroscopy with atoms. To increase the signal to noise ratio the optical detection can be combined with a subsequent particle counting, shown in (c). In the case of short-lived radioactive nuclei the β-asymmetry detection can be applied after optical pumping with σ polarized light in a guiding field as it is shown schematically in (d).

Part I.

Commissioning of the Collinear Laser Spectroscopy Setup TRIGA-LASER at the TRIGA Research Reactor Mainz

4. Layout of the TRIGA-SPEC experiment

In the TRIGA-SPEC experiment exotic nuclei produced by neutron-induced fission near the core of the TRIGA research reactor at the Institute of Nuclear Chemistry Mainz will be studied by collinear laser spectroscopy or Penning trap mass spectrometry [Ket08]. A schematic overview of the whole setup is given in Fig. 4.1 showing the different stages from production of the short-lived isotopes, ion beam formation and preparation up to the final experiments. Fig. 4.2 shows a photography of the whole experimental setup still in the construction phase.

The reaction products from the target (see Ch. 3.1.2) are transported on aerosols in a gas jet into an electron cyclotron resonance (ECR) ion source. The ECR is equipped with permanent magnets to create the magnetic field for the confinement of the electrons in the plasma. The electron motion is driven by a 2.54 GHz microwave field coupled into the plasma chamber of the source from above by hollow conductors and an antenna. This allows to inject the aerosols and the fission products from the back side of the source. The whole source is operated at up to 30 keV high voltage and the ions are accelerated towards an extraction electrode at ground potential.

A 90° magnetic dipole sector magnet is used to mass separate the ions of interest for the particular experiment from the large variety of ion species that are produced in the ECR source. The magnet from the Chinese company *Lanzhou Lanke Complete Set of Machinery* has a 0.5 m bending radius, a pole gap of 50 mm, and produces a maximum field of 1.2 T. The maximum current rating is 250 A. The iron yokes at the entrance and the exit of the magnet are designed according to a Rogowski profile to exhibit double-focussing properties. This means that a parallel beam that enters the magnet is focussed in both planes with the same focal length. To supply the current for the magnet, a high-power current source System 8500 MPS 853 from Danfysik is used.

Due to the relatively low yields of the fission process with 10^7 particles s^{-1} at maximum before ionization, a normal continuous beam operation of the experiment would result in very long integration time needed to see a signal. For the laser experiment, this might not be possible at all, even if care is taken in reducing the background. In the case of the Penning trap the problem is the ion-beam energy of several keV required for an efficient mass separation in the dipole magnet, because the Penning trap can only accept and trap ions with energies of a few hundred eV. A pulsed drift tube is therefore needed to slow down the ions by switched electric fields, which only works efficiently with a pulsed beam. Otherwise, only a small fraction of the continuous beam would be cut and decelerated, resulting in a particle rate of less than one ion per second. Therefore, a radio frequency quadrupole (RFQ) cooler and buncher will be installed right after the separation magnet. This will allow timing the pulsed drift tube with the ion bunch in the case of TRIGA-TRAP and gating the photomultiplier on the bunch, reducing the laser induced background by a large amount. The COLETTE RFQ [Lun09] formerly used at ISOLDE in the MISTRAL experiment has been allocated for this purpose. It is a linear Paul trap filled with a buffer gas and operated at high voltage, in which the ions are trapped by static and radio frequency electric fields and cooled by collisions with the buffer gas atoms. The technical design of the cooler is shown in Fig. 4.3. The release of the cooled ions results in a bunched beam with significantly lower transverse phase space volume and narrow longitudinal

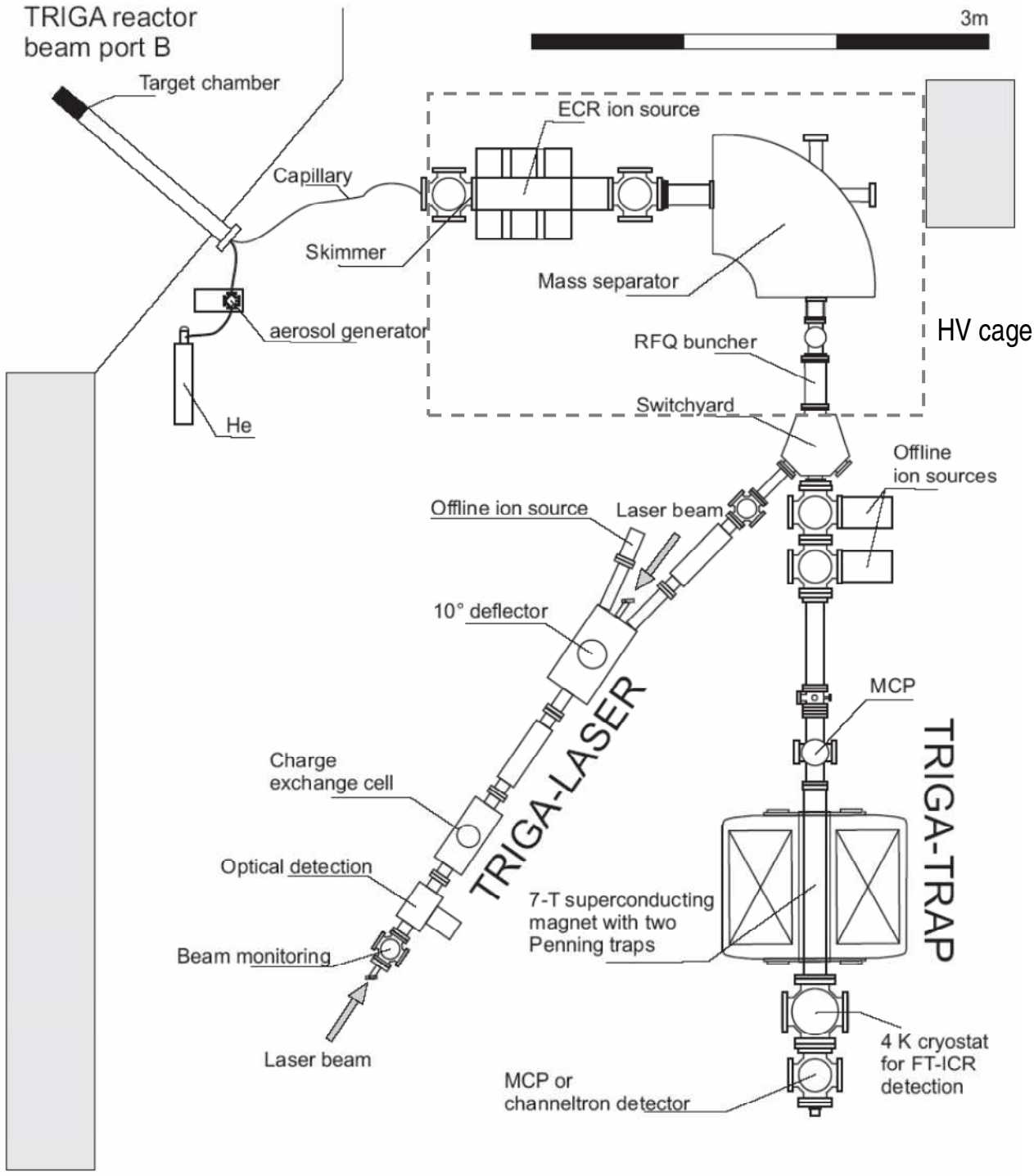

Figure 4.1.: Layout of the TRIGA-SPEC experiment. Details see text.

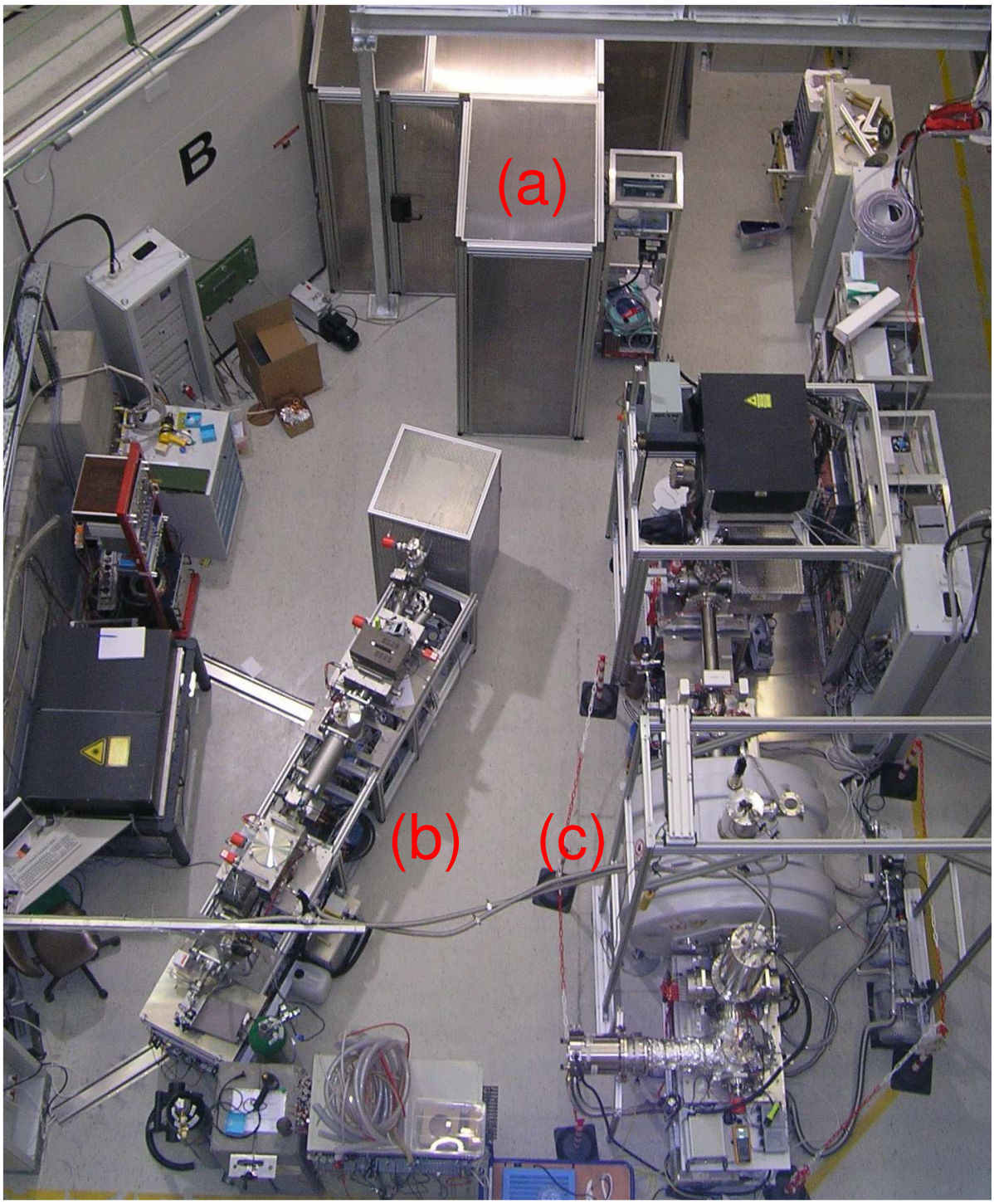

Figure 4.2.: Photography of the TRIGA-SPEC experimental setup (May 2009). (a) is the high voltage cage for the ion source. (b) is the collinear laser spectroscopy setup and (c) is the Penning trap setup with the superconducting magnet.

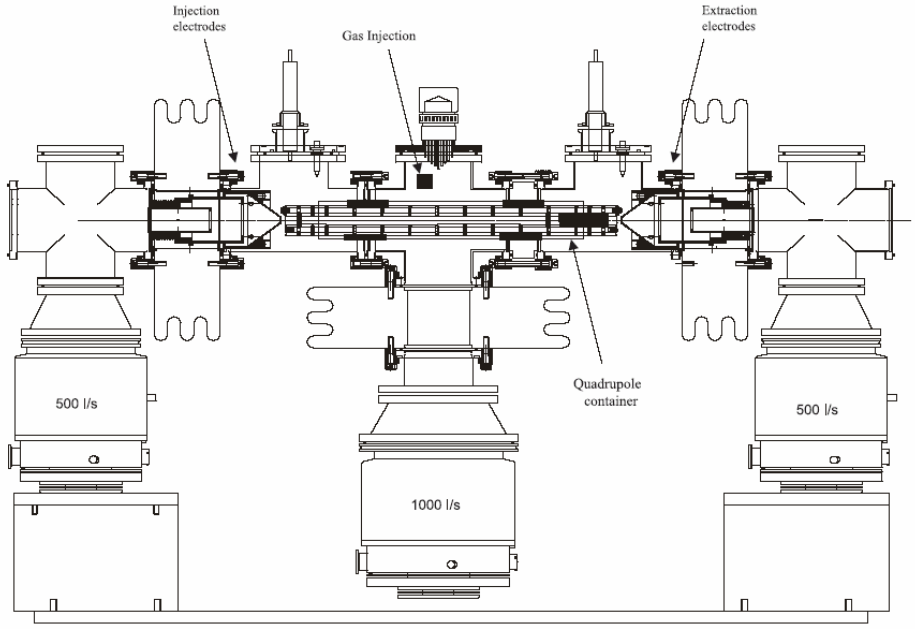

Figure 4.3.: Technical drawing of the COLETTE RFQ [Lun09]. The ion beam is injected from the left. The central part includes the gas-filled radiofrequency quadrupole (RFQ) that can be floated to the potential of the ion source to stop the ions inside the gas cell. After accumulation and cooling the ions are ejected on the right.

energy spread. The drift tube for the Penning trap experiment as well as the optical detector in the laser spectroscopy setup can then be triggered on the ejection pulse of the RFQ.

The Penning trap setup TRIGA-TRAP is a two-stage Penning trap which is mounted in a 7 T superconducting magnet. The first trap is a cylindrical purification trap to remove isobaric contamination and to cool the ions in a He buffer gas. The second trap is a hyperbolic Penning trap for the mass measurements by ion-cyclotron resonance either by recording the time of flight from the trap to a particle detector as a function of the excitation frequency (TOF-ICR) or by performing a Fourier transformation of the induced ion mirror current in the trap electrodes (FT-ICR). Both methods use the resonant excitation of the ion cyclotron motion in the trap at the cyclotron frequency $\omega_C = eB/m$. If the magnetic field B is known accurately or can be eliminated by a reference measurement, the mass m can be calculated from the frequency ω_C (see [Ket08] for further information). The application of carbon clusters as the aerosol used for the gas-jet transport offers a unique possibility to calibrate the mass measurement to the standard mass, defined by the isotope ^{12}C. The ion source is expected to produce a mass comb of carbon clusters with a wide variety of masses, allowing to find a suitable reference mass $n \times 12\,\mathrm{u}$, with integer n, for every isotope mass studied at a time. For off-line measurements a carbon cluster source operated with a pulsed frequency-doubled Nd:YAG laser is included that allows for cluster generation using laser ablation.

5. The Collinear Laser Spectroscopy Branch TRIGA-LASER

A high spectral resolution and a good transport and detection efficiency are the main design considerations for a collinear laser experiment. The ions or atoms of interest usually have low production rates and additional losses during the transport have to be avoided. In addition, the spectral line position needs to be extracted with high precision. Careful simulation of the beam steering and focussing elements before the charge exchange cell (CEC) ensure a configuration with low losses and an approximately spherical beam profile. Field gradient studies on the apertures of the detection chamber and CEC respectively, allow a design of the drift sections to minimize field penetration and hence, a blow-up of the longitudinal velocity spread of the ion beam after post acceleration or deceleration. For the simulation the SIMION code [Dah90] was used, which uses a Runge-Kutta algorithm to numerically solve the equation of motion of a single particle in a given field geometry defined by the solution of the Laplace equation. The geometries for the simulations can be imported from a 3D CAD program, in which the whole beam line with all components have been designed. An instruction for this import procedure can be found in App. B.

The complete TRIGA-LASER setup including the beam transport part after the separator magnet is shown in Fig. 5.1. All parts except the quadrupoles and the charge-exchange cell, which were already existing, are custom designs that have been developed and built during this PhD work.

5.1. The Vacuum System

The choice of a vacuum standard is an essential part of the design of a vacuum beamline. The final pressure, maximum bakeout temperatures, and maintenance time are differing a lot comparing copper sealed conflat flanges with ordinary rubber sealed flanges. For its relatively low cost, the sufficiently low minimum pressure of 1×10^{-7} mbar and the very short time to open and close the system as all flanges are fixed with clamps only, the ISO-K standard with viton seals was chosen for our setup. The vacuum pressure is maintained by 3 EBARA ET-300WS turbo pumps with purely magnetic bearings in the main sections and Edwards XDS 10 scroll pumps for the pre-vacuum side. Since the ion-beam switchyard and the beamline connecting it with the 10° deflector is not installed yet, there are three sections separated by air-actuated vacuum valves. The valves can be controlled manually or by pre set switching pressures of the vacuum gauges in order to avoid accidental ventilation of the whole setup in case of a leak. The first section is containing the off-line ion source used for the commissioning of the setup. The small ISO-K100 vacuum cross is pumped by a Pfeiffer TPU170 and an Edwards rotating vane pump. In the second section beam shaping and steering takes place in order to prepare the ion beam to enter the small apertures of the charge-exchange cell and the fluorescence detector in the third vacuum section and match the particle beam to the transversal laser beam profile.

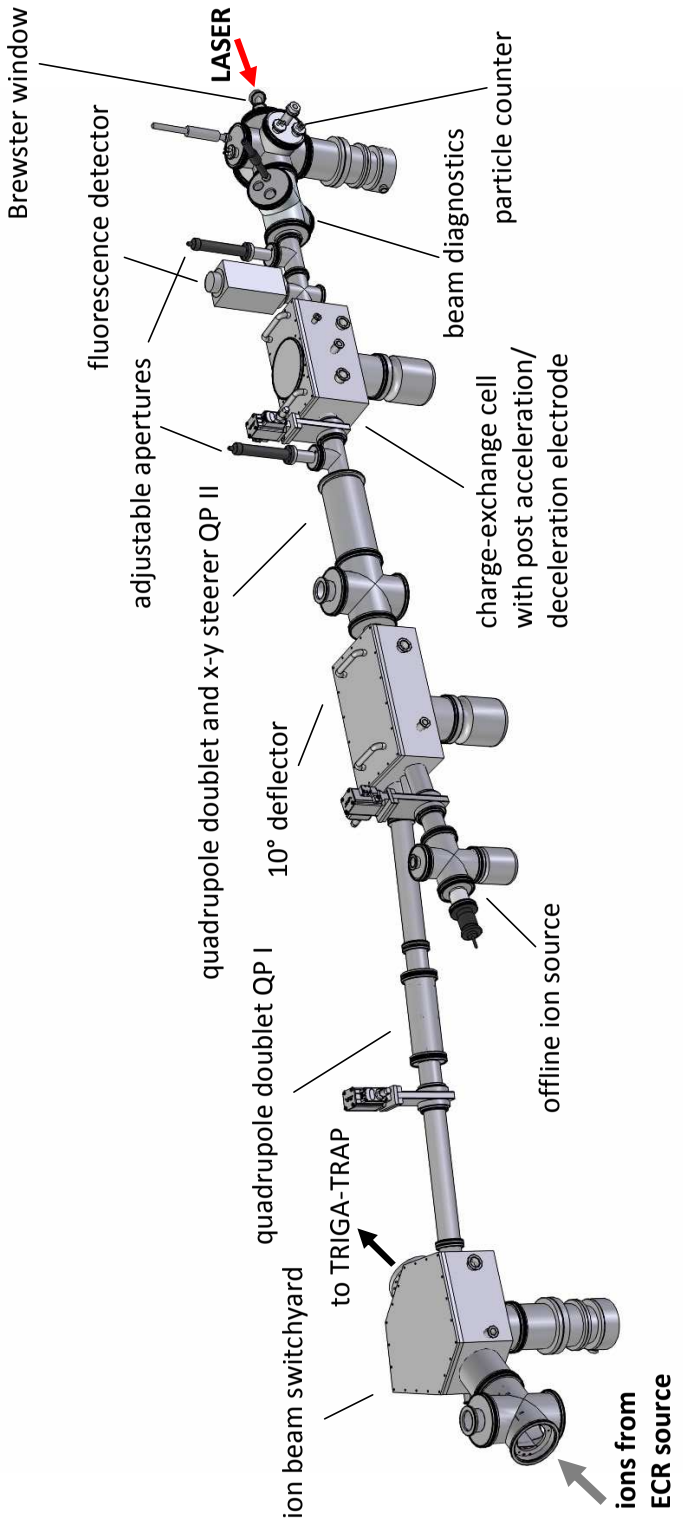

Figure 5.1.: 3D drawing of the TRIGA-LASER setup including the beam transport section and the offline source.

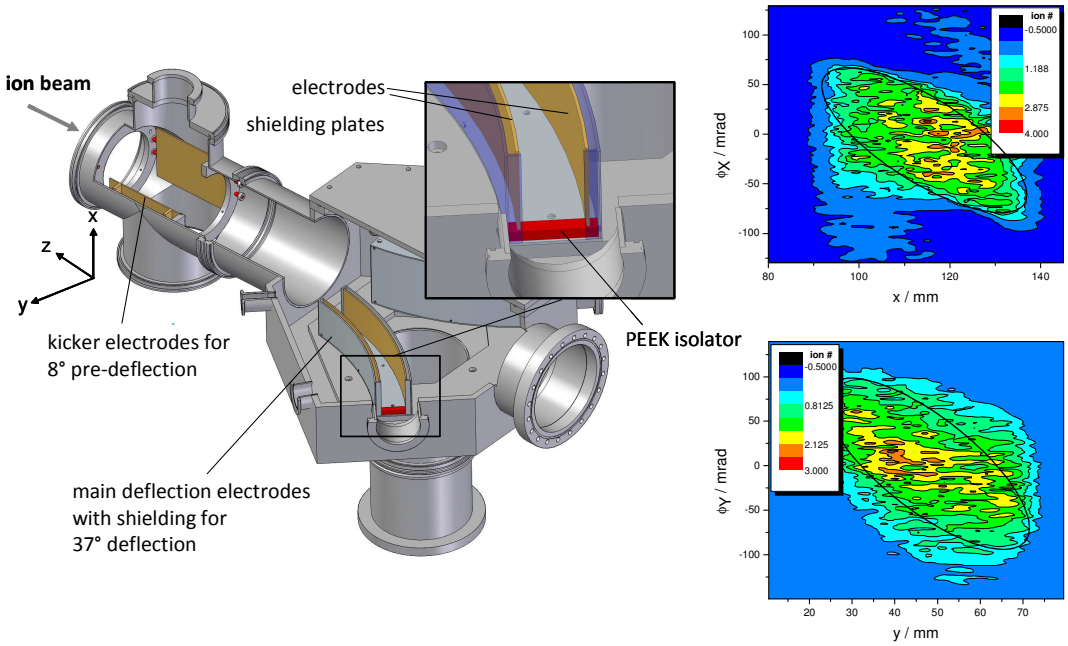

Figure 5.2.: CAD model of the electrostatic switchyard with beam acceptance phase space density plots. The switchyard includes a two-stage deflection unit with a 8° kicker and two main deflectors for guiding the beam at angles of ±45°. Beam transport through the central port is also possible and will be used for TRIGA-TRAP.

5.2. The 45° Electrostatic Switchyard

The 45° switchyard is a two stage deflection unit allowing to either send the ion beam to the Penning trap setup [Ket08] straight ahead or to the laser spectroscopy setup to the side. A 8° pre-deflector (kicker) with plane electrodes in an ISO-K 160 cross before the main vacuum chamber is used to predefine the path of the ion beam. The 37° main bending electrodes with curved shape are shielded and can remain on their deflection potential, no matter where the ion beam is sent to by the kicker. A beam that is not deflected by the kicker will pass the main chamber without deflection. A pre-deflected beam will enter the bending electrodes and undergo further deflection in the field gradient of the main deflection electrodes. The main advantage of this kicker-bender combination compared to other designs with mechanically moving electrodes (see e.g. [Baa97]) is the possibility for fast switching between up to three experiments by just changing the voltage on the kicker, which can be achieved in less than a microsecond. A quasi-parallel operation is therefore possible. The design of the kicker with a large gap of the electrodes of 100 mm and the commercially available vacuum cross with two additional flanges allow a combination with beam diagnostic devices like a Faraday cup or an MCP. A CAD model of the device is shown in Fig. 5.2. The acceptance from the phase space density plots can be estimated to $\approx 1000\,\pi$ mm mrad for both, x and y coordinates.

The acceptance was deduced from the density plots by the area of the ellipse drawn in and which was chosen to allow 100% transmission for all ions inside the ellipse area. To obtain such an acceptance plot 50 000 ions were defined to start in front of the device with randomized starting positions in x-y plane on a circular disc and randomized starting angles. The initial coordinates of the particles that left the device and passed a plane behind it were recorded and

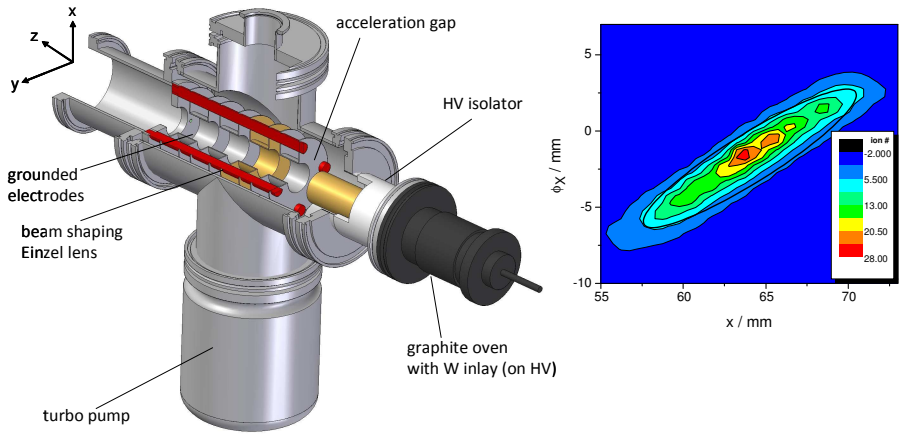

Figure 5.3.: Schematic view of the offline ion source and density plots of the phase space of the emitted ions. The offline ions from the oven on high voltage are accelerated by the first extraction electrode. A subsequent Einzel lens is used to form an ion beam with small divergence angle. The emittance extracted from the phase space plots is estimated to be $\approx 10\,\pi$ mm mrad at 10 keV.

evaluated. The deflection voltages extracted from the simulation are ± 93.3 V per keV ion energy for the kicker and the main electrodes, giving ± 2800 V for a 30 keV ion beam.

5.3. The Offline Ion Source

For first test experiments and commissioning of the ion optical devices, a simple ion source was constructed which is based on a resistively heated graphite oven [Gep00]. This oven was originally designed to produce an atomic beam, but for alkali and earth-alkali elements surface ionization [Dre68] allows the production of ion beams which can be extracted with an appropriate electrode geometry. The usage of a tungsten inlay facilitates the ionization and increases the ion yield. Fig. 5.3 shows the schematic drawing of the ion source and the extraction optics. The oven itself is put on a high potential, defining the ion energy after extraction and acceleration by the first electrode after the oven. The second electrode is again put on high voltage to form an Einzel lens together with the extraction electrode and the following electrode. The fourth electrode at the end exit flange is grounded and has no effect in this configuration. With this arrangement a nearly collimated beam with an emittance of $\approx 10\,\pi$ mm mrad at 10 keV can be formed, which is extracted from the phase space plots from Fig. 5.3 and is indicated by the ellipse. For the simulation a randomly distributed ensemble of ions with the thermal kinetic energy of ≈ 0.2 eV and randomly distributed emission angles was starting inside the model of the graphite tube being on a constant potential. Only the ions that effused out of the tube were accelerated. The voltage gradient existing on the real source due to the heating voltage applied on the tube was neglected.

In order to apply the acceleration voltage for the source, a compact high voltage cage was constructed which allows to put the whole source and the current supply for the oven on up to 10 kV. A Tauscher HTT-25F isolation transformer is used to float the ground potential of the 100 A supply. The water cooling tubes for the oven are wound at a length of 10 m inside the cage before being connected to the cooling water supply in order to restrict the current

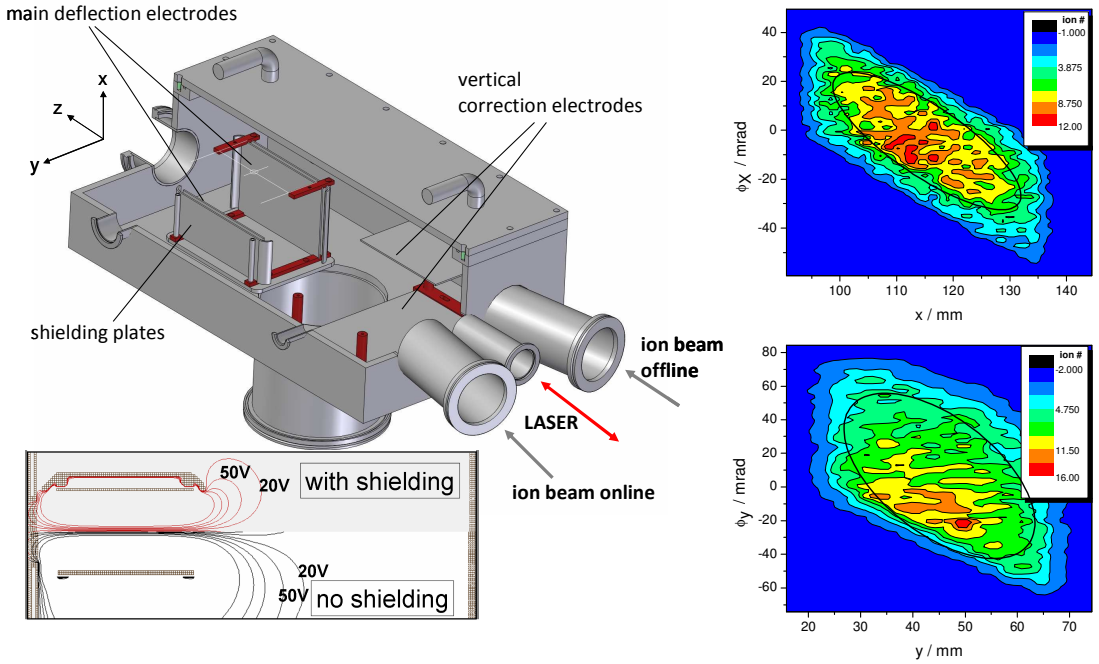

Figure 5.4.: CAD model of the 10° deflector with simulated acceptance density plots. The ellipses indicate the region where full transmittance is given. The small inset shows the SIMION field plot for a configuration with or without the shielding electrodes. For more details refer to the text.

being conducted by the water to $\leq$2 mA. The source high voltage is provided by a Heinzinger PNChp 60000 high precision voltage supply with the same specifications concerning stability as the one used to apply the voltage to the CEC.

5.4. Design of the 10° Deflection Chamber

The 10° deflection chamber electrostatically deflects the ion beam from two possible entrance directions in order to merge the ion beam with the laser beam axis. The main components are two pairs of plane deflection plates and the entrance/exit flanges for the laser and ion beam. The main electrode pair used for the horizontal deflection (y direction) is equipped with two shielding plates covering the main electrodes and reducing the electric field surrounding the deflector that could lead to ion beam distortion as indicated in the small inset in Fig. 5.4. This very simple design was chosen in order to allow large apertures for the laser light reducing scattered light. From an ion-optical point of view, as in the case of the switchyard, such a design has the disadvantage of focussing the ion beam in the deflection plane while not influencing the perpendicular plane. This leads to an elliptically deformed ion beam if an initially round profile is assumed. In Fig. 5.4 the 3D model of the chamber is shown together with density plots of the acceptance for both planes. From these plots an acceptance of $\approx 300\,\pi$ mm mrad can be estimated which should by far be sufficient to transmit 100% of the ion beam from the ECR source. An optimal transmission with 10° deflection is given at an electrode voltage of ± 106 V per keV of ion energy or ± 3180 V for a 30 keV beam. The previously mentioned beam asymmetry can be corrected by the subsequent quadrupole doublet which will be shown later in the overall

transmission simulations (see Section 5.8).

For beam monitoring purposes a Faraday cup is installed inside the vacuum chamber next to the exit flange on the source axis. With the deflection voltage turned off, the primary ion beam current can be measured.

5.5. The Charge-Exchange Cell

The charge-exchange cell (CEC) was adopted from an earlier experiment [Bac74, Ant78] and only the surrounding chamber and the high-voltage platform were constructed in this PhD work. The cell consists of a tubular housing with beam entrance and exit apertures containing the neutralizing agent (e.g. metallic Na, K, Cs, Rb) in a small reservoir. The center of the cell is electrically heated to melt and evaporate the metal. Both ends of the cell are cooled with copper blocks that are chilled by circulating synthetic low conductance thermalizing liquid by an external chiller. A stainless steel wire wick ensures the distribution of the liquid metal and the reflow to the reservoir. The whole cell is mounted on an isolated platform and can be put on a well defined potential up to ±10 kV to post-accelerate or -decelerate the ion beam for Doppler tuning. An electrode in front of the cell defines the acceleration gap together with the wall of the vacuum chamber and minimizes the field gradient close to the aperture of the cell. After neutralization the atoms keep the energy defined by the CEC potential. Residual ions can be deflected and separated from the atom beam with a small kicker configuration right after the cell. Fig. 5.5 shows the 3D CAD model of the CEC and the vacuum chamber. The acceptance from the simulation is estimated to be $\approx 20\,\pi$mm mrad. This is much smaller than the values for the other devices and is caused by the small entrance and exit apertures of the CEC of 7 mm together with the 200 mm length. Consequently, the subsequent optical detection region with slightly larger apertures does only have a minor effect on the limiting phase space of the transmitted beam after passing the CEC. As will be shown later in Section 5.3 the offline ion source produces an ion beam with an emittance small enough to be transmitted through the CEC and the optical detection setup with low losses, provided, careful beam shaping is done beforehand.

The voltages to perform the Doppler tuning are supplied by a Kepco BOP 500 voltage amplifier with an amplification factor of $f_{\mathrm{Kepco}} \approx 50$ fed by the output of a bipolar 16 Bit DAC allowing voltages from -500 V to +500 V and a high precision high voltage supply Heinzinger PNChp10000 with a maximum voltage of 10 kV with selectable polarity and a precision of 1×10^{-5} in 8 h operation time. At a later stage of the experiment the 10 kV supply will be used to make voltage jumps to go from one isotope to another for isotope shift measurements. The Kepco amplifier will be used for fast scanning of the voltage around the value given by the Heinzinger supply. Hence, the amplifier voltage is added to the main acceleration/deceleration voltage by floating the high voltage supply. A schematic view of this setup can be seen in Fig. 5.6. A Julie Research Labs high voltage divider KV-10R with an accuracy of 10^{-4} and an Agilent 34401A precision multimeter are used to measure the applied voltage. The total acceleration voltage for the Doppler shift in this experiment is therefore

$$U_{\mathrm{total}} = U_{\mathrm{source}} - \left(U_{\mathrm{Heinzinger}} + f_{\mathrm{Kepco}} \times U_{\mathrm{DAC}} \right) . \tag{5.1}$$

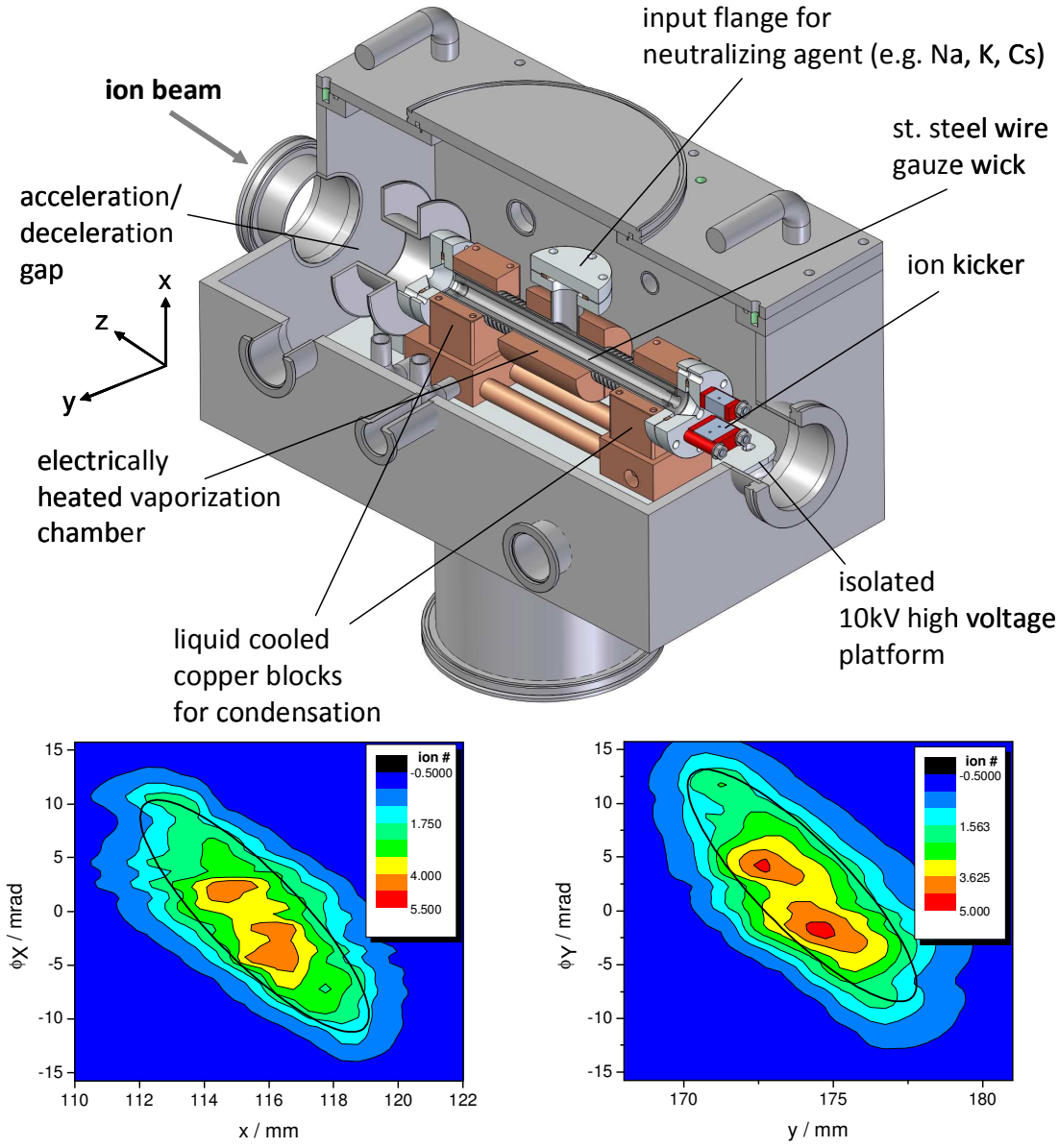

Figure 5.5.: 3D model of the charge-exchange cell and the vacuum chamber built for this experiment. The cell can be put on a well defined high voltage inside the vacuum chamber for Doppler tuning. The metal for neutralization can be inserted in the reservoir through a small flange and is evaporated in an oven. Liquid cooling at the sides of the cell condensate the metal vapor and prevents flooding of the vacuum chamber. The acceptance density plot allows the extraction of an acceptance of $\approx 20\,\pi$mm mrad.

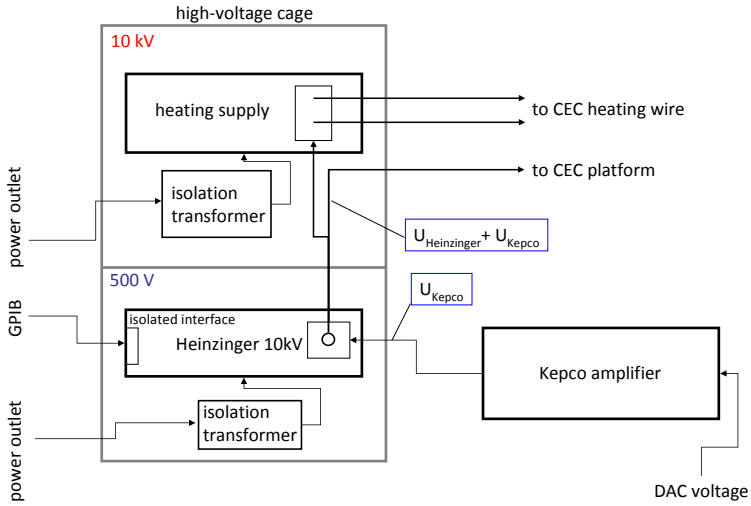

Figure 5.6.: Schematic view of the circuiting of the CEC post-acceleration/deceleration voltage supplies. The cage is separated in a low-voltage part for the Heinzinger supply and a high-voltage part for the CEC heating supply.

5.6. The Optical Detection Unit

The optical detection unit for this first version of the collinear laser spectroscopy setup is based on an ellipsoidal copper mirror with highest reflectivity for photons in the near-infrared region [Ple10], which collects the fluorescence photons in the one focus and reflects them to the other focus, which is located right on front of a light guide behind a vacuum viewport. A Hamamatsu R1017 extended infrared photomultiplier with 3% quantum efficiency for $\approx$ 800 nm light is used to detect the photons transmitted by the light guide. The details of the setup are shown in Fig. 5.7. The mirror can be put on high voltage for Doppler tuning on ions. Only small modifications have to be made for spectroscopy of ions instead of atoms. A wire grid under the vacuum viewport is inserted to define the potential of the mirror on this large aperture and to minimize the field gradient. Before the photomultiplier a set of wire strips is used to prevent stray fields in the photomultiplier. Stray light from the laser is reduced by apertures of increasing diameter in the tubes before and after the collecting mirror. The apertures have conical bores in order to exhibit only a small length for possible diffraction. The acceleration gap was designed with SIMION in order to ensure the smallest possible field gradient inside the mirror to prevent broadening of the fluorescence lines because of the detection of photons from ions on slightly different potentials. In the first 5 mm of the detector the field differs only by 1×10^{-6} from the final offset potential. This was obtained by placing an aperture of 11 mm after the acceleration gap and in 20 mm distance from the mirror entrance.

The signals from the photomultiplier are amplified and discriminated against electronic noise before they are sent as TTL pulses to the counter card of the data acquisition computer.

5.7. Beam Diagnostic Devices

A beam diagnostic chamber consisting of an air-actuated Faraday cup and a Danfysik dual vane probe System 5100 allows to measure the current of the ion or atom beam and, for sufficiently high currents of several hundred pA, also the beam shape. The vane probe is an oscillating fork

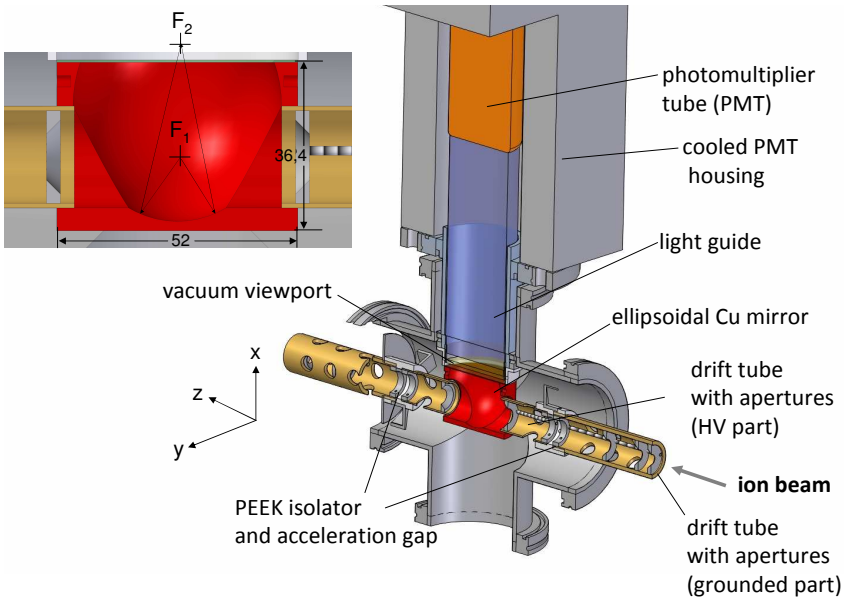

Figure 5.7.: CAD model of the light collection unit. The ellipsoidal collecting mirror can be put on a high voltage in order to perform Doppler tuning on ion beams. The apertures with increasing diameter towards the optical detection unit reduce the stray-light background from the laser beam.

mounted at an angle of 45° which passes the ion beam and detects the current as a function of the oscillation angle. The beam profiles for both beam components can be monitored with an oscilloscope.

The successful improvement of the sensitivity of our spectroscopy setup has recently been demonstrated with the photon-ion coincidence technique [Eas86] with calcium ions, which is part of a diploma thesis [Sie10]. The detector designed for this purpose uses a commercial DeTech 470 secondary electron multiplier (channeltron) to detect the secondary electrons from the impact of the ions or atoms on a copper conversion dynode. For the detection of ions the beam can be deflected on to the dynode by a pair of electrodes. For the detection of atoms a conversion electrode that is also used to reflect the laser beam out of the beam line can be moved into the beam axis with an air-actuated linear feedthrough. The detector unit is housed in a standard Iso-K160 cross and therefore very compact.

A detection efficiency of $\approx 60\%$ has been demonstrated and it was possible to clearly identify a resonance from 10^4 ions/s after about 20 min with the coincidence unit, while the purely optical detection did not even show an indication for a resonance after the same time.

5.8. Overall beam transport properties

After simulating and designing the individual parts of the setup, the transmission through the complete TRIGA-LASER beamline was studied and optimized. This was done for the beam from the offline source and for "online" beams, starting in front of the switchyard. The results give an idea for the voltages needed for first experimental tests and first estimates of the transport efficiency. For the offline beam transmission the beam extracted as described in Sec-

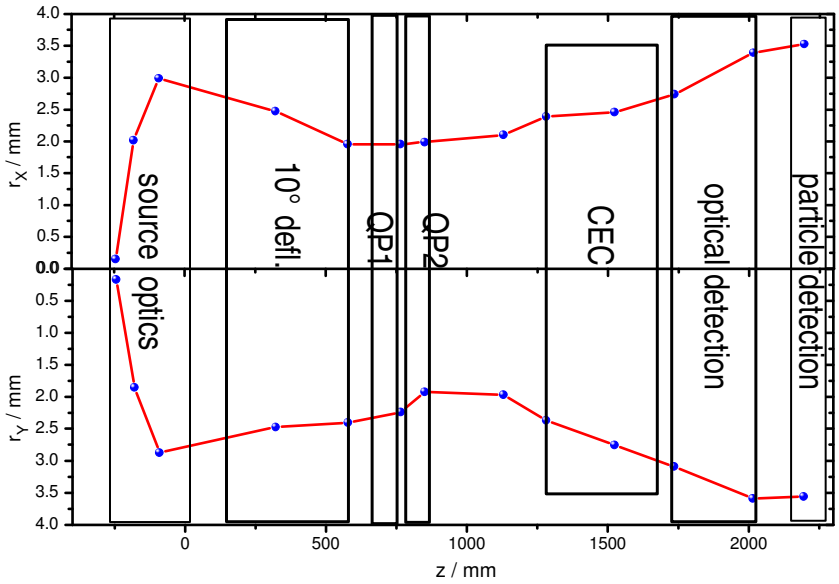

Figure 5.8.: Simulated beam envelope for both transversal beam components (x/y) for the offline beam with ϵ=10π mm mrad at 10 keV energy. The boxes representing the individual devices are scaled to represent the respective free aperture. The total ion transmission was simulated to be 97%.

tion 5.3 was guided through the line and the voltages were manually tuned to reach a maximum transmission of 97%. The simulated beam envelope for the transmission through the whole experimental setup for both transversal beam components is shown in Fig. 5.8. The voltages for the electrostatic elements are given in Tab. 5.1. The main losses occur in the charge-exchange cell and on the apertures of the optical detection unit.

For the online case three different beam initial conditions were studied. At first, the transport of cooled ions with 30 keV kinetic energy, extracted from the cooler with an emittance of $\approx$8 π mm mrad [Lun09] and ions coming directly from the magnet separator with an emittance of $\approx$20 π mm mrad and $\approx$30 π mm mrad which are typical values for the ISOLDE ion source and were adopted for this study. The initial beam diameter was fixed to 7 mm and only the divergence angle was changed to fulfill the different phase-space conditions. The efficiency for the transmission of the cooled beam was optimized to 98% with voltages for the ion-optical elements given in Tab. 5.1. The uncooled beams are transported with significantly lower efficiencies because of losses mainly in the CEC. From the 20 π mm mrad 76% of the ions reach the detection plane at the end of the beamline. The 30 π mm mrad beam is transported with 50% efficiency. The beam envelope as a function of the beam z-coordinate for the cooled low-emittance beam is shown in Fig. 5.9. It is clearly visible that the switchyard causes a beam distortion, focussing the beam only in the plane where the deflection takes place, but the two quadrupole doublets (QPI and QPII), one behind the switchyard and one following the 10° deflector allow to form a beam in the CEC and the light detection unit with only a small elliptical deformation. This is sufficient for a good spatial overlap of laser and ion beam for collinear laser spectroscopy and the moderate divergence of the beam after the light collector still allows an efficient ion counting, since the conversion dynode of the particle counter can accept beam diameters of up to 20 mm.

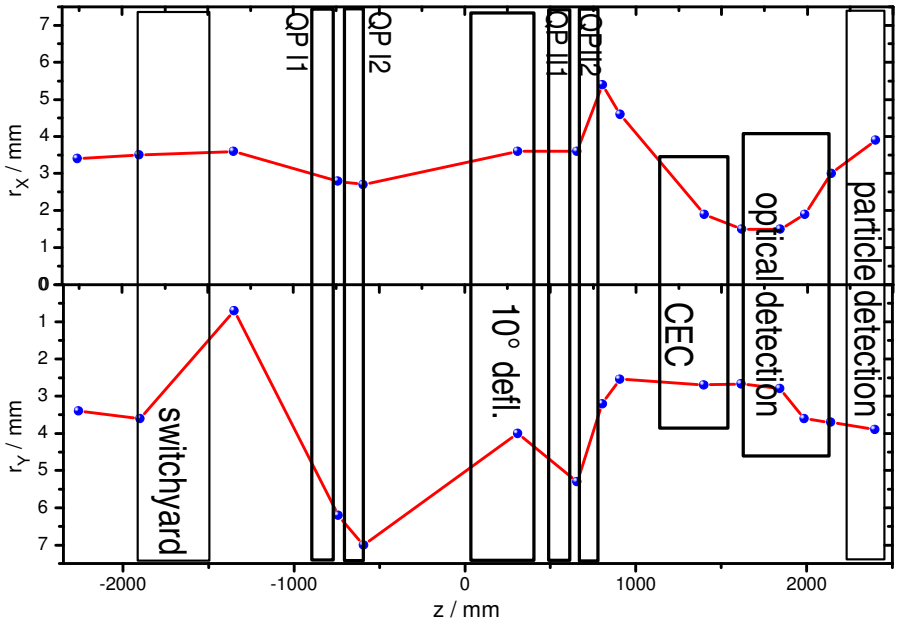

Figure 5.9.: Beam envelope for a cooled ion beam with ϵ=8 π mm mrad at 30 keV starting in front of the switchyard. The transmission was simulated to be 98%.

Table 5.1.: Ion optics voltages for best transmission of the different beams extracted from SIMION simulations. For the positions of the different devices refer to Fig. 5.15.9 and 5.8

beamline element	offline source	uncooled "online"	cooled "online"
beam energy / keV	10	30	30
beam emittance / π mm mrad	10	20	8
switchyard kicker / V	-	±3000	±3000
switchyard bender / V	-	±2760	±2760
source lens / V	5700	-	-
quadrupole QPI 1 / V	-	±390	±390
quadrupole QPI 2 / V	-	∓350	∓350
10° deflector / V	±1050	±3180	±3180
quadrupole QPII 1 / V	±55	±150	±200
quadrupole QPII 2 / V	∓55	∓250	∓190

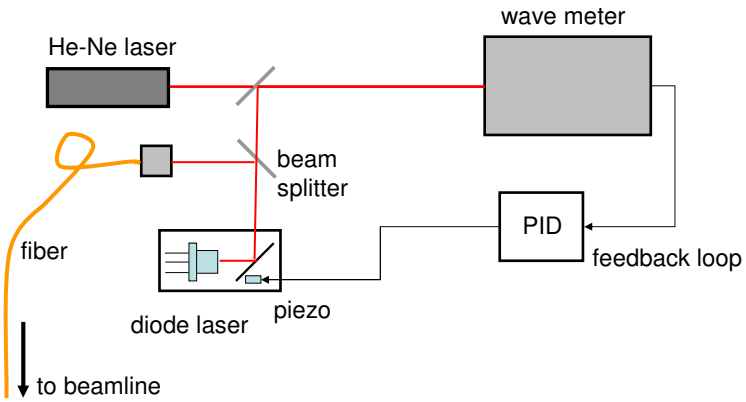

Figure 5.10.: The laser system used for the first tests with stable rubidium atoms. The laser was frequency-stabilized with a wavemeter and the light was guided to the experiment with a fiber.

5.9. The Laser System for the First Test on Rb Atoms

For the first laser spectroscopy tests with rubidium atoms a diode laser setup was used to produce the 780 nm probe laser light. A schematic view of the laser system is shown in Fig. 5.10. The Toptica DL100 laser was frequency stabilized by a HighFinesse WS7 wavelength meter which was calibrated prior to each measurement with a two-mode stabilized helium-neon laser. In the wavemeter control program the set wavelength is compared to the actual value to produce an error signal. After processing with a digital PID regulator, this feedback signal is sent to the piezo actuator of the diode-laser grating for wavelength tuning. Under stable conditions concerning ambient temperature and air pressure, a frequency error of only 6 MHz in 8 h was observed. However, it should be noted that this measurement was done in the laser laboratory and not in the reactor experimental hall.

The stabilized output of the laser was transported to the entrance window of the apparatus with a fiber, where the coupling to the beamline was accomplished by a set of mirrors and iris apertures. To ensure high transmission of the linearly polarized laser and a low level of scattering light the entrance and exit quartz windows were installed at the Brewster angle of 57.2°. Together with a careful adjustment of the laser beam through the beamline with the help of the adjustable apertures in front and behind the CEC, a transmission of 96% could be reached. The diameter of the well collimated laser inside the light collection unit was adjusted to be ≈4 mm offering enough distance from the edges of the small apertures of the CEC to keep scattered light in the detector on a reasonable level and ensure a reasonable overlap with the ion beam according to Fig. 5.9 and Fig. 5.8. The details of the laser background and its impact on the overall performance of the fluorescence detection will be discussed in the Ch. 6.2.2

5.10. Data Acquisition and Experiment Control

The primary task of the experiment control is to acquire the counts from the photomultiplier as a function of the voltage applied to the charge-exchange cell or the optical detection unit, and to measure this voltage with high precision. The implementation of all static voltages for the ion-optical devices in a common control system is planned for the future and has recently

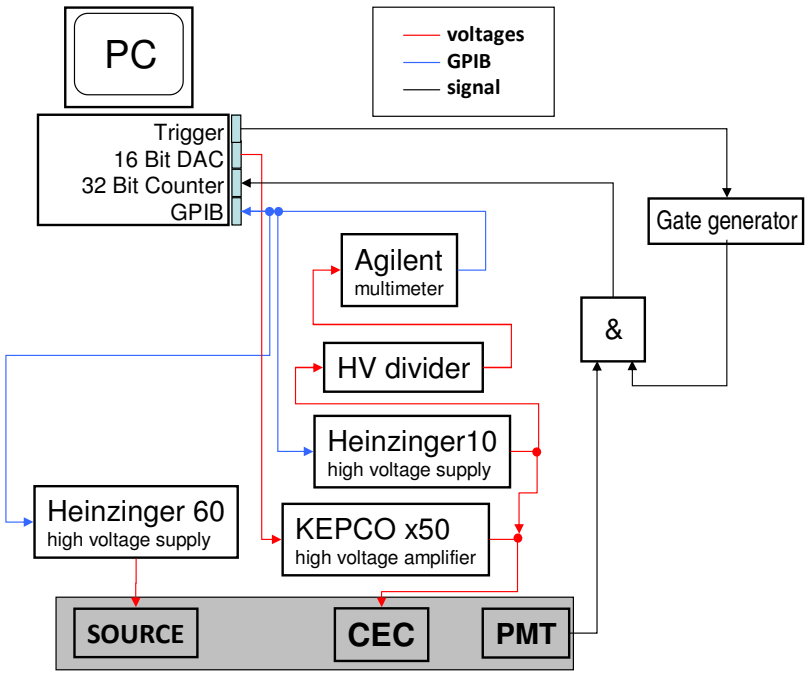

Figure 5.11.: Schematic of the data acquisition and the experiment control. The shown configuration is used for scanning the voltage either with the Kepco amplifier or with the Heinzinger 10 kV supply. For further details refer to the text.

started as a diploma thesis [Ham10].

The data acquisition program was created in LabView and allows communicating with the Heinzinger high-voltage supply and the Agilent precision multimeter via GPIB. The Kepco amplifier is controlled by the DAC of a multi I/O card also providing four 32 Bit counter channels used for the pre-processed TTL-pulses from the photomultiplier counting electronics. The program records the number of counts for each measurement step of typically 20 ms (dwell time) as a function of the DAC voltage for the Kepco amplifier or the Heinzinger supply which are ramped during one scan. A pre-defined number of total scans allows integrating individual scans directly. Because of timing problems with the PC-based LabView and other background processes which affected the dwell time during the first tests, the measurement gate was created externally by a NIM digital gate generator and a coincidence unit. Fig. 5.11 shows the schematic of the experiment control.

6. Off-line Commissioning of TRIGA-LASER

For a first performance test of the experimental setup the search for an easy solution concerning ion production and required laser system, but still with the ability to also test the charge-exchange cell, led to rubidium as an ideal test candidate. The infrared wavelength of the $5\,^2S_{1/2} \rightarrow 5\,^2P_{3/2}$ D2 transition of 780 nm in the atom is easily supplied by a low-priced laser diode in a relatively simple external cavity setup and the ions can easily be produced by surface ionization in a hot cavity.

6.1. Beam Transport and Charge Exchange

The results presented in this section are mainly based on beam intensity measurements with Faraday cups. In some cases the adjustable apertures were used as charge collectors to extract the ratio of ions passing the charge-exchange cell. The current was measured with a Keithley 6485 picoamperemeter.

For the intensity measurement of the atom beam the cylindrical suppressor electrode in the Faraday cup (see Fig. 6.1) was put on positive potential (≈30 V) to extract secondary electrons emitted from the impinging atoms. This electron current was then measured. A calibration measurement with ions showed that with this particular geometry on average three electrons were released per incident particle.

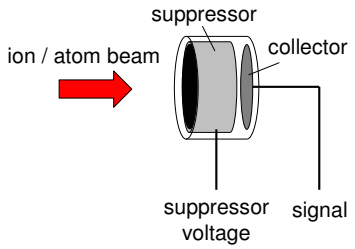

Figure 6.1.: Schematic view of the Faraday cup.

6.1.1. Transport Efficiency and Ion Beam Profiles

The ion beam transport efficiency through the complete setup can only be roughly estimated as it is impossible to measure the ion current in every position of the beamline. Eventual losses in the extraction optics of the ion source for example, cannot be quantified. For a 6 keV rubidium ion beam the efficiency was determined by measuring the current on two identical Faraday cups, one inside the 10° deflection chamber and the other one behind the optical detection unit. After fine adjustments to the ion-optical elements a transmission efficiency of 70% was obtained. The voltage settings for this case are given in Tab. 6.1.

After the installation of two identical adjustable apertures in front of the charge-exchange cell and behind the optical detection system, another transmission test was done by measuring the current on the closed apertures, which is an aluminum plate with a number of apertures of different diameter. The result was a transmission of 71% in agreement with the previous result, showing that losses between the 10° deflection chamber and the CEC are negligible. The voltages applied to the electrodes are also listed in Tab. 6.1. The need for a correction voltage in the 10° deflection chamber shows that the offline source housing and its connection to the setup are not exactly straight and cause the ion beam to enter at a small angle in the vertical plane. The agreement with the simulations that predicted a transmission of 97% (see Chapter 5.8) is

Table 6.1.: Experimental ion-optics voltages for best transmission at two different beam energies given by the ion source potential measured with the Faraday cups for 6 keV and the aperture plates for 10 keV ion beam energy.

beamline element	Faraday cup	aperture plates
beam energy / keV	6	10
source lens / V	4745	7880
10° deflector / V	±595	±1028
10° corr. electr. / V	±156	±72
quadrupole 1 / V	±123	±217
quadrupole 2 / V	∓109	∓182

weak. Most probably, the ion source simulation is not accurate and the actual emittance is significantly larger.

Besides transmission, the beam profile is also essential for the performance of the experiment. Therefore, the profiles were monitored with the vane probe in the Faraday cup chamber and the electrode voltages were further adjusted. A typical beam profile as it is monitored by an oscilloscope is shown in Fig. 6.2. The measurement was done with a 300 pA beam at 10 keV. The extracted 1/e beam diameters are 6 mm for the horizontal plane and 7 mm for the vertical plane showing only a slight elliptical shape of the beam at this position of the beamline. This result is in good agreement with the simulated beam envelope shown in Fig. 5.8 predicting 7 mm diameter.

6.1.2. Charge Exchange of Rubidium Ions with Potassium

The ideal partner for a charge-exchange reaction for an ion is the atom of the same element, as this resonant process offers the highest cross section. In the case of rubidium the usage of the pure metal holds a certain handling risk as it is quite reactive. Therefore, we load the ion source with rubidium nitrate, which is not possible for the charge-exchange cell. We chose to use potassium with an ionization potential of 4.341 eV, only 0.164 eV greater than the IP of rubidium with 4.177 eV [Lid97], allowing a non-resonant charge transfer in the reaction

$$\mathrm{Rb}^+ + \mathrm{K(4s)} \longrightarrow \mathrm{Rb(5s)} + \mathrm{K}^+ - \Delta E. \tag{6.1}$$

Where the energy deficit $\Delta E = 0.164\,\mathrm{eV}$ is taken from the ion's kinetic energy.

Potassium has a melting point of 64 °C [Lid97] and is safely stored in paraffin oil. We inserted an amount of ≈5 g in the reservoir of the CEC and allowed the cell to degas for one night at a medium temperature of 100°C before testing the charge exchange process at higher temperatures. To detect the atoms after neutralization the residual fraction of ions was reflected out of the central beamline by the kicker electrodes on the charge exchange cell.

The charge-exchange efficiency measurement was done with increasing oven temperatures and different ion energies ranging from 2 keV to 10 keV for each temperature. The result of this measurement is shown in Fig. 6.3. The uncertainties are mainly attributed to the uncertainty in the current measurement of ≈1 pA. Efficiencies of almost 100% can be obtained regardless of the ion energy at temperatures greater than 200°C.

The curves can be described with a simple model for the attenuation of a particle beam moving through a medium with a reaction cross section σ, according to [Has64]:

$$\epsilon = 1 - \exp\left(-n\sigma l\right). \tag{6.2}$$

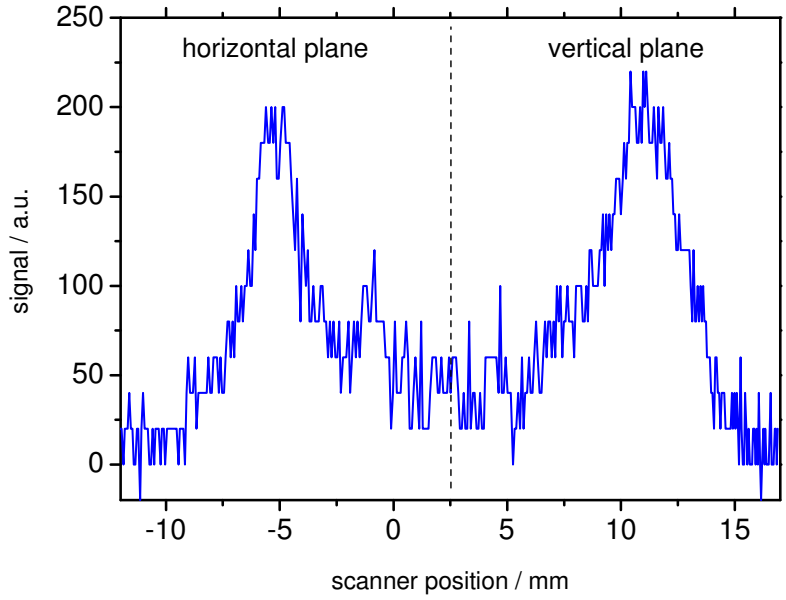

Figure 6.2.: Ion beam profile recorded with the vane probe for a beam current of 300 pA. The $1/e^2$ beam diameters for the slightly elliptically deformed beam are 6 mm for the horizontal plane and 7 mm for the vertical plane.

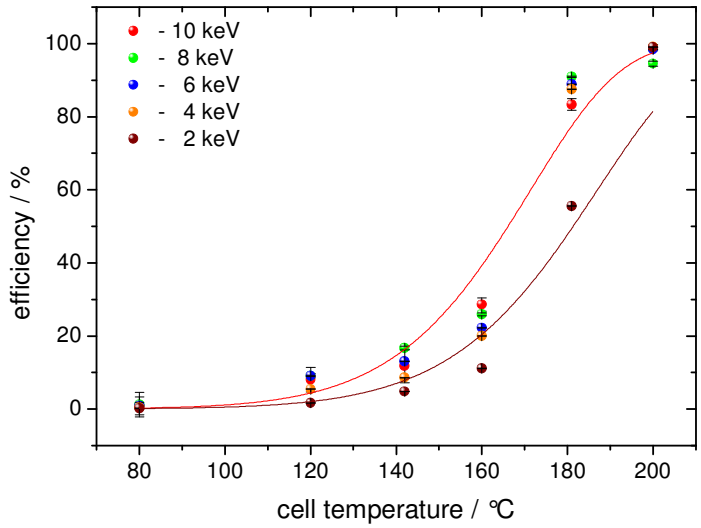

Figure 6.3.: Charge exchange efficiencies for different ion energies as a function of the cell temperature. The curves show fits with the model described in the text, allowing to extract the charge-exchange cross sections.

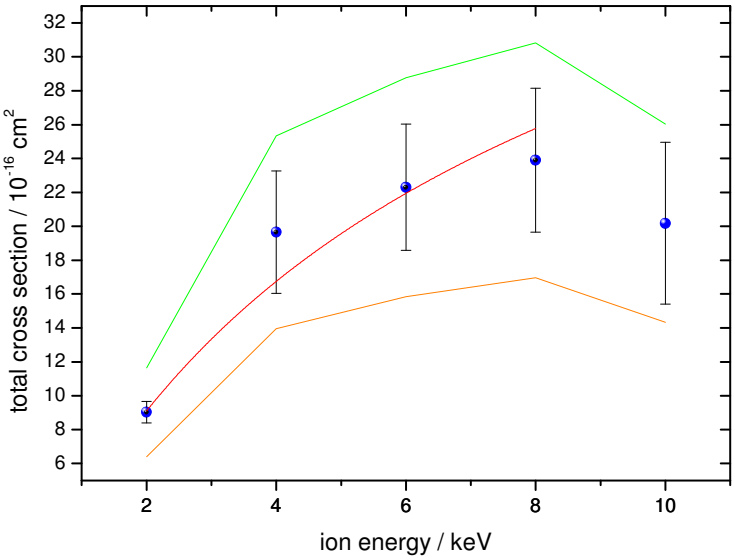

Figure 6.4.: Charge-exchange cross sections for the non-resonant charge transfer between Rb^+ and K. The error bars refer to the statistical error from the fit to the efficiency data shown in Fig. 6.3. The two outer curves represent the confidence band due to the systematic uncertainty caused by the unknown interaction length in the charge-exchange cell. There is a significant increase in the cross section with a local maximum, which is typical for this type of reaction [Per65]. A fit to the data according to Eq. 6.4up to an energy of 8 keV is indicated by the solid red line.

Where l is the length of the interaction region and n is the atom density of the medium. Replacing n with a parametrization of the vapor pressure of liquid potassium as a function of the temperature [Alc84], one obtains

$$\epsilon = 1 - \exp\left(-\frac{10^{-\frac{4453\,K}{T}+4.402} N_A \sigma l}{V_{\mathrm{mol}}\, p_0}\right), \tag{6.3}$$

with the constants N_A the Avogadro number, V_{mol} the standard volume per mol and p_0 the standard pressure. The vapor pressure in the active region of the CEC deduced from the parametrization for 200°C is $P_{\mathrm{vap}} = 10^{-4453\,K/473\,K+4.402} = 1 \times 10^{-2}$ mbar while the ambient pressure in the vacuum chamber remains unchanged at 1×10^{-6} mbar. This shows that the condensation and reflow of the potassium at the outer cooling blocks, which were kept at temperatures of 45°C, works nicely[1].

A fit to the data with the cross section as a free parameter results in the values for σ shown in Fig. 6.4. An interaction length of 7±2 cm was assumed, as the precise extension of the K vapor cloud inside the CEC is unknown and can only be estimated. Therefore the large systematic uncertainties on the cross sections marked by the two limiting curves. It was shown for other combinations of alkali ions and vapor [Per65], that the non-resonant cross sections are of the order of $10^{-15} - 10^{-16}$ cm^2 and that the global trend of the cross section follows the relation

[1] The CEC is now operational for more than one year without refill.

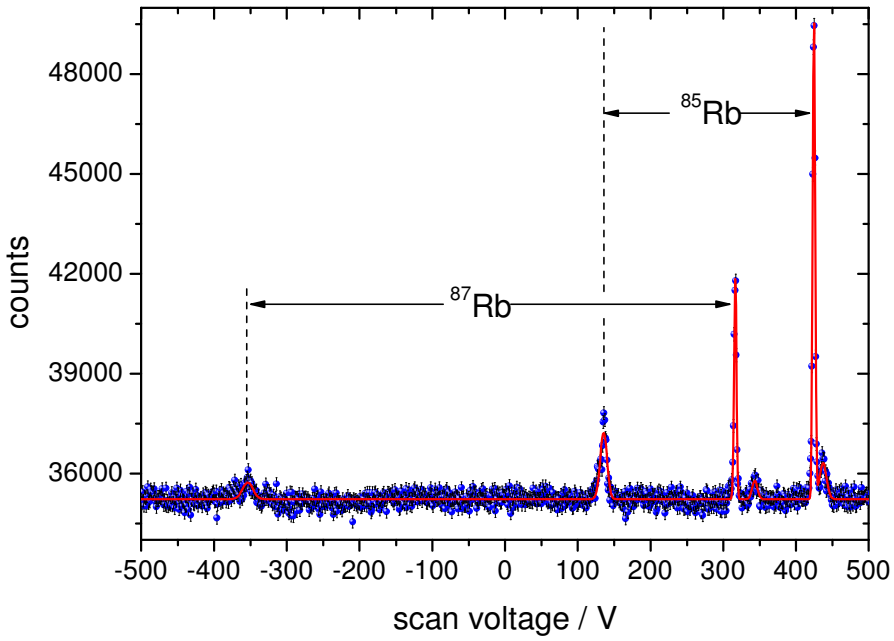

Figure 6.5.: Full hyperfine spectra for the stable Rb isotopes recorded in one measurement. The spectra are the sum of 10 individual scans taken with 1 V steps and a dwell time of 20 ms. The laser power was 1 mW and the atom intensity was 1.2×10^8 atoms/s.

[Per65]

$$\sigma \propto \exp\left(\frac{-a\Delta E}{h\sqrt{2E_{\mathrm{kin}}/m}}\right), \tag{6.4}$$

with the element specific constant a, the energy deficit ΔE, the ion mass m and Planck's constant h. This relation is valid until a maximum is reached for a certain energy depending on ΔE. Above this value the cross section decreases monotonically with increasing particle energy as in the case of the resonant charge exchange. Our results are in good agreement with this, reproducing the correct order of magnitude and showing a maximum at 8 keV. A fit to the data excluding the cross section for 10 keV, which is already decreasing, is shown by the solid red line. Unfortunately, the behavior for higher energies cannot be studied so far, because of the limited high-voltage specifications of the offline-source cage.

For further laser spectroscopy tests, a cell temperature of 140°C was chosen in most cases in order to increase the lifetime of the CEC and the potassium filling and for convenient heating and cooling times. This offers a charge-exchange efficiency of ≈ 10%. It will be shown later, that besides the charge exchange reaction further collisions may occur at higher cell pressures, which change the kinetic energy of some atoms, leading to a visible effect in the lineshape of the laser spectroscopic resonances (see Ch. 6.2.4).

6.2. Collinear Laser Spectroscopy with Stable Rubidium Atoms

The ion beam transport tests and the commissioning of the charge-exchange cell were only preparatory work for the main task of the setup: collinear laser spectroscopy on a fast atomic beam. A full hyperfine spectrum for both naturally abundant isotopes ^{85}Rb and ^{87}Rb recorded

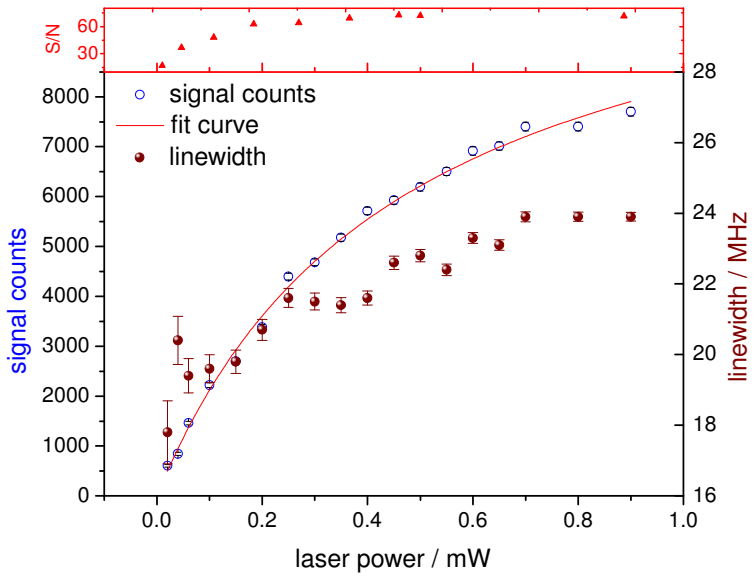

Figure 6.6.: Saturation curve with observed linewidth and signal-to-noise ratio. The saturation power from the fit to the maximum count rate is $P_{\mathrm{sat}} = 0.46(1)\,\mathrm{mW}$. Above 0.5 mW the S:N ratio shows no increase any more. The linewidth shows a moderate but significant increase with increasing power.

in anti-collinear geometry is presented in Fig. 6.5. The 10 individual scans were performed with 1 V steps from the Kepco amplifier and a dwell time of 20 ms. The laser power was 1 mW at a wavenumber of $12810.2000\,\mathrm{cm}^{-1}$ and the (corrected) atom current was 20 pA, corresponding to $1.2{\times}10^8$ atoms/s. A rough fit to the individual components was done with single Gaussian profiles to guide the eye. A more detailed analysis will follow in Ch. 6.2.3.

6.2.1. Saturation Power and Signal-to-Noise Ratio

The experimental determination of the transition-saturation power is necessary for later experiments, in order to apply a laser power that delivers sufficiently high signals without significant power broadening [Dem93]. In addition, the comparison with the theoretical saturation intensity allows a conclusion about the actual diameter of the spatial overlap between laser and atom beam. To obtain the saturation characteristic, the strongest hyperfine component of ^{85}Rb was recorded with a step size of 0.5 V and Gaussian lineshapes were fitted to the resonances. The maximum count rate and the fitted linewidth (FW1/e^2) are plotted as a function of the laser power in Fig. 6.6. On top of the graph, the signal-to-noise ratios *i.e.* signal/$\sqrt{\text{background}}$ for the individual measurements are given. The measurement reveals that it is not beneficial to go higher in laser power than 0.5 mW, as the signal-to-noise-ratio does not increase any more. The saturation curve was fitted with the relation [Dem93]

$$\text{Signal} = C \times \frac{\frac{P}{P_{\mathrm{sat}}}}{1 + \frac{P}{P_{\mathrm{sat}}}}\,, \tag{6.5}$$

with C and P_{sat} as fitting parameters yielding $P_{\mathrm{sat}} = 0.46(1)\,\mathrm{mW}$. With the estimated laser beam diameter of 4 ± 1 mm, larger ion beam diameter and rectangular profiles as an approximation,

one obtains for the saturation intensity of the D2 transition $I_{\mathrm{sat}} = 3.7(9)\,\mathrm{mW/cm^2}$, which is in good agreement with the theoretical value of $I_{\mathrm{sat}}^{\mathrm{theo}} = 3.05\,\mathrm{mW/cm^2}$ [Ste01a].

6.2.2. Performance of the Fluorescence Detection System

The overall efficiency of the optical detector is composed of the geometric efficiency of the collecting ellipsoidal mirror ϵ_{geo}, the transmission of the inverted viewport and the light guide $\epsilon_{\mathrm{trans}}$, and the quantum efficiency of the photomultiplier QE according to

$$\epsilon_{\mathrm{total}} = \epsilon_{\mathrm{geo}} \times \epsilon_{\mathrm{trans}} \times QE. \tag{6.6}$$

The experimental observable is the number of real fluorescence counting events on top of the background at resonance per time unit, divided by the number of atoms that passed the detector in the same time interval. For our test experiment with naturally abundant ^{85}Rb (72%) and the calibration of the Faraday cup as described in section 6.1.2, this leads to the expression

$$\epsilon_{\mathrm{total}} = \frac{\mathrm{signal}}{j_{\mathrm{atoms}} \times 0.72 \times N_{\mathrm{scans}} \times t_{\mathrm{dwell}}}, \tag{6.7}$$

with an atom flux of $j_{\mathrm{atoms}} = I_{\mathrm{atoms}}^{\mathrm{cup}} \times 1/3$. N_{scans} is the number of accumulated scans and t_{dwell} is the measurement time per channel. In Fig. 6.7 the resonance which was used to extract the best value of $\epsilon_{\mathrm{total}} = 1\,\mathrm{photon}/356\,\mathrm{atoms}$ for the total efficiency is shown.

Because of the lack of mass separation in the beam, any contamination of the ion beam would lead to underestimated values for the measured efficiency and the real efficiency will scale linearly with the fraction of impurities. In order to further increase the number of detected photons per atom the reflectivity of the mirror could be optimized, which so far only has a copper surface polished by hand.

In order to get an idea about the performance of the detector in comparison with similar devices, our results were compared to the existing fluorescence detection setup used at ISOLDE in the COLLAPS experiment[Neu81]. The setup there consists of a 20 cm long mirror and in the case of Mg and Be ions (UV) two lens stages and two photomultipliers. For infrared wavelengths as in the case of Ba a light guide was used to collect the light from the chamber. For a real comparability of the efficiencies of the different detectors $\epsilon_{\mathrm{total}}$ was normalized by the quantum efficiency to account for the different photomultipliers used, the different transition strengths by the Einstein B coefficient [Dem93], and the different numbers of excitation cycles per meter in the detector volume by the atom/ion velocity v multiplied by the excited-state life time τ. The normalized efficiency can be expressed as

$$\epsilon_{\mathrm{geo}}^{\mathrm{norm}} = \frac{\epsilon_{\mathrm{total}}}{QE \times B \times v \times \tau}. \tag{6.8}$$

In this way of comparing the individual detectors the present setup shows an excellent performance with 14 times higher efficiency compared to the present COLLAPS detector (see Table 6.2). Results of detector simulations with the optical ray tracing software FRED [Eng10] are shown as bar chart in Fig. 6.8. The calculated efficiencies were normalized to the measured efficiency at TRIGA-LASER. The ray-tracing simulations [Ham10] show excellent agreement with the measured results. Only the performance of the Ba detection setup was predicted to be better, which may be caused by transmission losses in the light guide that are not included in the simulation.

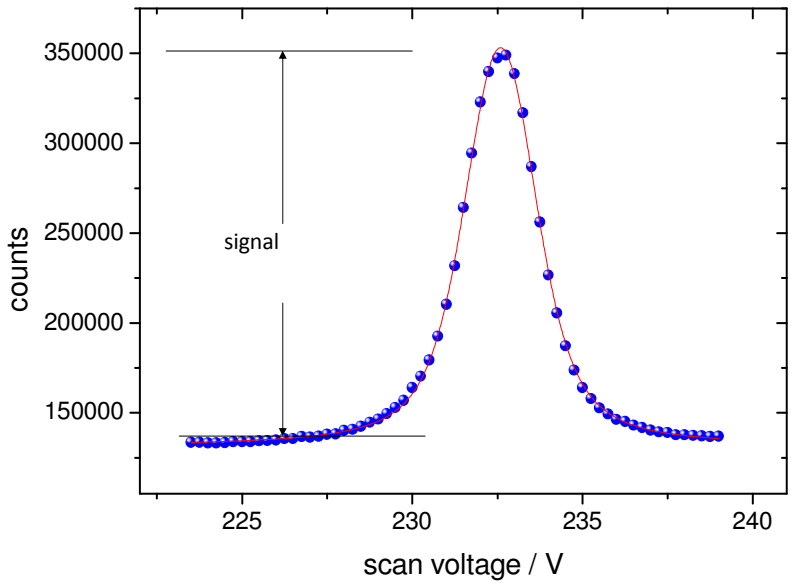

Figure 6.7.: Resonance scan used to extract the best value of the efficiency. $\epsilon_{\text{total}} = 1\,\text{photon}/356\,\text{atoms}$ could be obtained and reproduced in several independent measurements. The resonance is the sum of 50 scans with 20 ms dwell time and the Faraday cup current was 49 pA.

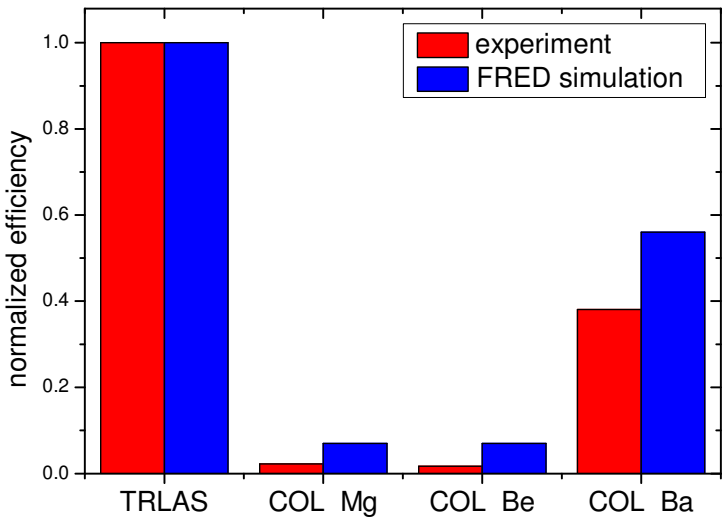

Figure 6.8.: Comparison of the normalized efficiencies as obtained in ray tracing simulations (see text) and in experiments for the detection system used in this work (TRIGA-LASER) and at different optical detection systems from COLLAPS. The relative efficiencies calculated for the different setups are in good agreement with the respective experimental results. The optical detection systems for Mg and Be are identical, which is reproduced by this comparison and indicates consistency of the applied normalization.

Table 6.2.: Detector efficiencies, normalized efficiency $\epsilon_{\text{geo}}^{\text{norm}}$ and noise-normalized efficiency ϵ_{noise} as defined in the text. All values required for the calculation according to Eq. 6.8 and Eq. 6.9 are included for the four detector setups.

Experiment	TRIGA-LASER	COLLAPS Ba	COLLAPS Mg	COLLAPS Be
Reference	This work	[Neu81]	This work	[Gep10]
ϵ_{total}	2.9×10^{-3}	1.0×10^{-2}	5×10^{-4}	8.3×10^{-5}
QE / %	5	20	25	20
τ / ns	26.3	8.4	3.9	8,7
Background / 1/s	200 000	15 000	15 000	15 000
B / 10^{20} m/kg	10.8	12.1	3.4	2.1
v / 10^5 m/s	1.51	2.06	6.34	10.8
$\epsilon_{\text{geo}}^{\text{norm}}$ /10^{-26} a.u.	20.5	7.15	1.44	1.74
ϵ_{noise} / 10^{-29} a.u.	10.5	26.1	5.87	6.72
$\boldsymbol{\epsilon_{\text{geo,rel}}^{\text{norm}}}$	**1**	**0.34**	**0.069**	**0.088**
$\boldsymbol{\epsilon_{\text{noise,rel}}}$	**1**	**2.49**	**0.56**	**0.64**

Besides efficiency, the background level in the detection section is defining the overall performance of an optical detector and therefore needs to be taken into account. Here the main contribution to the noise is treated as statistical fluctuations of the stray light caused by the laser. In this case $\epsilon_{\text{geo}}^{\text{norm}}$ is modified by the noise, *i.e.* the square root of the background count rate per mW of incident laser power. Again, to correct for the influence of the photomultiplier's quantum efficiency on the background rate, the result is multiplied by the square root of the quantum efficiency according to

$$\epsilon_{\text{noise}} = \epsilon_{\text{geo}}^{\text{norm}} \times \sqrt{\frac{QE}{\text{background}}} \tag{6.9}$$

and is called noise-normalized efficiency. From this point of view the TRIGA-LASER optical detection unit is performing similar well as the existing systems at ISOLDE because its performance measure is slightly reduced by the high background level. In Table 6.2 the results are summarized.

A more practical figure for the efficiency of an optical detector is the minimal particle beam intensity needed to get a visible signal in a reasonable time. Currently, with the TRIGA-LASER setup developed in this work a signal-to-noise ratio of 2 in a resonance scan of 20 points can be reached for rubidium in a 6 h integration time with a beam intensity of only 1×10^4 particles/s, assuming stable voltages and a laser that is stable in intensity and frequency (see Ch. 6.2.5).

At the present status our detector is competitive, although we suffer from the rather high background level. Further optimization of the apertures in the beamline, especially right after the Brewster windows, may reduce the background and, hence, the noise. This will be subject to further studies together with a completely new design of the light collector [Ham10] using a combined approach of imaging and non-imaging optics.

6.2.3. Resolution and Accuracy of the Collinear Setup

The high-voltage divider used to measure the voltages applied to the charge-exchange cell was calibrated with the Heinzinger PNChp10000 high voltage supply, which is specified to be accurate

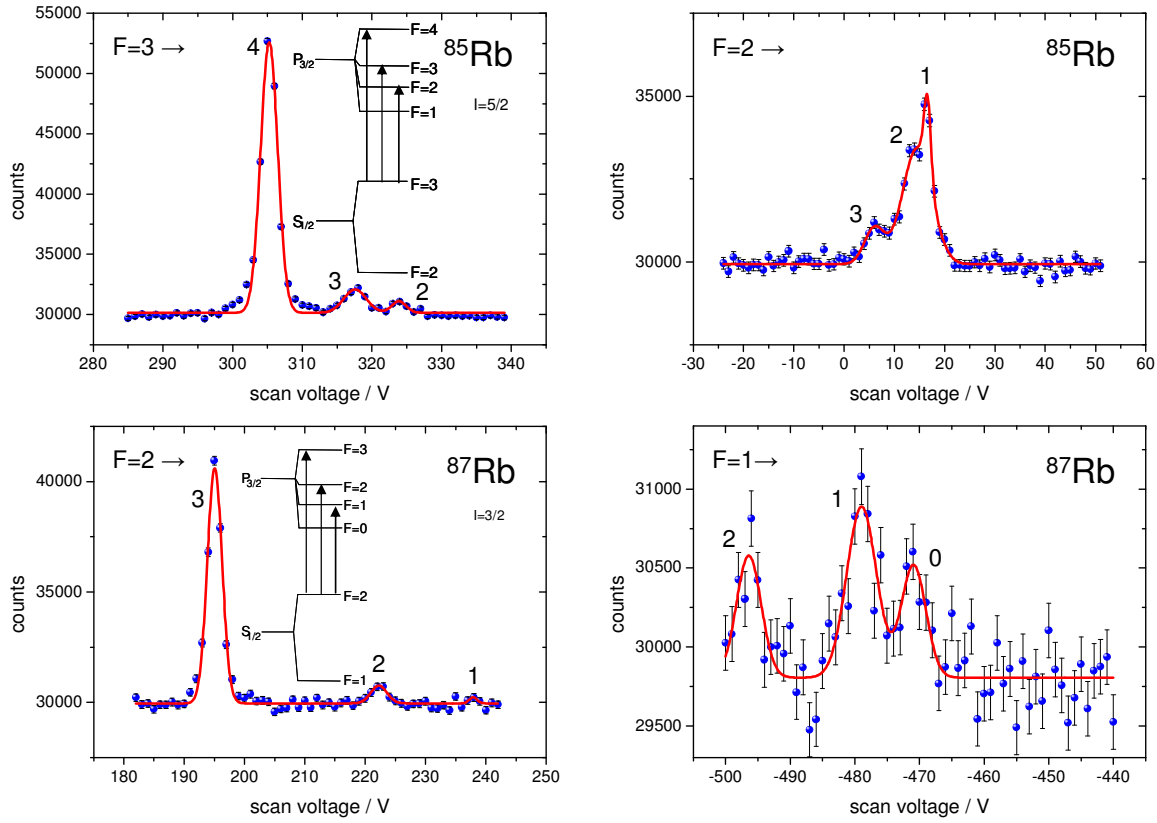

Figure 6.9.: Hyperfine multiplets of the two stable rubidium isotopes. The assignment of the transitions was done according to the selection rules for dipole transitions. The resonances were fitted with Gaussian profiles of one common FWHM. The center positions, the intensities, the baseline and the linewidth (FWHM) were free fitting parameters. In Tab. 6.3 the results of the extracted level spacings are shown in comparison to literature values.

in voltage to 2×10^{-4}. This yielded a divider ratio of $D = 1001.212(5)$. With this voltage divider the Kepco high voltage amplifier could be calibrated and an amplification factor of $f_{\mathrm{Kepco}} = 50.09$ was extracted.

The experimentally well known hyperfine structure and the isotope shift of ^{85}Rb to ^{87}Rb [Ste01a] were studied in detail to investigate the resolution and the accuracy of our experiment. The measurement was performed with the Kepco amplifier and a source voltage of 9976 V measured with the voltage divider. The laser was stabilized to 12810.1633 cm^{-1} throughout the measurement. The individual peaks of the hyperfine multiplets were fitted with Gaussian profiles for the extraction of the hyperfine structure parameters. A more detailed discussion about the line shape will follow later. In Fig. 6.9 the multiplets are shown together with the assignment of the individual transitions. All peaks from allowed transitions are visible and even the closely neighboring peaks in the $F = 2$ multiplet of ^{85}Rb can be separated. Also transitions which are subject to hyperfine pumping (in the ^{85}Rb $F = 2$ and the ^{87}Rb $F = 1$ case) are visible, showing the advantage of a short distance between the charge-exchange cell and the detector. Tab. 6.3 compares the extracted hyperfine splittings with the literature values taken from [Ste01a]. The frequencies were calculated from the voltage differences in non-relativistic

Table 6.3.: Comparison of the measured hyperfine splittings and the isotope shift with literature values. Splittings are listed with respect to the strongest transition of each multiplet. The ground state (g.s.) splitting and the isotope shifts are listed separately in the last two lines. The reference values were taken from [Ste01a]. The first error given is the statistical error from the fit and the second error is the systematic error because of the 10^{-4} uncertainty in the absolute voltages.

^{85}Rb			^{87}Rb		
	Our exp./MHz	Ref./MHz		Our exp./MHz	Ref./MHz
F=3→4	0	0	F=2→3	0	0
F=3→3	121(2)(7)	120.640(68)	F=2→2	266(3)(7)	266.650(9)
F=3→2	183(2)(7)	184.041(91)	F=2→1	418(6)(7)	423.597(7)
F=2→3	0	0	F=1→2	0	0
F=2→2	68(4)(7)	63.401(61)	F=1→1	162(5)(7)	156.947(7)
F=2→1	99(3)(7)	92.773(90)	F=1→0	239(4)(5)	229.165(4)
g.s splitting	3034(1)(6)	3035.732	g.s. splitting	6835(1)(6)	6834.682
			Isotope shift	-77(2)(5)	-78.0955(15)

approximation according to

$$\delta\nu\left(U_1, U_2\right) = \nu_{\text{laser}} \times \sqrt{\frac{2}{mc^2}} \left(\sqrt{U_2^{\text{ges}}} - \sqrt{U_1^{\text{ges}}} \right) . \tag{6.10}$$

The results are summarized in Tab. 6.3 and are in excellent agreement with literature values. For example, the observed ground-state hyperfine splittings show a relative deviation of only 6×10^{-4} and 1×10^{-4} from the literature values for ^{85}Rb and ^{87}Rb, respectively, demonstrating that the setup is already at a status to perform high-accuracy spin and magnetic moment measurements. Furthermore, the determined isotope shift of $\delta\nu_{IS}^{87,85} = -77(2)\,\text{MHz}$ is also accurate.

The statistical uncertainties were calculated based on the fitting uncertainties for the resonance centers. The systematic uncertainties are mainly due to the uncertainties of the voltages applied to the ion source and the charge-exchange cell. For the ion source voltage an uncertainty of $\Delta U_{\text{source}} = \pm 0.5\,\text{V}$ was assumed as the actual potential the ions are produced at is unknown because of the voltage gradient across the ionizer tube (see Ch. 5.3). A quarter of this voltage gradient was therefore assumed as the uncertainty. The post-acceleration voltage of the charge-exchange cell is produced by the DAC voltage with a specified relative uncertainty of $\Delta U_{\text{DAC}}^{\text{rel}} = \pm 10^{-4}$ multiplied by the Kepco factor with an uncertainty of $\Delta f_{\text{Kepco}} = \pm 5 \times 10^{-5}$. The total systematic voltage uncertainty was calculated by

$$\Delta U_{\text{sys}} = \pm \sqrt{\Delta U_{\text{source}}^2 + \left(\Delta f_{\text{Kepco}} U_{\text{DAC}}\right)^2 + \left(\Delta U_{\text{DAC}}^{rel} U_{\text{DAC}} f_{\text{Kepco}}\right)^2} , \tag{6.11}$$

according to Eq. 5.1. The uncertainties of the frequency differences were calculated based on Eq. 6.10 with the expression

$$\Delta\delta\nu^{1,2} = \pm \frac{\nu_{laser}}{2} \sqrt{\frac{\left(\Delta U_1\right)^2}{U_1 mc^2} + \frac{\left(\Delta U_2\right)^2}{U_2 mc^2}} . \tag{6.12}$$

The line width of the observed resonances in Fig. 6.9 is below 25 MHz and thus only 4 times larger than the natural linewidth of 6 MHz. From the Doppler compression of a thermally

distributed ensemble (refer to Ch. 3.2) one would expect a residual line width matching the natural line width. The observed broadening cannot be attributed to a divergence in the beam which is limited to about 3 mrad in our setup for good transmission, but to the voltage gradient in the ion source. Depending on the origin of ionization, the ion's initial potential varies along the ionizer tube leading to an increase of the actual velocity spread and to additional Doppler broadening. The 10 kV total acceleration voltage results in a differential Doppler shift of $\approx$ 10 MHz/V. The observed width therefore corresponds to only 2 V variation of the potential the ion is produced at, which can be expected with our source configuration. With a different type of surface ion source with indirect heating (*e.g.* electron impact heating), the resonances should become significantly narrower.

6.2.4. The Charge Exchange Process and its Impact on the Line Shape

In Ch. 6.1.2 it was already discussed that the charge exchange reaction leads to a small energy loss of all particles of the order of 0.1 V due to the energy gap in the ionization potentials between K and Rb. This energy deficit however, does not change the line profile. To fully understand the observed line shape, which to the first order can be described by a Voigt profile [Dem93], other reactions besides the charge exchange to the ground state of Rb have to be taken into account. There are several possible inelastic reactions contributing to the additional energy loss of some of the particles passing the charge-exchange cell [Ben86]:

$$\mathrm{Rb}^+ + \mathrm{K}\,(4s) \rightarrow \mathrm{Rb}^+ + \mathrm{K}\,(4p) - \Delta E \rightarrow \mathrm{Rb}^+ + \mathrm{K}\,(4s) - \Delta E + h\nu\,, \tag{6.13}$$

if the collision occurs prior to the neutralization, or for inelastic collisions after the charge exchange reaction, *e.g.*

$$\mathrm{Rb}\,(5s) + \mathrm{K}\,(4s) \rightarrow \mathrm{Rb}\,(5s) + \mathrm{K}\,(4p) - \Delta E \rightarrow \mathrm{Rb}\,(5s) + \mathrm{K}\,(4s) - \Delta E + h\nu\,, \tag{6.14}$$

where the potassium gets excited and

$$\mathrm{Rb}\,(5s) + \mathrm{K}\,(4s) \rightarrow \mathrm{Rb}\,(5p) + \mathrm{K}\,(4s) - \Delta E \rightarrow \mathrm{Rb}\,(5s) + \mathrm{K}\,(4s) - \Delta E + h\nu\,, \tag{6.15}$$

for an excitation of the rubidium atom. A third type of reaction is the charge exchange into the first excited state of rubidium:

$$\mathrm{Rb}^+ + \mathrm{K}\,(4s) \rightarrow \mathrm{Rb}\,(5p) + \mathrm{K}^+ - \Delta E \rightarrow \mathrm{Rb}\,(5s) + \mathrm{K}^+ - \Delta E + h\nu\,. \tag{6.16}$$

The energy deficit ΔE corresponds to the energy gap of ≈ 1.6 eV between the ns ground state and the np first excited state of the potassium or the rubidium atom, respectively and results in a shift in the resonance position. The analysis of the observed spectra shows that one reaction of this type is not sufficient to fit the data satisfactorily. Depending on the cell temperature a significant amount of particles have suffered from two inelastic collisions. Fig. 6.10 shows the comparison between a regular single Voigt fit and a fit with three equally spaced Voigt profiles of common width with a distance of 1.6 V for a CEC temperature of 180°C. For clarity the residuals are also plotted. The difference in the peak position estimated by a single Voigt fit to the fit with three profiles is 0.1 V, which corresponds to $\approx$1 MHz in frequency.

If the assumptions made above are correct, then the relative peak height of the satellite peaks should depend on the vapor pressure in the cell, being a measure for the collision probability. The peak intensity ratios between the main peak and the leftmost peak were studied at different cell temperatures and the parametrization from Eq. 6.3 was used to estimate the vapor pressures. From Fig. 6.11 we can conclude that there is indeed an increase in the intensity of the satellite peak with increasing potassium vapor pressure in the charge-exchange cell supporting the assumption of collisional excitation.

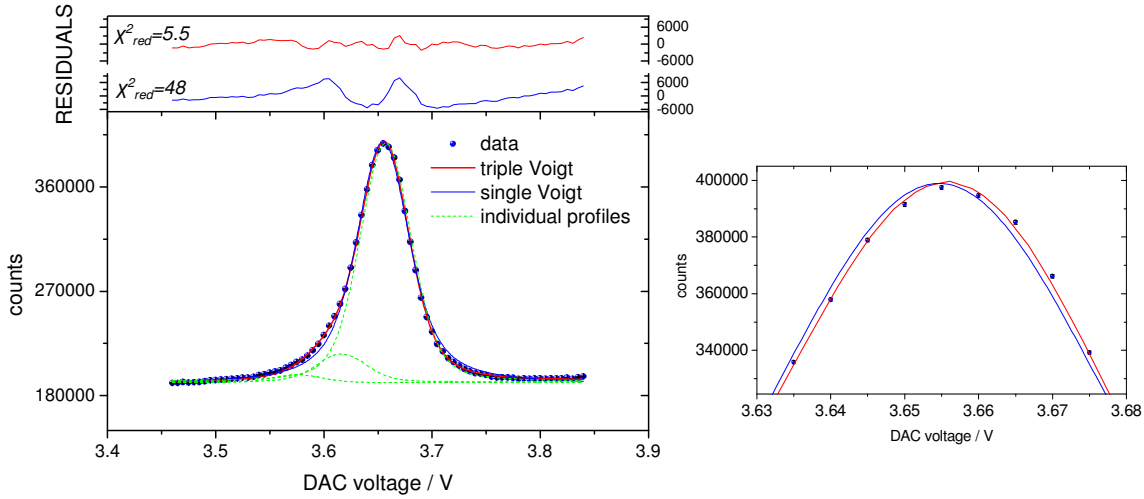

Figure 6.10.: Comparison between a single Voigt fit and multiple Voigt profiles used to fit the ^{85}Rb ($F = 3 \rightarrow F = 4$) resonance recorded at 180°C charge-exchange cell temperature. The improvement of the fit by using three Voigt profiles is indicated by the residuals and the reduced χ^2. In this example the difference in the positions of the main peak is 0.1 V.

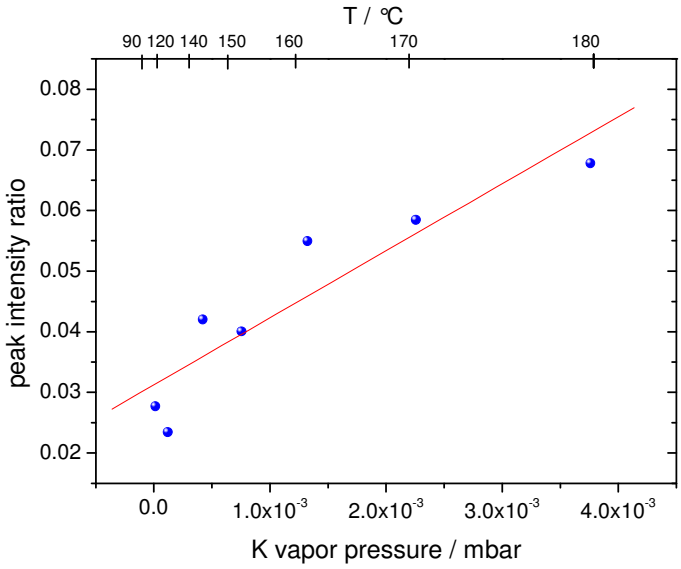

Figure 6.11.: Relative intensity of the leftmost satellite peak in Fig. 6.10 depending on the vapor pressure in the charge-exchange cell. The largest value of the pressure corresponds to an oven temperature of 180°C. The red line is a linear fit to the data. There is a significant increase of the relative peak intensity with increasing vapor pressure.

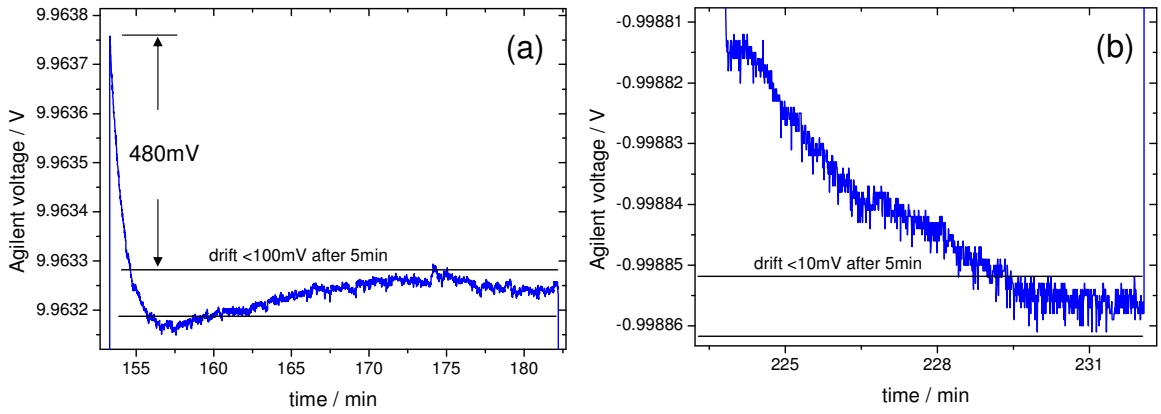

Figure 6.12.: Settling curves of the Heinzinger PNChp10000 output voltage after big voltage jumps. To get the real voltages the shown y-axis has to be scaled with the HV-divider ratio $D = 1001.21$. (a) shows the response of the supply to a jump from 1 kV to 9.976 kV. After 5 min the drift of the voltage is below 100 mV. In (b) the result of a jump from -9 kV to -1 kV is shown. The drift is smaller than 10 mV after 5 min.

6.2.5. Long-Term Stability of the Collinear Setup

The most interesting physics results for laser spectroscopy are expected for the region far off stability. The yields there are rather low, which means long integration times until a resonance can be observed. During this measuring time the applied voltages and the laser frequency need to be as stable as possible. Perfect stability however, can never be achieved. The usual measuring procedure is therefore to do reference scans on stable isotopes and to evaluate, *e.g*, the isotope shift with respect to this reference. Drifts in voltages or frequency can be detected as a shift in the resonance position of the reference isotope and can be corrected for. However, the behavior of the system between two reference measurements needs to be characterized. Especially if we consider that scanning on a reference isotope means changing the offset voltage of the Heinzinger power supply by a significant amount and jumping back to the original voltage to continue the measurement on rare isotopes.

Voltage Stability

The performance of the two Heinzinger 10 kV and 60 kV power supplies was studied using the Julie Research voltage divider and the Agilent precision multimeter. The voltage scale in the graphs of Fig. 6.12 has therefore to be multiplied by the divider ratio of $D = 1001.212$. The Heinzinger PNChp10000 will be used for the offset potential which is applied on the charge-exchange cell or the optical detection region, respectively.

The observed drifts have to be taken into account if highest measurement accuracies are required. In this case during the first five minutes after a voltage reset, laser spectroscopic measurements might be prohibited. After this time the specified stability of 10^{-5} is reached.

For the ion source power supply of the type Heinzinger PNChp60000 a long-term stability measurement over 27 h was made including the warm-up period. Fig. 6.13 shows the result of the voltage monitoring. During the first 20 h there is a drift of 1.2 V for 9.97 kV applied to the ion source. After that the device is very stable with the voltage fluctuating by about 80 mV in

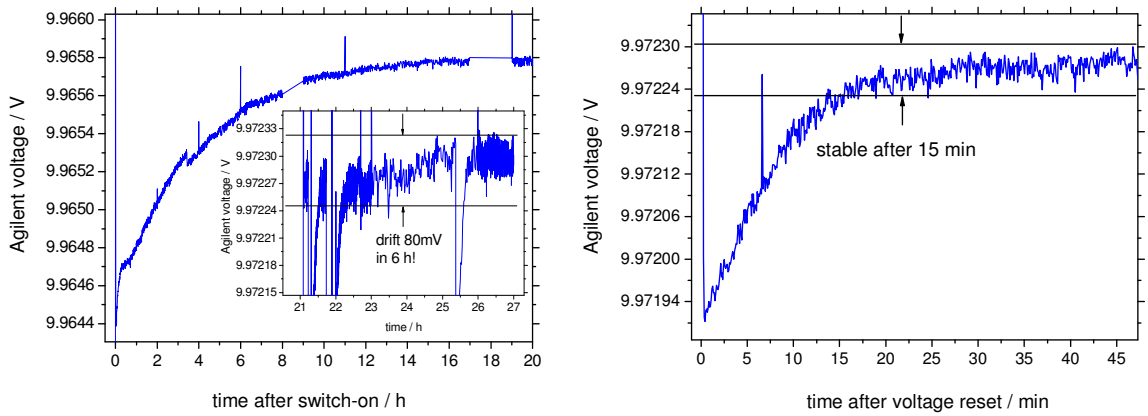

Figure 6.13.: Long-term voltage stability of the Heinzinger PNChp60000 high voltage supply. During the measurement the ion source was connected and the current load was ≈2.8 mA. The left big graph shows the warm-up behavior of the supply needing about 20 h to completely thermalize. The small inset shows the stability after the warm up, which is within the specifications, disregarding the short stand-by pulses. The graph on the right-hand side shows the response of the supply to switching it on again after 10 min stand-by. After 15 min the voltage is stable again.

6 h, which is within the specified stability of 10^{-5} in 8 h. After switching the power supply to stand-by for 10 min, as it can happen in the experiment when the device detects a discharge and turns off, the recovery time is short. After about 15 min the voltage is stable again and the total drift from the voltage right after switching on is only 300 mV in the case of 9.97 kV, which for many cases is tolerable.

Overall Stability

The stability of the combined voltage and laser system was studied by analyzing the evolution of the resonance positions with time. Simultaneous monitoring of the source voltage, supplied for this test by the 10 kV Heinzinger device, allows to extract the long-term behavior and contribution of the laser frequency stabilization. The measurement was performed during five hours in the day time with normal working activity in the reactor hall. In Fig. 6.14(a) the fitted resonance peak positions for the $F = 3 \rightarrow F = 4$ component in ^{85}Rb (points) are shown as a function of time together with the source voltage (solid line). Please note that this measurement includes also all simulated jumps and stand-by phases, therefore the irregular structure in the voltage. As expected from the modified Doppler formula

$$U_{\text{peak}} \approx U_{\text{source}} - \frac{mc^2}{2e}\left(\frac{\nu_{\text{res}}}{\nu_{\text{laser}}} - 1\right)^2, \tag{6.17}$$

the peak center voltage follows the trend of the source voltage. However, there is another contribution to the total drift in the line position resulting in 1 V additional drift in 5 h observation time, which must be attributed to a drift of the laser lock. This drift can be estimated by the approximation

$$\Delta\nu_{\text{laser}} \approx -\frac{\nu_{\text{res}} e}{\sqrt{2eUmc^2}}\Delta U \tag{6.18}$$

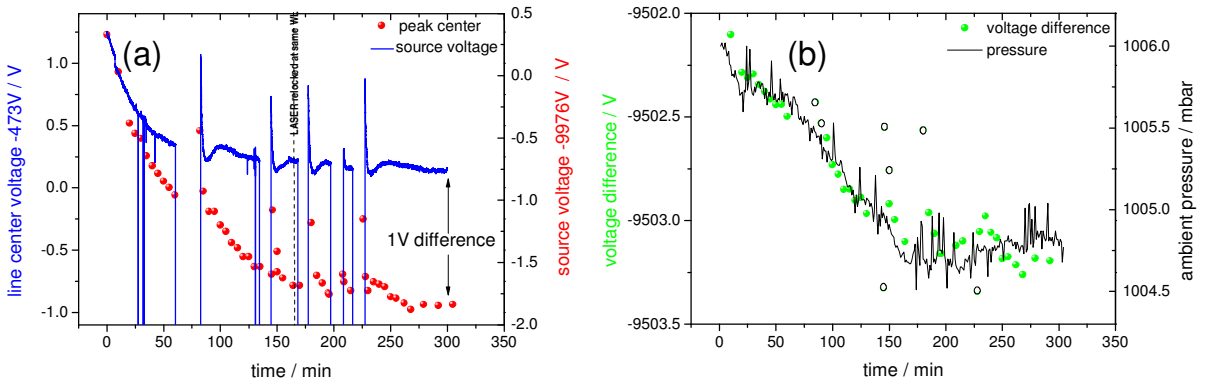

Figure 6.14.: (a) Evolution of the peak position voltage and the source voltage with time. Naturally, the peak position follows the trend of the source voltage, but there is an increasing discrepancy between both voltages culminating in 1 V difference after 5 h. This additional contribution to the line position was found to be due to a drift of the laser lock point caused by a pressure change in the experimental hall as indicated in (b). Here, the difference in the voltages, representing the residual drift of the two curves in (a), is plotted together with the ambient pressure with time. The gray dots are data points belonging to the artificial voltage breakdown and recovery phases. Both curves show the same trend with an inflection point after 160 min.

to 9.7 MHz in 5 h. It was already known that the wavemeter of the Fizeau design is quite sensitive to changes in ambient pressure. This was observed by monitoring the error signal for the frequency lock. The reactor experimental hall is maintained at underpressure compared to the environment in order to prevent possible contaminations in the air from leaving the area. Every time the door is opened, pressure fluctuations in the reactor hall occur which are correlated with a reaction in the laser stabilization error signal. If one compares the trend of the ambient pressure during the day time with the residual drift in the voltage, which was calculated by taking the difference between the two curves in Fig. 6.14(a), a strong correlation is found. Both curves presented in Fig. 6.14, show the same trend and have an inflection point after about 160 min. This leads to the conclusion that the current wavemeter-based laser stabilization is the main contribution to instabilities in the resonance peak position. The drift is caused by a change in the distance between the mirrors in the interferometer which are deformed by the pressure change. This change modifies the wavelength measured and in the stabilization mode the wavemeter generates a regulation signal that tries to compensate for this apparent wavelength change. From the result shown in Fig. 6.14 and the Doppler conversion factor of ≈10 MHz/V, a pressure dependence of about 10 MHz/mbar can be extracted.

So far, all the shown voltage measurements were limited to 10 kV maximum voltage and 10^{-4} measuring accuracy. For the later application of the 60 kV Heinzinger supply in the high-voltage platform of the cooler and buncher, another voltage divider will be required to monitor the stability of the voltage. If it was possible to use a divider of the Münster type [Thu09], then high-voltage measurements with accuracies of the order of 10^{-6} would be possible. However, in this regime contact potentials on electrode surfaces in the cooler and space charge effects will limit the agreement between the measured voltage with the divider and the actual ion energy

after extraction. A 10^{-5} measurement would therefore be sufficient for the purpose of most experiments at TRIGA-LASER which might be obtained using a 60 kV Julie Research divider with an additional temperature stabilization.

With regard to the laser stabilization, there would be the possibility to install the frequency reference, like a wavemeter, an FPI, or even the frequency comb in the temperature- and pressure-stabilized laser laboratory of the institute and to couple the laser light through a fiber reaching from the laser laboratory to the experiment in the reactor hall. A short-term solution which could improve the wavelength stability is a hermetically sealed housing for the wavemeter kept at constant pressure and temperature.

6.3. Summary and Outlook

The current TRIGA-LASER setup is already at a stage to allow the measurement of nuclear spins and moments of radioactive isotopes by studying the hyperfine structure. It was shown in the commissioning measurements that high-resolution scans of atomic hyperfine structures are possible and that the results agree with literature values. The voltages applied are satisfactorily stable with the power supplies working according to their specifications.

The upgrade of the post-acceleration/-deceleration voltage devices, which includes a high-voltage cage to float the offset voltage supply and the charge-exchange cell voltage supply on the scanning voltage, will be the next step towards the full functionality of the setup, involving also isotope-shift measurements with the jump-scan method.

After successful tests of the ion source, the mass separator, and the RFQ cooler and buncher, measurements of charge radii of the neutron-rich isotopes of elements starting from molybdenum and above will be performed to study the shape change at N=60 with a prolate deformation, which is supposed to vanish for nuclei above Mo [Cha09].

Besides the potential to perform laser spectroscopy on unknown ground, the TRIGA-LASER experiment gives a unique opportunity to perform important development work towards higher sensitivity of detectors [Ham10] or higher accuracy of the voltage measurement for the existing COLLAPS experiment at ISOLDE (CERN), but especially it serves as the prototype of the LASPEC beamline for laser spectroscopy on atomic beams at the future facility FAIR at GSI [Rod10].

Part II.

Moments and Radii of Exotic Magnesium Isotopes studied with Collinear Laser Spectroscopy at ISOLDE

7. Collinear Laser Spectroscopy of Mg Isotopes at ISOLDE

The measurements described in the following chapters were performed at the ISOLDE facility at CERN. An overview of the ISOLDE experimental hall with the individual experiments is shown in Fig. 7.1. The general production mechanism and further details about the ISOLDE facility were already discussed in Ch. 3.1.1.

7.1. Isotope Production

For the production of neutron deficient Mg isotopes a silicon carbide target was exposed to the 1.4 GeV proton beam from the proton synchrotron, whereas a uranium carbide target was used for the neutron-rich isotopes. Element-selective ionization was achieved by resonant laser ionization [Koe03] and the magnesium ions were extracted from the source and accelerated to a beam energy of 60 keV. The production yields are listed in Tab. 7.1 for all radioactive magnesium isotopes. In the case of ^{21}Mg an enormous contamination of $> 10^8$ ions/s of ^{21}Na was observed despite of the element-selective ionization, due to the large production yield of ^{21}Na, its low ionization potential and the required high temperature at the source. This contamination could be reduced by 2 orders of magnitude by carefully tuning the slits behind the high-resolution mass separator (HRS). Also the strong contamination of ^{24}Na in the ^{24}Mg stable isotope beam should be mentioned because it prohibited the use of ^{24}Mg as a reference isotope in isotope shift measurements to avoid contamination of the detection region and the β-NMR setup with this rather long-lived isotope ($T_{1/2}$=15 h).

7.2. The COLLAPS Setup

The collinear laser spectroscopy setup COLLAPS (*Col*linear *Ap*plied *S*pectroscopy) is one of the pioneering experiments in on-line laser spectroscopy. A precursor experiment was started at the TRIGA research reactor in Mainz for the study of neutron-rich Rb and Cs isotopes extracted from a surface ion source placed in one of the beam tubes of the reactor [Kle79, Rei80]. From 1978 to 1979 COLLAPS was installed at ISOLDE (CERN) and until today it delivers valuable input to the understanding of nuclear structure in the region of unstable nuclei [Noe10]. Very recently, the achievable accuracy of the experiment was pushed to its limits to extract the very small field shifts of the neutron-rich Be isotopes by combining collinear and anti-collinear excitation with the accurate frequency determination with a frequency comb [Noe09]. The location of the experiment in the ISOLDE hall is indicated in Fig. 7.1 and a schematic view of the experimental setup of the COLLAPS experiment is shown in Fig. 7.2. Details will be discussed in the following sections. In this work, all detection methods discussed in 3.2.1 have been applied to adapt the experiment to the properties and the yields of the species of interest. The measurements described in the next two chapters will give an impression about the versatility of the experimental method.

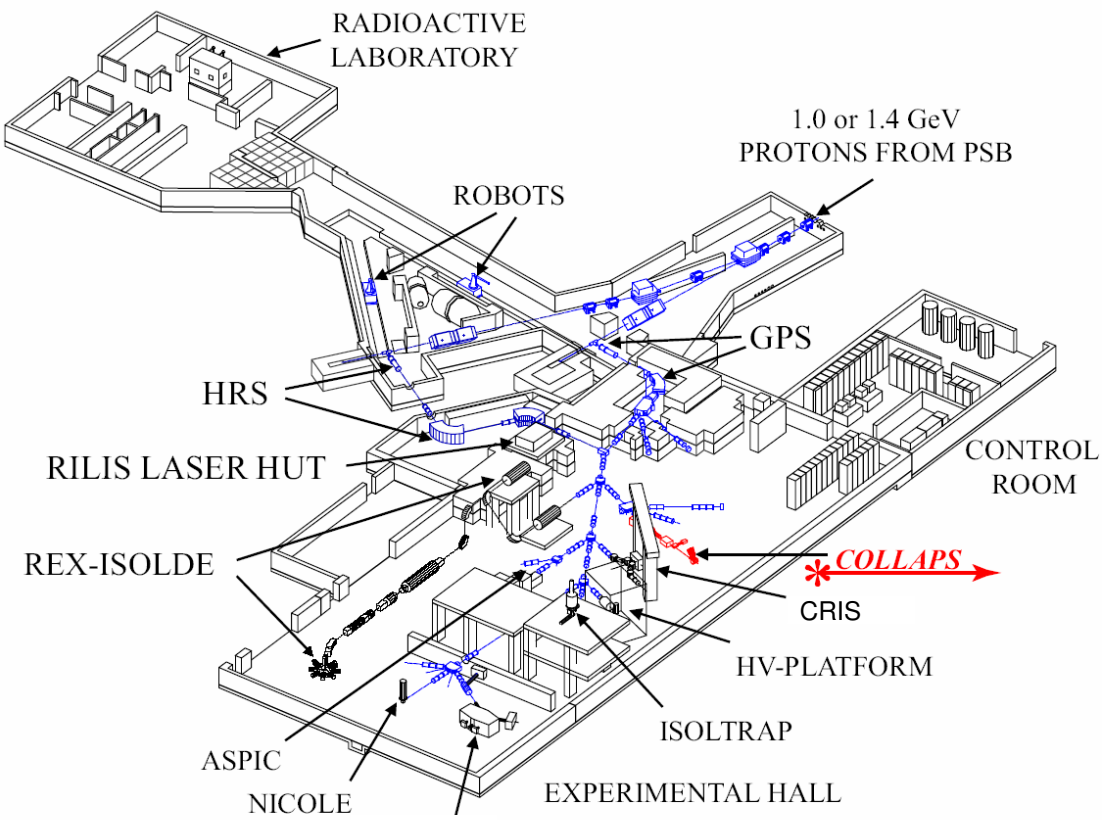

Figure 7.1.: The ISOLDE experimental hall with the transport beamline and the individual experiments.

Table 7.1.: Average production yield of radioactive magnesium isotopes at ISOLDE. The yields for the neutron-deficient isotopes $^{21-23}$Mg are obtained with a silicon carbide (SiC) target and the neutron-rich isotopes are produced with a uranium carbide target. Laser resonance ionization was used to ionize the species. 1 ion/μC corresponds to approximately 1 ion/s, depending on the current and the pulse structure of the protons.

Isotope	yield / ions/μC	Isotope	yield / ions/μC
^{21}Mg	$< 1 \times 10^4$	^{28}Mg	3.6×10^7
^{22}Mg	9×10^5	^{29}Mg	1.2×10^6
^{23}Mg	1.4×10^7	^{30}Mg	4.6×10^5
^{24}Mg	stable	^{31}Mg	1.5×10^5
^{25}Mg	”	^{32}Mg	4.2×10^4
^{26}Mg	”	^{33}Mg	5.3×10^3
^{27}Mg	1.4×10^6		

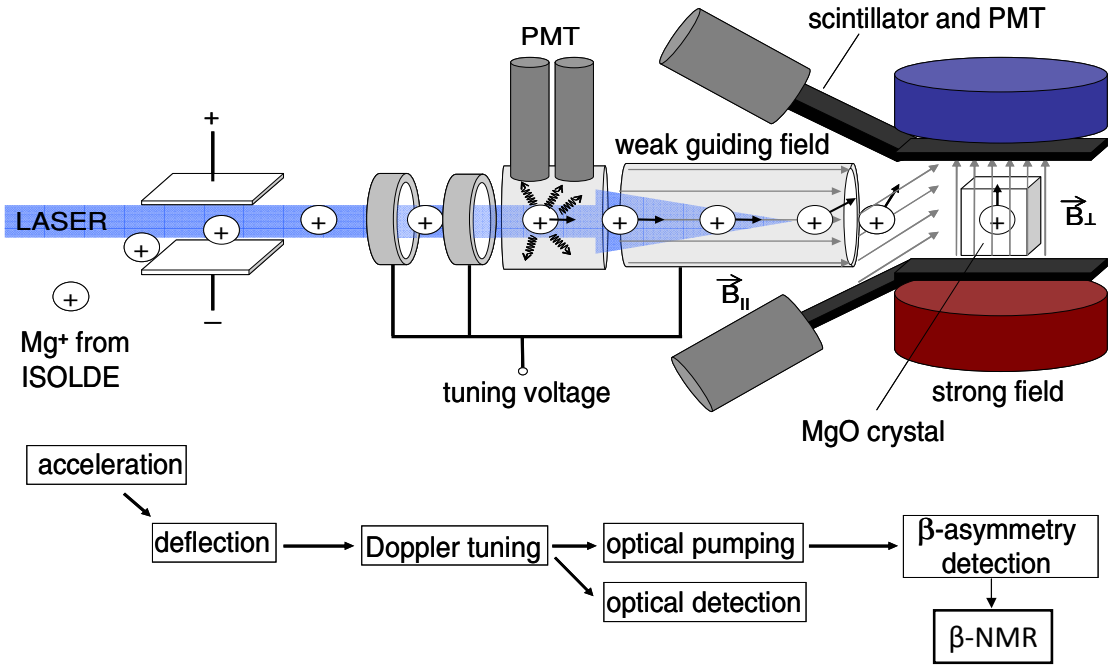

Figure 7.2.: Top view of the experimental setup used for optical pumping followed by β-NMR. The ions from ISOLDE are exposed to circularly polarized laser light in a weak magnetic guiding field. The resulting atomic polarization is adiabatically rotated in the transition region between the weak longitudinal guiding field and the strong perpendicular NMR field. In the strong field the nuclear moment is decoupled from the electron shell before the ion is implanted into a MgO crystal. Two opposing pairs of scintillators (left and right) are used to detect the asymmetry of the β decay. A radio frequency signal can be applied to a coil around the crystal (not shown in this figure) to resonantly destroy the nuclear polarization and thus the β asymmetry.

7.2.1. Laser System and Doppler Tuning

For all measurements with Mg ions the laser light was produced with a Coherent 699-21 ring dye laser, which was locked to a temperature stabilized Fabry-Perot interferometer, and subsequent second-harmonic generation with a WaveTrain frequency doubler. The laser frequency was monitored with a Burleigh wavemeter with 300 MHz accuracy.

To scan the resonances, Doppler tuning was performed with a voltage scan by a Kepco voltage amplifier with a gain of ≈ 50 fed by the output voltage from an 18 Bit CAMAC DAC. In the case of magnesium the differential Doppler shift corresponds to approximately 20 MHz/V. An additional offset voltage was added to account for the isotope shifts between the isotopes and the resulting voltage shift. This voltage was produced by a Fluke 410B high voltage supply and measured with a Julie Research KV-10R voltage divider and a PREMA high-precision multimeter. The formulas needed to connect the total acceleration voltage to the laser frequency in the ion rest frame are given in App. A. For each data point a dwell time of typically 10 ms was used for the integration of the photomultiplier counts, before switching to the next voltage with a step size of typically 500 mV.

In order to make the isotope-shift measurements more accurate, a calibration of the ISOLDE ion-source voltage supply and the Julie Research 10 kV voltage divider was performed with a high-precision high-voltage divider [Thu09, Kri10]. It was discovered that the real source voltage is about 36.5 V lower than the value recorded by the data acquisition program. All voltages were therefore corrected in the data analysis. Contrary, the divider ratio for the measurement of the post-acceleration voltage was determined to be 1000.02 which is well within the specifications given by the manufacturer of 1000.0(1).

7.2.2. Setup for β-NMR of ^{21}Mg

In the case of the neutron-deficient ^{21}Mg, optical pumping was performed on the $3\,^2S_{1/2} \rightarrow 3\,^2P_{3/2}$ D2 transition of the Mg ion at a wavelength of 279.635 nm [Kau91] with circularly polarized laser light in a weak magnetic guiding field. At the transition to the strong field of the NMR magnet the atomic polarization is first rotated by 90° as indicated in Fig. 7.2 and then the nuclear polarization is decoupled from the atomic shell in the strong magnetic field of the NMR magnet, before the ion is implanted into a MgO crystal. The signals of the particle counters obtained from the β decay particles were recorded as a function of the Doppler-tuning voltage applied to the optical pumping drift section. For the NMR measurement an RF field was applied to the coil around the MgO crystal. For further background reduction 3 mm copper degraders were placed between the vacuum chamber and the detectors to stop most of the lower-energy positrons from the decay of the ^{21}Na isobaric contamination in the ion beam. An additional reduction of the background by 3 orders of magnitude was achieved.

7.2.3. Setups for Isotope Shift Measurements

For the measurement of the isotope shifts of the neutron-rich Mg isotopes several different measurement techniques had to be combined to extract the resonance positions for the different isotopes. For all isotope shift measurements the $3s\,^2S_{1/2} \rightarrow 3p\,^2P_{1/2}$ D1 transition at 280.271 nm [Kau91] was used and the isotope shifts were measured with respect to the reference isotope ^{26}Mg. Nuclides with relatively high production yields, such as $^{24-30}$Mg, were measured with classical optical fluorescence detection. Doppler tuning was performed as described above. The rarely produced exotic isotope ^{31}Mg was studied with β-decay asymmetry detection after optical pumping. This technique was for the first time employed for isotope-shift measurements. Since

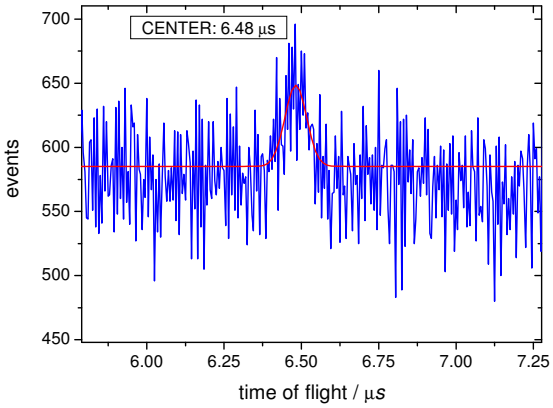

Figure 7.3.: Time-of-flight spectrum of ^{32}Mg triggered on the fluorescence signal from the photomultiplier. The center position is 6.48 μs and the full width a the base is 170 ns.

it relies on the understanding and modeling of the line profile in β-asymmetry detection to extract the resonance positions it was crucial to have a candidate where both techniques can be applied and compared. Therefore, ^{29}Mg was remeasured with β detection. Additionally, photon-ion coincidence detection (see Ch. 3.2.1) was used to increase the signal-to-noise ratio for the measurement on ^{32}Mg. The coincidence measurement on ^{32}Mg required the determination of the correct delay and further electronics to make the photomultiplier signals coincident with the particle counter signals. In Fig. 7.3 the time-of-flight spectrum of ^{32}Mg is shown which was used to set the correct time delay produced by a DGG222 delay generator and the gate width for the photon signals, set by a CAEN N93B dual timer, to coincide with the events from the particle counter. The center position of the coincidence peak is 6.48 μs. The width at the base is about 170 ns. A conservative time gate of 400 ns was chosen to be sure not to miss any real coincidence events.

8. Magnetic Moment of the Neutron-Deficient Isotope ^{21}Mg Determined with β-NMR

Nuclei far from β-stability can be used as a benchmark for the nuclear shell model which is well adapted to predict the observables of nuclei in the valley of stability. The validity in the exotic region needs to be further investigated. ^{21}Mg is one of the few accessible $T_z = 3/2$ cases in the *sd* shell [Fir04]. The fact that the magnetic moment of the mirror nucleus ^{21}F is also known allows to study the mirror symmetry in the *sd* shell.

8.1. Experimental Results

To detect the spatial asymmetry in the emission of the β-decay positrons (see Ch. 3.2.1) the signals of the scintillators (left and right) were recorded. The asymmetry can be quantified as

$$a = \frac{N_{\text{left}} - N_{\text{right}}}{N_{\text{left}} + N_{\text{right}}}\,, \tag{8.1}$$

with the count rates N of the photomultipliers attached to the scintillators. The hyperfine structure in the optical transition was obtained by recording the asymmetry a as a function of the Doppler-tuning voltage applied to the optical pumping line. The result for both σ polarizations is shown in Fig. 8.1 together with the atomic level scheme. The fit to the data was performed by numerically solving the rate equations of the optical pumping process and calculating the resulting asymmetry from the assumed hyperfine structure pattern [Kei00]. Free parameters were the asymmetry offset and a slope of the baseline and the hyperfine structure parameters A for the ground-state and the excited-state splitting. The spin was originally fixed to $I = 5/2$ according to the shell model predictions. Not taken into account was a possible elliptical polarization of the laser light affecting the polarization, which might be the reason for the small deviations between the experimental resonances and the fitted profiles.

At first, the extracted resonance positions were only used to find the optimal position for the β-NMR measurement. Staying on a constant voltage at the position of the strongest peak, *i.e.* the first peak of the right hyperfine multiplet for σ^- light, the rf signal was applied, leading to a resonant destruction of the asymmetry and hence, to a smaller asymmetry signal. The resulting resonance after a total integration time of 12 h is shown in Fig. 8.2 (a). The data is the sum of two individual measurements. The fitted function is not a Lorentzian because this would only be observed for a monochromatic radio-frequency excitation. Here, however, a sinusoidal frequency modulation of 5 kHz amplitude was applied to artificially broaden the profile. Hence, a larger step size could be used when tuning the rf frequency to allow for shorter measurement times. Substituting the sinusoidal frequency modulation $\nu(t) = \nu + M\sin(\omega t)$ into the Lorentzian profile and integrating over a modulation period modifies the profile to [Yor07b]

$$f(\nu, \nu_0, \Gamma, M) \propto \int_{-1}^{1} \left\{ 1 + \left[\frac{2\left(M\tau + \nu - \nu_0\right)}{\Gamma} \right]^2 \right\}^{-1} \frac{d\tau}{\sqrt{1-\tau^2}}\,, \tag{8.2}$$

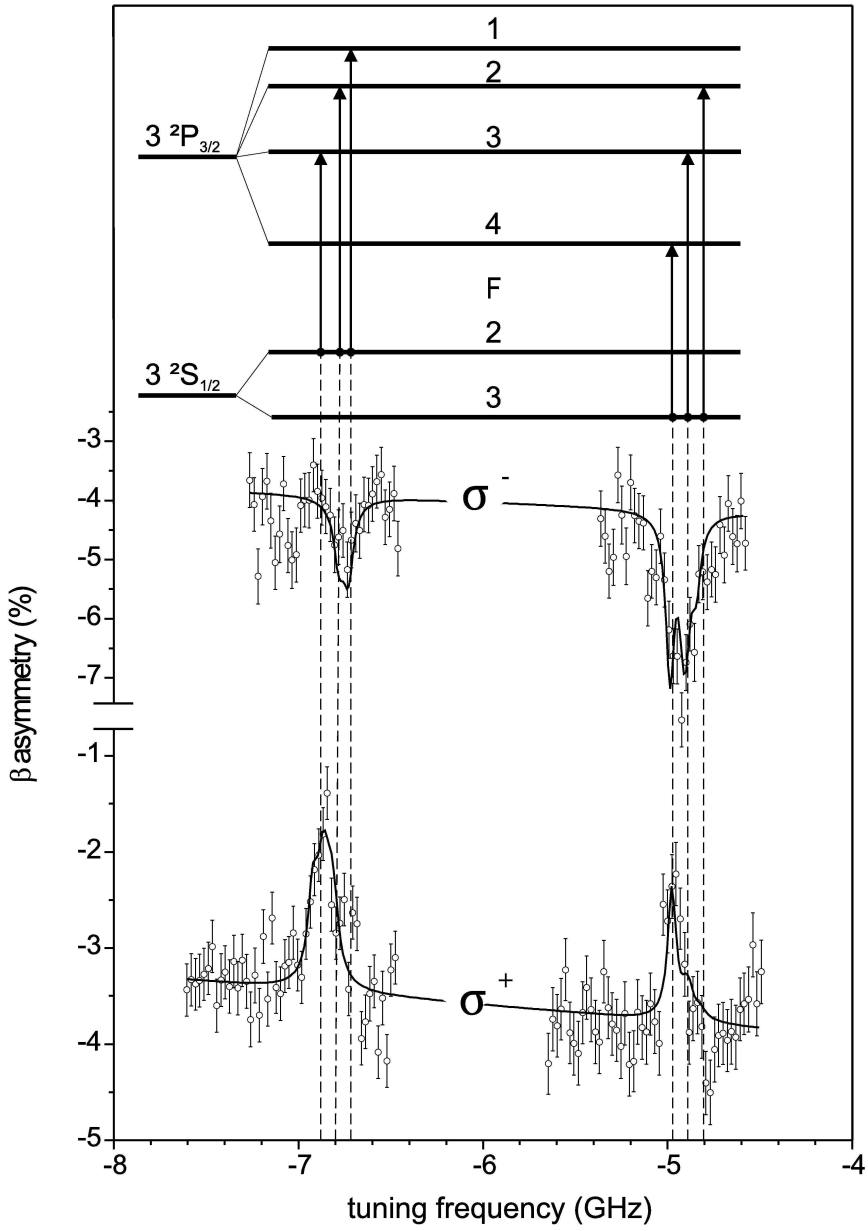

Figure 8.1.: Hyperfine structure of ^{21}Mg for σ^+ and σ^- polarization and the corresponding energy level diagram for a negative magnetic moment and a nuclear spin $I = 5/2$. The frequency scale was calculated with respect to the ^{24}Mg transition frequency from the total acceleration voltage and the laser frequency as measured with a wavemeter. The solid lines represent fits of simulated spectra as discussed in the text. For more details refer to the text.

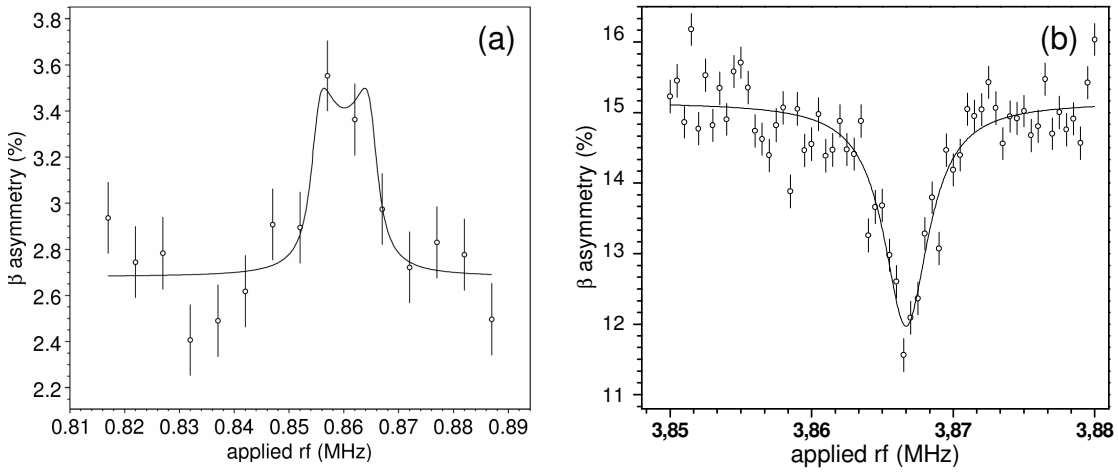

Figure 8.2.: Nuclear magnetic resonances of ^{21}Mg with frequency modulation (a) and of the reference isotope ^{31}Mg without frequency modulation (b). The determined resonance frequency for ^{21}Mg extracted from the fit with the fitting function (Eq. 8.2) is $\nu\left(^{21}\mathrm{Mg}\right) = 860.1(12)\,\mathrm{kHz}$. The resonance profile of ^{21}Mg shows an increase in the measured asymmetry, which can be explained by different count rates of the individual particle detectors resulting in an offset value for the asymmetry even without optical pumping. This offset has changed from the hyperfine structure measurement to the NMR measurement due to a modification of the discriminator levels of the counting electronics.

with the central frequency ν_0, the Lorentz width of the profile Γ, and the modulation amplitude M. A resonance frequency of $\nu\left(^{21}\mathrm{Mg}\right) = 860.1(12)\,\mathrm{kHz}$ is obtained from a χ^2 minimization of this profile to the experimental data points. The statistical uncertainty is deduced from the fit.

The resonance frequency, *i.e.* the Larmor frequency ν_L, can be written as

$$\nu_L = \frac{gB\mu_N}{h} \tag{8.3}$$

with the nuclear magneton μ_N, Planck's constant h, and the magnetic flux density B. This allows to determine the nuclear g factor if the precise magnetic field at the location of the crystal and the implanted ions is known. Therefore, a reference measurement with ^{31}Mg with the known g factor $g\left(^{31}\mathrm{Mg}\right) = -1.7671(3)$ [Ney05] was used to calibrate the magnetic field. The corresponding resonance is shown in Fig. 8.2 (b) together with a Lorentzian fit, since no frequency modulation was applied. A central frequency of $\nu\left(^{31}\mathrm{Mg}\right) = 3866.67(14)\,\mathrm{kHz}$ was obtained, which lead to an absolute value of the ^{21}Mg nuclear g factor

$$\left|g\left(^{21}\mathrm{Mg}\right)\right| = \frac{\nu\left(^{21}\mathrm{Mg}\right)}{\nu\left(^{31}\mathrm{Mg}\right)}\left|g\left(^{31}\mathrm{Mg}\right)\right| = 0.393(3)\,. \tag{8.4}$$

The uncertainty is the quadratic sum of the statistical uncertainty from the fit and a 0.6% relative systematic uncertainty 5 kHz/860 kHz due to the frequency modulation of 5 kHz. The sign of the g factor can not be extracted from this measurement.

The g factor amplitude can now be used to analyze the hyperfine structure in more detail as

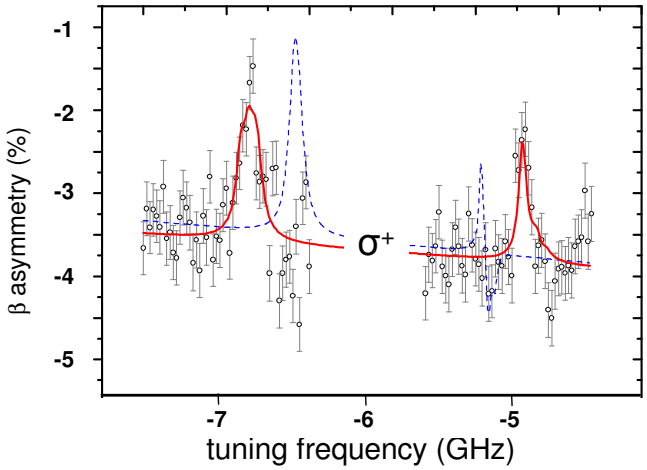

Figure 8.3.: Comparison of the fitting result obtained with spin $I = 5/2$ shown as a solid red curve and a simulation for spin $I = 3/2$, shown as the blue dashed line, with the A factor fixed to the value deduced from the g factor as described in the text.

it is now possible to calculate the hyperfine A factor

$$A = \frac{g_I \mu_N B}{J} \tag{8.5}$$

and to use it as a fixed parameter in the fitting procedure. As the total separation of the individual multiplets is determined by the A factor (see Ch. 2.1.1) and the nuclear spin I according to Eq. 2.12, the spin I can be extracted in this way. Therefore, another Mg reference isotope has to be used to eliminate the unknown magnetic field of the moving electrons at the nuclear site. Using the stable reference isotope ^{25}Mg with spin $I = 5/2$, a magnetic moment of $\mu\left(^{25}\mathrm{Mg}\right) = -0.85545(8)\mu_N$ [Rag89], and $A\left(^{25}\mathrm{Mg}\right) = 596.254376(54)\,\mathrm{MHz}$ [Ita81] the A factor is

$$\left|A\left(^{21}\mathrm{Mg}\right)\right| = \left|\left(g\left(^{21}\mathrm{Mg}\right) A\left(^{25}\mathrm{Mg}\right) 5/2\right) / \mu\left(^{25}\mathrm{Mg}\right)\right| = 684(4)\,\mathrm{MHz}\,. \tag{8.6}$$

A reasonable fit to the data shown in Fig. 8.3 with this A factor as a fixed parameter is only possible with spin $I = 5/2$. Other values result in either a too large hyperfine splitting or the splitting is too small and the peak positions predicted by the fitting function do not match the real positions at all, as it is demonstrated for $I = 3/2$ as an example in Fig. 8.3.

The sign of the g factor can now be fixed by studying its impact on the hyperfine structure center of gravity. For this, the isotope shift between ^{21}Mg and ^{24}Mg is estimated based on the mass shift constant $K_{MS} = -954(12)\,\mathrm{GHz\,u}$ obtained from theoretical calculations [Ber03] to $\delta\nu^{21,24} = K_{MS} \times \frac{m_A m_{A'}}{m_A - m_{A'}} = 5.65(7)\,\mathrm{GHz}$, neglecting the small field-shift contribution. Assuming a positive g factor the experimental isotope shift calculated from the center of gravity of ^{21}Mg and the resonance position of ^{24}Mg is 5.95 GHz whereas it is 5.63 GHz for the negative sign. It can therefore be concluded that the sign of the g factor and, hence, the magnetic moment, is negative. Finally, the nuclear magnetic moment can be calculated from the g factor and the nuclear spin I to

$$\mu\left(^{21}\mathrm{Mg}\right) = g\left(^{21}\mathrm{Mg}\right) \times I \times \mu_N = -0.983(7)\,\mu_N\,. \tag{8.7}$$

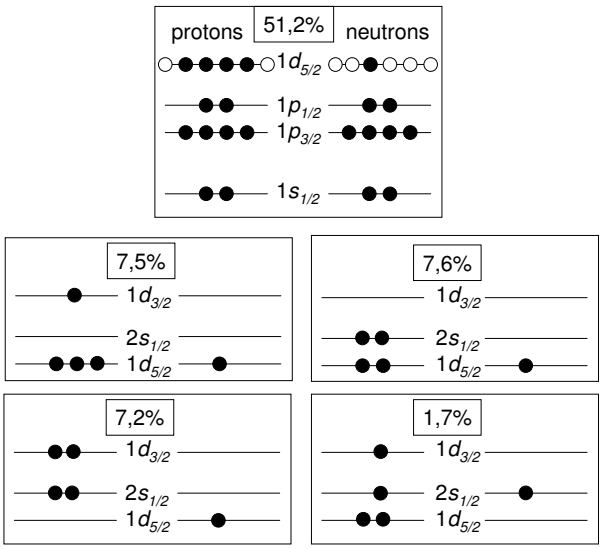

Figure 8.4.: Ground state composition of ^{21}Mg according to ANTOINE [Cau06] calculations performed in this work. Only the most dominant contributions are shown. The standard single-particle shell model state is shown on top. There is significant configuration mixing resulting in a magnetic moment being much smaller in absolute value than the single-particle value. The relative fractions of the individual configurations are indicated.

8.2. Discussion

For $N = 9$ isotones an even Z the nuclear shell model predicts a ground state which is governed by the unpaired neutron in the $1d_{5/2}$ orbit. In the extreme single particle picture, the Schmidt model, the ground-state configuration of ^{21}Mg should consist of closed $1s$ and $1p$ shells for the neutrons and the protons and four protons in the $1d_{5/2}$ proton shell as indicated in the configuration shown on top of Fig. 8.4. This assumption leads to a single-neutron magnetic moment of $-1.913\,\mu_N$ from the unpaired neutron in the $1d_{5/2}$ neutron shell.

To understand the large discrepancy to the measured value, large-scale shell-model calculations using the shell-model code ANTOINE [Cau06] with the USD interaction Hamiltonian proposed by Wildenthal [Wil84] were used to calculate the ground-state configuration and the magnetic moment of ^{21}Mg. According to this calculation the ground state is strongly mixed and composed of different configurations. The main contributions are shown in Fig. 8.4. For this ground state the shell model code predicts a magnetic moment of $-0.968\,\mu_N$, which differs only by 1.5% from the measured value.

Isoscalar Magnetic Moment

The proton-rich nucleus ^{21}Mg is one of the few experimentally accessible nuclei with the isospin $T_Z = (N - Z)/2 = +3/2$. Using the magnetic moment of the $T_Z = -3/2$ mirror nucleus ^{21}F and the results obtained here the spin expectation value $\langle\sigma\rangle$ can be calculated from the isoscalar part of the magnetic moment [Sug69]

$$\mu_{\mathrm{IS}} = \frac{1}{2}\left[\mu\left(T_z = +3/2\right) + \mu\left(T_z = -3/2\right)\right] \tag{8.8}$$

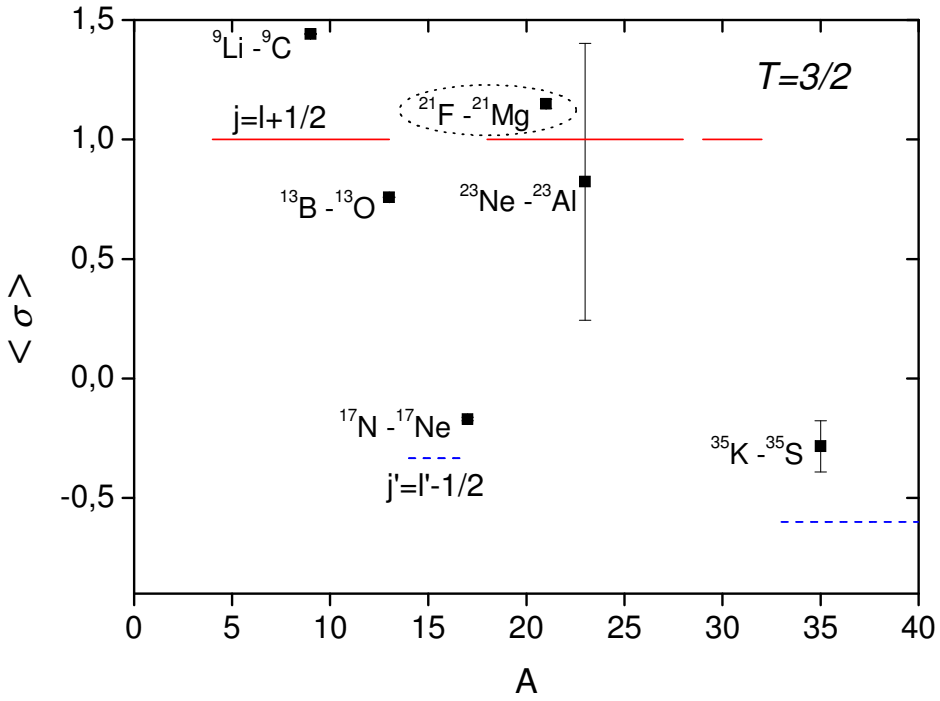

Figure 8.5.: Spin expectation values for the known $T = 3/2$ mirror pairs shown together with the single-particle limits indicated as solid red lines for the $j = l + 1/2$ cases and as dashed blue lines for the $j' = l' - 1/2$ cases. The values were taken from this work and from [Mat99, Mat95, Gei05, Wil71, Bur54, Cor83, Uen96, Mer06, Oza06, Mat96].

using the relation [Sug73]

$$\langle\sigma\rangle = \frac{2\mu_{\mathrm{IS}}/\mu_N - I}{(\mu_p + \mu_n)/\mu_N - 1/2}\,. \tag{8.9}$$

I is the total angular momentum (spin) of the nucleus, $\mu_p = 2.793\,\mu_N$ and $\mu_n = -1.913\,\mu_N$ are the free-nucleon magnetic moments for the proton and the neutron, respectively. For the mirror pair $\left(^{21}\mathrm{F},\ ^{21}\mathrm{Mg}\right)$ we obtain the value $\langle\sigma\rangle = 1.15$.

The extreme single-particle model predicts a value of $\langle\sigma\rangle = 1$ for a nucleon in the single particle state $j = l+1/2$. Empirical values for $T = 1/2$ are consistently smaller than one. In the $T = 3/2$ case only three mirror pairs with a $j = l+1/2$ ground state have been investigated experimentally, so far. In the $\left(^{13}\mathrm{B},\ ^{13}\mathrm{O}\right)$ case the spin expectation value is 0.758(2) [Huh98] which agrees well with the known empirical systematics from $T = 1/2$ nuclei. The $\left(^{9}\mathrm{Li},\ ^{9}\mathrm{C}\right)$ system exhibits a large value of $\langle\sigma\rangle = 1.441(2)$ [Mat95, Huh98]. For the third pair $\left(^{23}\mathrm{Ne}\,,^{23}\,\mathrm{Al}\right)$, the spin expectation value is 0.82(58) [Gei05, Oza06] but the uncertainty on the magnetic moment of ^{23}Al is too large to judge whether $\langle\sigma\rangle$ is larger or smaller than one. The results for all known $T = 3/2$ mirror pairs are summarized in Fig. 8.5. All experimental results for the four $T = 3/2$,$j = l + 1/2$ mirror pairs together with the predictions from the extreme single-particle model and the shell model are summarized in Tab. 8.1.

It was tried to reproduce the occurrence of spin expectation values greater than unity by including isospin non-conserving effects (INC) [Orm89] in the shell-model calculations [Man98], but the resulting $\langle\sigma\rangle$ value for $\left(^{9}\mathrm{Li},\ ^{9}\mathrm{C}\right)$ was still 18% smaller than the experimental value. Finally, it was shown that intruder configurations are the key to reproducing the large value

Table 8.1.: Experimental spin expectation values $\langle\sigma\rangle$ for the four $T = 3/2$, $j = l + 1/2$ mirror pairs and theoretical predictions from the single-particle (s.p.) model, the shell model with isospin non-conserving interactions (INC), with the universal *sd* (USD) interaction [Wil84] for the *sd*-shell or with the *p* shell two-body matrix element (PTBME) interaction [Jul92] for the *p*-shell and with the Warburton Brown *p* shell (WBP) interaction for the *p*-*sd* shell [War92].

Mirror pair	Exp.	s.p.	INC	USD/PTBME	WBP
$(^{21}\mathrm{F},\ ^{21}\mathrm{Mg})$	1.15(2)[a]	1.00	1.15[b]	1.11[a]	-
$(^{9}\mathrm{Li},\ ^{9}\mathrm{C})$	1.44(2)[b]	1.00	1.18[b]	1.09[b]	1,47[c]
$(^{23}\mathrm{Ne},\ ^{23}\mathrm{Al})$	0.82(58)[d]	1.00	-	0.82[a]	-
$(^{13}\mathrm{B},\ ^{13}\mathrm{O})$	0.758(2)[e]	1.00	-	-	-

[a] this work
[b] values taken from [Man98, Huh98]
[c] values taken from [Uts05]
[d] values taken from [Gei05, Oza06]
[e] values taken from [Mat96, Wil71]

[Uts05], meaning that the model space used for the shell-model calculations had to be extended to the *sd* shell [War92].

In the case of the A=21 mirror pair, already the isospin-symmetric shell model reproduces the experimental magnetic moments rather well with $-0.968\,\mu_N$ for ^{21}Mg and $+3.888\,\mu_N$ for ^{21}F. This results in $\langle\sigma\rangle = 1.11$. The value changes slightly to 1.15, in excellent agreement with the experimental value, if the Coulomb interaction for the protons and asymmetric nucleon-nucleon interactions are taken into account [Man98].

9. Charge Radii of $^{24-32}$Mg from Combined Optical and β-Asymmetry Detection

In the measurements described in this chapter the classical optical detection was combined for the first time with the detection of the β asymmetry to determine isotope shifts for the extraction of nuclear radii. This was only possible by carefully studying and simulating the spectra observed in the β detection [Kei00] and taking systematic line shifts due to the applied magnetic guiding field into account. To check for the consistency of this method the isotope shift between ^{26}Mg and ^{29}Mg was measured with combined fluorescence and asymmetry detection and with fluorescence detection only.

9.1. Optical measurements

Typical spectra of ^{24}Mg and ^{26}Mg as examples for the even-even isotopes are shown in Fig. 9.1. The single resonances of these isotopes were fitted with Voigt profiles with the Lorentz width fixed to the natural linewidth of 41.4 MHz and the Doppler width as a free parameter that was typically 24 MHz. A small satellite peak on the left side caused by ions that have undergone a collisional excitation with the residual gas and were therefore slower by ≈ 4.5 eV was also included in the fitting routine by a second Voigt profile. This energy loss corresponds to the energy gap of the $3\,^2S \rightarrow 3\,^2P$ transition. Such side peaks are also visible in the odd-isotope cases with hyperfine structure and are accounted for by the fitting routine. Together with the resonance center voltage, the total acceleration voltage was calculated from the source voltage and the detection region offset voltage:

$$U_{\text{total}} = U_{\text{source}} - \left(U_{\text{offset}} + f_{\text{Kepco}} \times U_{\text{DAC}}\right) . \tag{9.1}$$

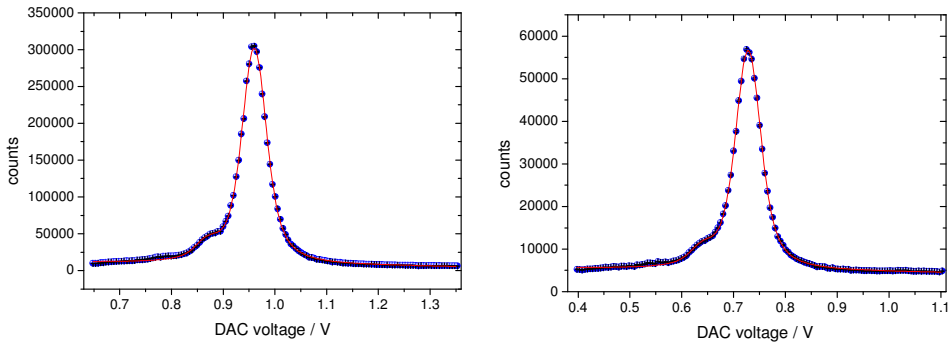

Figure 9.1.: Fluorescence signal of ^{24}Mg (left) and ^{26}Mg (right). The resonances are the sum of 20 individual scans. The side peak from collisional excitation is well pronounced and included in the fitting routine (see text).

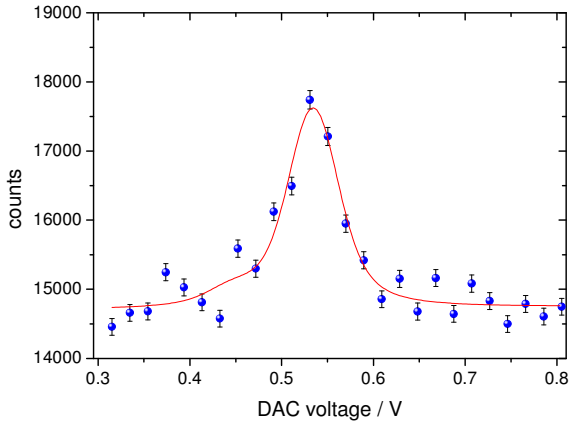

Figure 9.2.: Photon-ion coincidence signal of ^{32}Mg. The background was reduced by a factor of six compared to the classical fluorescence detection.

For the isotope-shift calculations these individual measurements were always referenced with a subsequent reference measurement on ^{26}Mg to cancel long-term systematic drifts of voltages or the laser wavelength. The isotope shifts were calculated according to the expression given in App. A.2 in the fully relativistic form.

While the measurements for the less exotic spin I=0 isotopes took only a few hours each, the coincidence scans on ^{32}Mg were performed during 26 hours until seven reasonable spectra were recorded. Fig. 9.2 shows a typical signal of the coincidence measurement. The background was compressed by a factor of six compared to the classical optical detection with scattered-light background rates of typically 5000 s^{-1}.

The results of the isotope-shift measurements are summarized in Tab. 9.1 together with the statistical uncertainties from the fits and the systematic uncertainties due to the uncertainties of the applied voltages.

Independent from our measurement, the isotope shift between ^{24}Mg and ^{26}Mg was recently remeasured on laser-cooled and trapped Mg ions in an rf trap [Bat09], offering the opportunity to check the accuracy of our experimental method. Our result is in reasonable agreement with the trap measurement within our uncertainty showing that the calibration was successful and justifying our estimated systematic uncertainties.

For the resonances of the $I \neq 0$ isotopes the full hyperfine structure was fitted with a routine that calculates the center of gravity of the resonances with the Spin I and the hyperfine A factor taken from [Yor07b, Kow06] as fixed parameters. Lorentz profiles were fitted to the data with peak intensities, linewidth, offset and center of gravity as free parameters. In Fig. 9.3 typical spectra for the isotopes ^{25,27,29}Mg are shown. The solid red lines indicate the fit to the data.

9.2. Optical Pumping and Asymmetry Detection

The measurement of the hyperfine structure of ^{31}Mg was performed by optical pumping and the detection of the asymmetry in the emission of the β-decay positrons induced by the polarization of the nucleus as discussed in Ch. 8. As a reference for the reliability of the extracted center of gravity of the resonances and hence, the possibility to connect the data taken by both methods, the measurement on ^{29}Mg was repeated with optical pumping as well. It is important to notice that the isotope shifts between ^{26}Mg and ^{29}Mg obtained with optical detection and asymmetry

Table 9.1.: Isotope shifts of the neutron-rich magnesium isotopes $^{24-32}$Mg. The first value in brackets corresponds to the statistical uncertainties. The second value is the systematic voltage uncertainty.

isotope shifts	technique	our experiment/MHz	literature [Bat09]/MHz
$\delta\nu^{26,24}$	opt.	3076 (2)(7)	3084.905 (93)
$\delta\nu^{26,25}$	”	1460 (3)(3)	
$\delta\nu^{26,27}$	”	-1361 (1)(3)	
$\delta\nu^{26,28}$	”	-2598 (1)(5)	
$\delta\nu^{26,29}$	”	-3768 (1)(9)	
$\delta\nu^{26,29}$	asym.	-3767 (2)(9)	
$\delta\nu^{26,30}$	opt.	-4834 (3)(12)	
$\delta\nu^{26,31}$	asym.	-5835 (2)(14)	
$\delta\nu^{26,32}$	opt.	-6780 (2)(15)	

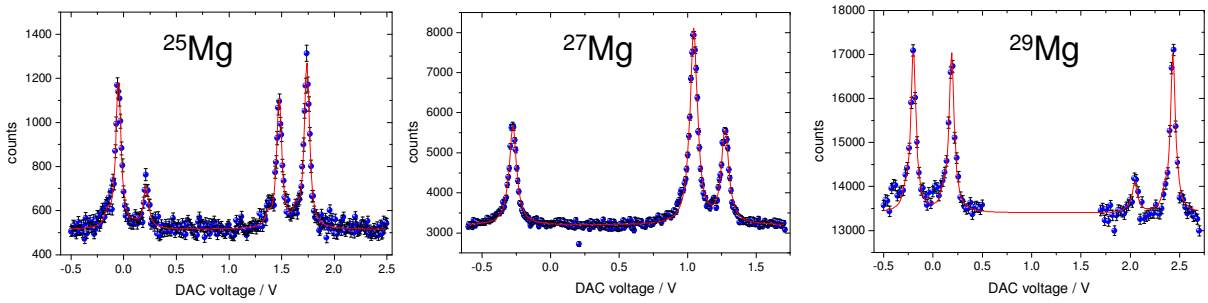

Figure 9.3.: Hyperfine spectra of the odd magnesium isotopes ^{25,27,29}Mg measured by classical fluorescence spectroscopy. The spectra are the sum of typically 20 individual scans. The solid line shows the full fit to the hyperfine structure. In the case of ^{29}Mg the scanning region was restricted to the hyperfine components because of low statistics.

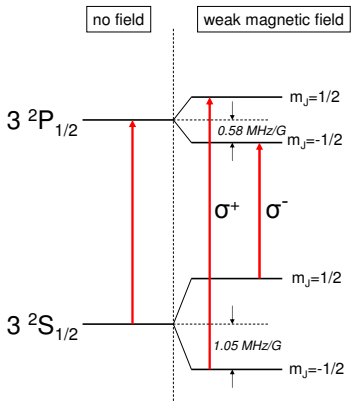

Figure 9.4.: Zeeman effect and the shift of the resonance frequency in ^{26}Mg for excitation with σ-polarized light.

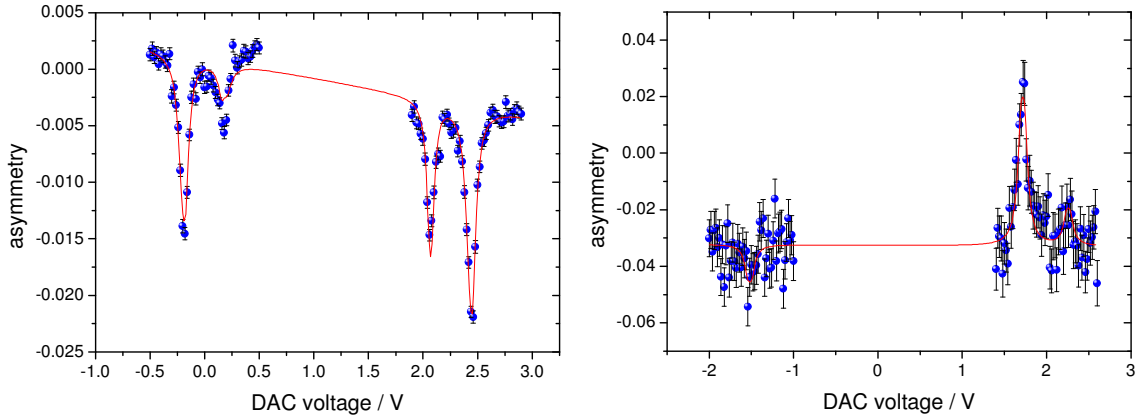

Figure 9.5.: β-asymmetry signals for the radioactive isotopes ^{29}Mg (a) and ^{31}Mg (b) for σ^- polarization together with the results from the fits with the calculated asymmetry from optical pumping.

detection, given in Tab. 9.1 are in excellent agreement within the uncertainties justifying our approach to connect both methods.

As the asymmetry measurements as well as the reference scans on ^{26}Mg all took place with the weak axial magnetic guiding field of ≈5 G turned on, the Zeeman effect has to be taken into account in the determination of the isotope shift. The asymmetry fitting routine already includes this effect for the calculation of the center of gravity, but the resonance positions of the reference isotope ^{26}Mg have to be corrected. Depending on the laser polarization and the selection rules for optical transitions in Zeeman substates, the real resonance position is shifted by $\delta\nu = \pm 1/2 \left(g_J\left(S_{1/2}\right) + g_J\left(P_{1/2}\right)\right) \mu_B B$ as it is indicated in Fig. 9.4. For the 5 G magnetic field and with the g_J factors $g_J\left(S_{1/2}\right) = 1.5$ and $g_J\left(P_{1/2}\right) = 0.83$ this results in a shift of ±8.2(8) MHz. This shift was considered before calculating the individual isotope shifts. The treatment of the asymmetry spectra and how the fitting function is composed was already described in Ch. 8.1. The spectra for both isotopes and for σ^- polarizations are presented in Fig. 9.5 together with the results of the least-squares fit.

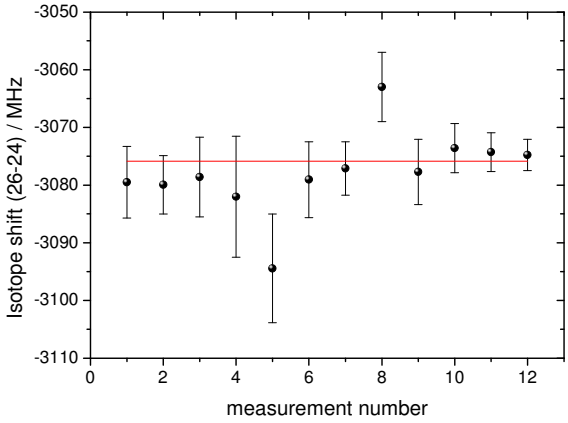

Figure 9.6.: Distribution of all individual isotope shifts between ^{24}Mg and ^{26}Mg used for the analysis. A fit of a constant to the data yields a $\chi^2_{red} \approx 1$.

For each isotope pair the individual measurements were plotted as a function of the measurement number. A fit to this data with a constant value corresponding to the mean was then performed to check the consistency of the statistical uncertainty ascribed to the individual data points by the fitting routine with the statistical distribution of the individual points. In case of too small uncertainties, resulting in a fit with a $\chi^2_{red} > 1$, the statistical uncertainties of the individual isotope shift measurements were afterwards scaled with the $\sqrt{\chi^2_{red}}$ obtained from this fit in order to ensure sufficiently large statistical uncertainties. This is particularly the case for the isotopes with high production yields where the good statistics typically delivers too small uncertainties. The result of such a fit after scaling the uncertainties is shown in Fig. 9.6 for the isotope shifts between ^{24}Mg and ^{26}Mg. These uncertainties were then used to calculate the weighted mean of the isotope shifts according to

$$\overline{x} = \frac{\sum_{i=1}^{N} x_i \frac{1}{\sigma_i^2}}{\sum_{i=1}^{N} \frac{1}{\sigma_i^2}}\,, \tag{9.2}$$

with σ_i the uncertainty of the individual measurement. The standard error of the weighted mean,

$$\Delta x = \frac{1}{\sqrt{\sum_{i=1}^{N} \frac{1}{\sigma_i^2}}}\,, \tag{9.3}$$

was then used as the final statistical uncertainty. One contribution to the systematic uncertainty arises from the determination of the source voltage U_{source}. This voltage is measured with a high voltage divider which was recently calibrated with the high-precision voltage divider as mentioned before. In addition, the actual potential at which the ions are produced may differ by a few volts from the applied source voltage. An overall relative contribution of 5×10^{-5} was considered. The voltage applied to the optical detection region is also measured with a recently calibrated high voltage divider. The relative uncertainty was estimated to 7×10^{-5} as the divider ratio may have been subject to thermal drifts since the calibration. The full expression for the uncertainty obtained from error propagation can be found in App. A.4

9.3. Extraction of the Nuclear Charge Radii

In order to extract the changes in the mean-square nuclear charge radii, data from radii determined with studies of muonic magnesium atoms need to be combined with theoretical calculations of the field shift constant. A King plot then yields the specific mass shift constant. Absolute radii can afterwards be calculated with a reference charge radius for one isotope.

9.3.1. King Plot and Mass Shift Constants

The isotope shift can be expressed by the mass-shift and the field-shift contribution according to (see Ch. 2.1.2):

$$\delta\nu^{A,A'} = \underbrace{(k_{\mathrm{NMS}} + k_{\mathrm{SMS}})}_{K_{\mathrm{MS}}} \times \frac{m_{A'} - m_A}{m_{A'} m_A} + F \times \delta \left\langle r^2 \right\rangle^{A,A'} . \tag{9.4}$$

For the field shift factor $F = -127(6)\,\mathrm{MHz/fm^2}$ we use *ab initio* calculations from Berengut *et al.* [Ber03] which for other alkali and alkali-earth metals have proven to be consistent with experimental values to better than 5%.

The normal-mass-shift constant can easily be calculated using the transition frequency ν_0 [Kau91] by

$$k_{\mathrm{NMS}} = -\nu_0 \times m_e = -586.618\,\mathrm{GHz\,u} \tag{9.5}$$

with the electron mass m_e in atomic mass units. To determine the mass-shift factor a King plot with the the known $\delta \left\langle r^2 \right\rangle$ from ^{24}Mg to ^{25}Mg and ^{26}Mg from muonic data [Fri92] based on the modified isotope shifts

$$\underbrace{\delta\nu^{A,A'}_{\text{our work}} \times \frac{m_A m_{A'}}{m_{A'} - m_A}}_{y} = K_{\mathrm{MS}} + F \times \underbrace{\delta \left\langle r^2 \right\rangle^{A,A'}_{\text{muon}} \frac{m_A m_{A'}}{m_{A'} - m_A}}_{x} \tag{9.6}$$

was evaluated. Plotting the y values as a function of the x values as indicated by the braces should result in a linear function and a linear fit with the field-shift constant as a fixed parameter allows to extract the mass-shift constant. Fig. 9.7 shows the resulting King plot. The solid red line is the result of the linear fit with the slope fixed to the theoretical value for F. The dashed lines are fits with the slope fixed to $F \pm \Delta F$. The total mass shift constant K_{MS}, *i.e.* the axis intercept extracted from the fit is $K_{\mathrm{MS}} = -954(1)\,\mathrm{GHz\,u}$ with the uncertainty composed of the statistical uncertainty from the fit and the systematic uncertainty of the field shift and its impact on the axis intercept. The specific mass shift constant can now be calculated to (see Ch. 2.1.2)

$$k_{\mathrm{SMS}} = K_{\mathrm{MS}} - k_{\mathrm{NMS}} = -367(1)\,\mathrm{GHz\,u}\,, \tag{9.7}$$

with the transition frequency ν and the electron mass m_e This value is in agreement with the theoretical value $k^{theo}_{\mathrm{SMS}} = -373(12)\,\mathrm{GHz\,u}$ derived in [Ber03] which has a too large uncertainty to use it for the evaluation of the radii directly.

9.3.2. Mean Square Nuclear Charge Radii

The $\delta \left\langle r^2 \right\rangle^{A,A'}$ can now be calculated for the isotope pairs from ^{24}Mg to ^{32}Mg. The results are summarized in Tab. 9.2 together with the absolute value for the radii which were calculated according to

$$\left\langle r^2_A \right\rangle^{1/2} = \left(\left\langle r^2_{26} \right\rangle + \delta \left\langle r^2 \right\rangle^{26,A} \right)^{1/2} , \tag{9.8}$$

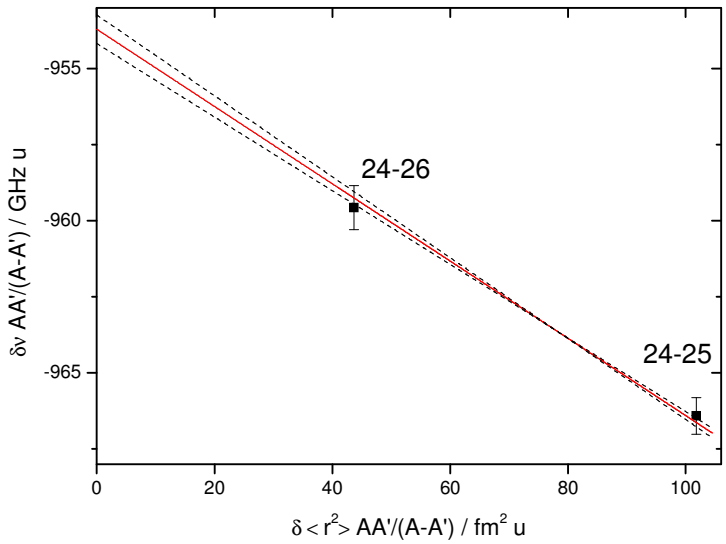

Figure 9.7.: King plot created from the experimental isotope shifts between ^{24,25,26}Mg obtained in this work and radii from muonic data. The solid red line indicates the least squares linear fit with the slope fixed to the theoretical electronic factor $F = -127(6)\,\mathrm{MHz/fm^2}$ [Ber03]. The dashed lines are fits with the slope fixed to $F + \Delta F$ and $F - \Delta F$, marking the boundaries for the slope of the line.

Table 9.2.: Mean square nuclear charge radii and absolute radii for ^{26}Mg up to ^{32}Mg. The first uncertainty given in brackets denotes the statistical uncertainties and the second number is the uncertainty in the determination of the mass shift constant. This uncertainty is changing the slope of the charge radius as a function of the atomic mass number as it is acting on all radii equally.

$(26, A')$	$\delta \langle r^2 \rangle^{26,A'}$ / fm^2	absolute radius r / fm
24	0.15 (2)(1)	3.060 (6)(70)
25	-0.02 (3)(1)	3.03 (1)(4)
26	-	3.035 (4)
27	0.01 (1)(1)	3.037 (3)(3)
28	0.21 (1)(2)	3.070 (3)(7)
29 *optical*	0.31 (1)(3)	3.084 (2)(10)
29 *asym.*	0.31 (2)(3)	3.085 (6)(10)
30	0.56 (2)(4)	3.125 (6)(15)
31	0.80 (2)(5)	3.163 (4)(20)
32	0.96 (2)(6)	3.190 (7)(20)

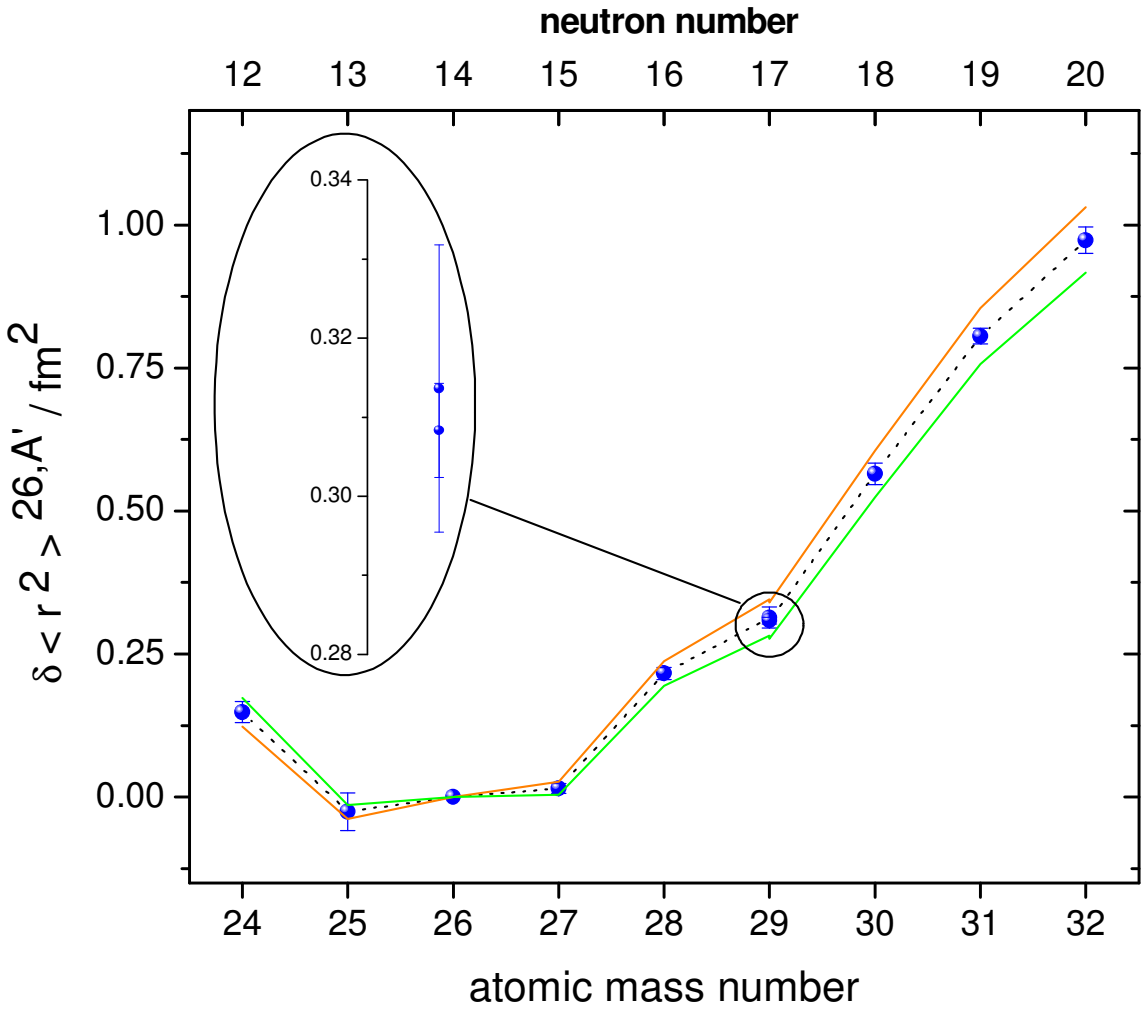

Figure 9.8.: Changes in the mean square nuclear charge radii of the neutron-rich Mg isotopes. The blue error bar denotes the statistical error in the voltages while the green and the red line indicate the limiting curves allowed by the uncertainty of the mass shift constant. The inset shows a magnified view of the two results for ^{29}Mg obtained with optical detection and asymmetry detection, respectively. The two values show excellent agreement within their uncertainties.

assuming a reference radius for ^{26}Mg of r_{26}=3.035(4) fm [Fri92]. The total statistical uncertainties have been calculated from the statistical uncertainties of the isotope shifts using Gaussian error propagation. The systematic uncertainty of the voltage determination is included in the mass-shift constant obtained from the King plot. This uncertainty approximately has the same mass dependence $\frac{m_A - m_{A'}}{m_A m_{A'}}$ as the mass shift. The field shift is therefore independent from this contribution. For more details refer to App. A.4. The remaining systematic uncertainty originates only from the uncertainty of the mass-shift constant determined from the King plot. All changes in radii were calculated based on the same mass-shift constant and therefore also the same uncertainty acts on the radii. The uncertainty therefore systematically changes all $\delta\langle r^2\rangle$. Two borders for the trend of the radii are defined by the uncertainty of the mass-shift constant. Fig. 9.8 shows the data presented in Tab. 9.2. The contribution of the mass shift constant uncertainty is indicated by the red and the green border curves.

9.4. Discussion

Many theoretical studies of nuclei near the $N = 20$ shell closure exist but the charge radius is addressed in only a few of them, whereas the deformation parameter β_2, describing the quadrupole deformation of the nucleus, is more often evaluated. To compare the experimental results obtained here to different nuclear models and calculations, the nuclear charge radius must thus be linked to the commonly used deformation parameter β_2. The droplet model is therefore used to calculate the changes in the mean-square charge radii as a function of theoretically derived deformations.

9.4.1. The Nuclear Charge Radius in the Droplet Model

The droplet model is a more refined substitute for the liquid-drop model with the main difference being the individual distributions of the neutrons and the protons. Therefore, the model can, for example, account for the development of neutron skins for neutron-rich nuclei. All coefficients were deduced from fitting to experimental data, as it was also done in the liquid-drop model. The nuclear charge radius is given by the expression [Mye83]

$$\langle r^2\rangle = \langle r^2\rangle_u + \langle r^2\rangle_r + \langle r^2\rangle_d \,, \tag{9.9}$$

with the size and shape contribution

$$\langle r^2\rangle_u = \frac{3}{5}R^2\left(1 + \alpha_2^2 + \frac{10}{21}\alpha_2^3 - \frac{27}{35}\alpha_2^4\right) . \tag{9.10}$$

The second term is a redistribution effect because of the Coulomb repulsion slightly increasing the proton density on the surface of the nucleus and is given by

$$\langle r^2\rangle_r = \frac{12}{175}C'R^2\left(1 + \frac{14}{5}\alpha_2^2 + \frac{28}{15}\alpha_2^3 - \frac{29}{5}\alpha_2^4\right) . \tag{9.11}$$

The parameter C' in Eq. 9.11 can be approximated to $C' \approx 0.0156 \times ZA^{-1/3}$. The last term in Eq. 9.9

$$\langle r^2\rangle_d = 3b^2 \,, \tag{9.12}$$

with $b = 0.99\,\text{fm}$, adds a constant contribution because of the diffuseness of the nucleus. The parameter α_2 can be expressed by the commonly used deformation parameter according to

$$\alpha_2 = \sqrt{\frac{5}{4\pi}}\beta_2 \,. \tag{9.13}$$

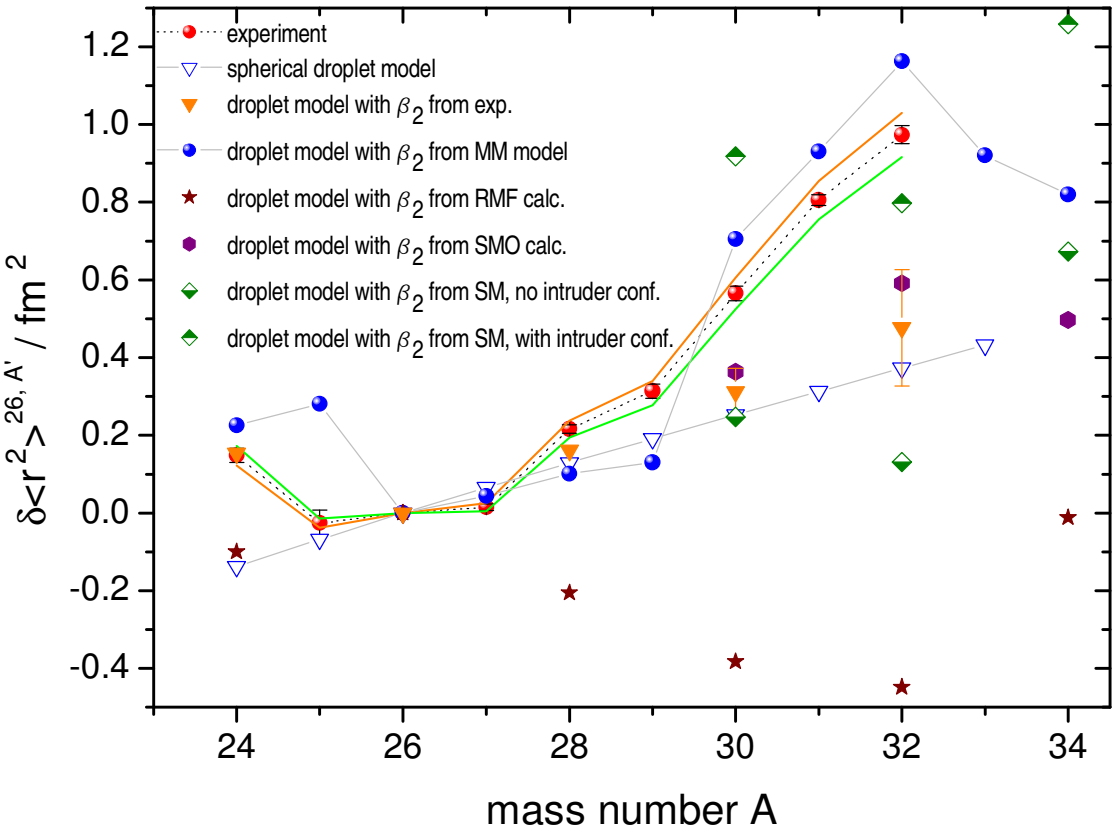

Figure 9.9.: Comparison of the experimental data to model predictions and theoretical calculations with reference to ^{26}Mg. The orange triangles are obtained from the droplet model with experimental deformation parameters from [Ram01]. The blue dots are results from the droplet model using the macroscopic-microscopic model (MM) according to [Zhi06]. The red stars are predictions from the relativistic mean-field calculations (RMF) with effective nucleon-nucleon interactions [Mit02] and the violet hexagons refer to mean-field calculations with density-dependent separable monopole nucleon-nucleon interaction (SMO) [Ste02]. The results from shell model calculations with and without intruder configurations in the ground state [Cau01] are shown by the half-filled green rhombs.

R is a measure for the size of the nucleus, including protons and neutrons, and is a modified liquid drop radius

$$R = r_0 A^{1/3} (1 + \bar{\epsilon}) \ , \tag{9.14}$$

with $r_0 = 1.18\,\mathrm{fm}$ and $\bar{\epsilon}$ defined according to [Mye83]. $\bar{\epsilon}$ depends on empirical parameters describing *e.g.* the ratio of the surface area of a deformed nucleus to the area of a sphere with the same volume or variations of the Coulomb potential for the transition from spherical to deformed nuclei.

Now we can calculate the changes in the mean square radii using deformation parameters from theory or other experiments and compare them with our results. A prediction for purely spherical configurations can be achieved by fixing β to zero for all isotopes. The trend of the charge radii for this simplified model can be seen in Fig. 9.9 indicated by the blue triangles. Good agreement is observed for radii radii from ^{25}Mg up to ^{27}Mg. For the nucleus ^{24}Mg with well known deformation there is a big discrepancy, and also the isotopes $^{29-32}$Mg deviate considerably from the predictions of the spherical droplet model, which may be a hint for the onset of intruder configurations in the ground states of these isotopes. The calculation of the charge radii with deformation parameters from experimental $B\,(E2)$ values deduced from electron scattering and Coulomb excitation measurements for even-even nuclei [Ram01] shown as orange triangles in Fig. 9.9 is in good agreement from ^{24}Mg up to ^{28}Mg. For the more exotic isotopes however, our measurement exhibits a slightly steeper slope for the radii changes.

The use of the β_2 predictions from the macroscopic-microscopic (MM) model [Zhi06] in our droplet radii calculation shows the best agreement with the present data set. Only the $\delta\left\langle r^2\right\rangle$ for ^{25}Mg deviates by more than five times the error bars from the experimental result. This theoretical description combines a macroscopic model for the nucleus, in this case the liquid-drop model, with a microscopic model accounting for shell effects by spin-orbit interactions and pairing effects [Nil69]. The sum of the total energy derived by both models is then minimized to determine the ground-state configuration. Zhi and Ren [Zhi06] refined the microscopic model by employing isospin-dependent spin-orbit interaction parameters, κ and μ, which describe the effects of the proton-neutron interactions in light exotic nuclei. This may be the foundation of the good agreement with the experimental data, as the reordering and lowering of single-particle orbits, being an attribute of the island of inversion, can be linked to nucleon-nucleon interactions [Uts99]. One should note that the ϵ_2 parameter used in [Zhi06] refers to a different nuclear shape parameterization [Mol95]. But ϵ_2 can be transformed into the commonly used β_2. Therefore, a graph is plotted in [Nil69] showing the relation between the parameters that was used here for a graphical conversion from ϵ_2 into β_2, which were then used to calculate the changes in the radii.

The relativistic mean field approach (RMF) [Mit02] is a fully relativistic quantum field theory which treats the nucleons as Dirac spinors interacting with each other by meson exchange [Rin96]. The mean-field approximation is used to reduce the number of allowed meson interactions based on symmetry considerations. The nucleonic quantum numbers, the coupling constants, and the nucleon mass, *i.e.* the parameters of the Lagrange density used to calculate the total energy of the system, are adjusted in order to give the best agreement to known experimental data. There are a number of standard parameter sets often used in the calculations. The pairing effect on the total energy is included in the theory by the BCS formalism [Moe92]. The agreement of the charge radii derived from this theory with our results and with all other predictions shown in Fig. 9.9 is poor. The progress of the radii does not even show the correct trend and predicts a spherical nucleus for ^{32}Mg.

Qualitatively good agreement with the experimental results is observed for the many-body perturbative mean-field approach with density-dependent separable monopole nucleon-nucleon

interactions (SMO) [Ste01b]. In this theory the wave function for the ground state of the nucleus is described by a Slater determinant of the single-particle states [Vau72]. A Hartree-Fock approximation for the nucleon-nucleon interaction is used in which the individual nucleon is described as a particle interacting with a mean field produced by the other nucleons. For this mean field Stevenson *et al.* use the SMO interaction [Ste01a]. The trend of the $\delta\langle r^2\rangle$ is well reproduced and also the decrease in the radii for nuclei with $A > 32$ predicted by the MM model is well pronounced.

In contrast to the Hartree-Fock method the shell model calculations involve nuclear wave functions as linear combinations of Slater determinants. In Fig. 9.9 the predictions from this model are shown as half-filled green rhombs. The Hamiltonian consists of kinetic energy operators for the nucleons and two-body interactions between protons and neutrons. A special diagonalization scheme is used to calculate the coefficients of the wave functions [Cau99]. From the shell model point of view, the large deformations of the magnesium isotopes for $A > 30$ are accompanied by the lowering of the pf orbits and intruder configurations mixing to the ground states in addition to the normal sd configurations [Cau01]. The significance of these particle hole-excitations to the pf shell in the explanation of the experimental deformation properties of ^{32}Mg is very well illustrated in the comparison of the shell-model predictions for the normal and the intruder configuration. The $\delta\langle r^2\rangle$ deduced from the simulation with normal configuration is too small, predicting a smaller radius than for ^{30}Mg, while the simulation involving the intruder states gives reasonable agreement with our data. For ^{34}Mg the normal configuration without particle-hole excitations gives better agreement with the macroscopic-microscopic model. In the case of ^{30}Mg our result lies between the predicted radii from the shell model for normal or intruder configuration.

In summary, the experimental charge radii show a clear deviation from the predictions of the spherical shell model. Only models that account for nuclear deformations can describe the changes in the mean square nuclear charge radii qualitatively correct. However, the best agreement is achieved by the macroscopic-microscopic model that reproduces the experimental radii rather well.

9.4.2. Comparison to Other Isotope Chains at the Island of Inversion

Magnesium is not the only element which exhibits intruder configurations and large deformations in the ground states when neutron-rich isotopes are considered. Similar experimental observations have been made with sodium [Thi75, Wil80] and neon [Pri99] for which isotope shift measurements are also available [Hub78, Gei02]. For comparison, the result for the charge radii for the three elements are plotted together as a function of the neutron number in Fig. 9.10. All three chains show similar behavior with a minimum for the radius around $N = 14$ and increasing radii to both sides. Na and Mg show the same increase in the slope from $N = 17$ to $N = 18$. While this trend in the case of Na is caused by the onset of intruder configurations [Wil80], the normal ground state configuration of ^{30}Mg can already explain the significant increase in deformation that is observed.

9.5. Summary and Outlook

In this thesis the preceding work on the nuclear structure of magnesium isotopes studied with collinear laser spectroscopy [Yor07b, Kow06] was continued. The spin and the magnetic moment of the neutron-deficient isotope ^{21}Mg were measured for the first time, which allowed to study the properties of mirror nuclei in one of the few accessible cases for $T_z = -3/2$. An anomaly in the

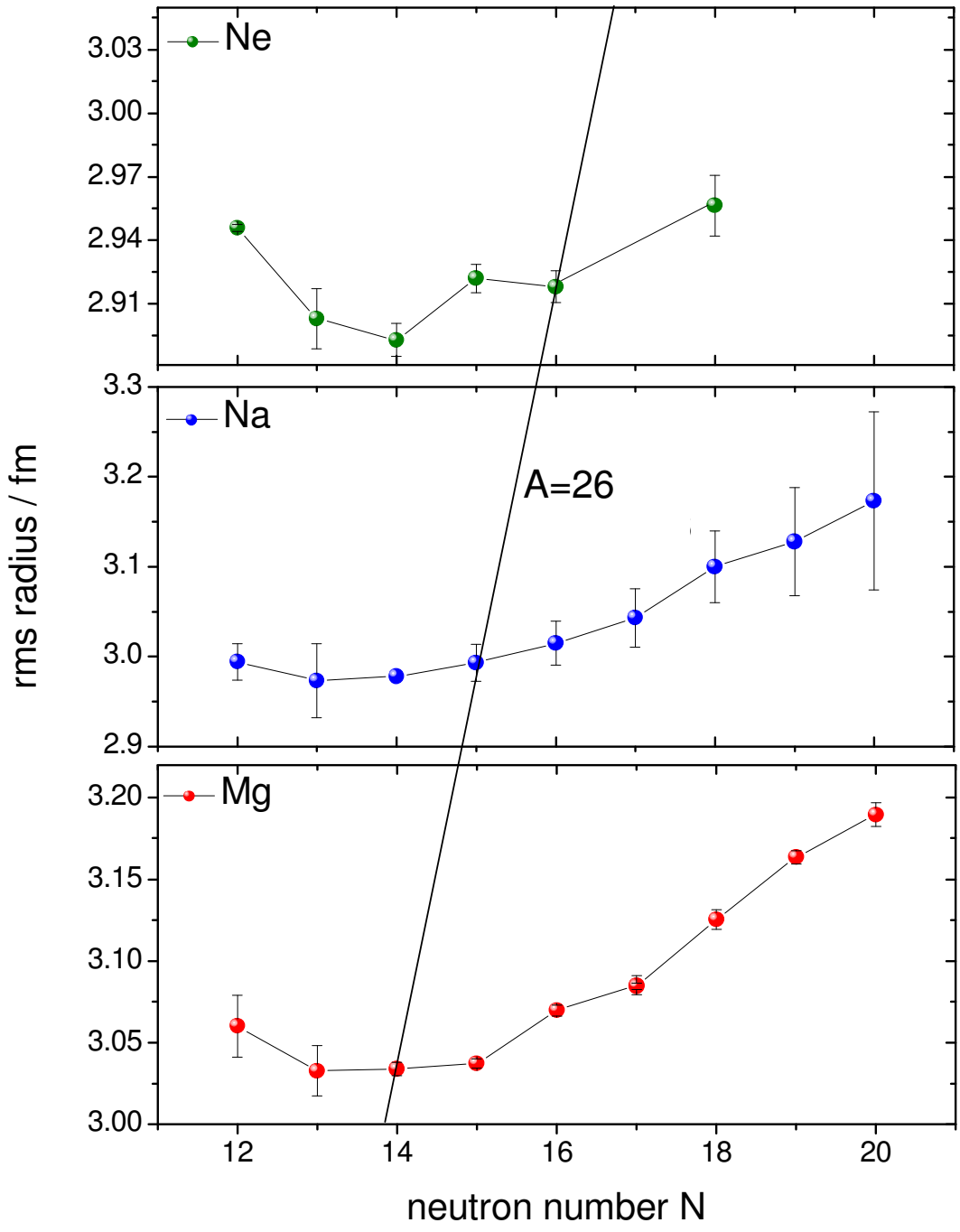

Figure 9.10.: Charge radii of magnesium isotopes together with the results for sodium and neon as a function of the neutron number. The red dots show the results of our work. The blue dots refer to the sodium data [Hub78] and the green dots are the radii of the neon isotopes [Gei02]. The systematic uncertainties due to the uncertainty in the mass shift constant were omitted as they would not change the qualitative trend in the radii, but only the slopes. The line crossing the three plots connects the $A = 26$ isobars of the three elements.

isoscalar magnetic moment was revealed, which can be reproduced by shell model calculations by taking isospin non-conserving effects into account.

Furthermore, the measurement of the isotope shift of the $^{24-32}$Mg isotope chain with combined optical spectroscopy and β-asymmetry detection induced by optical pumping allowed to study the structural changes at the transition to the island of inversion, where intruder states contribute significantly to the ground-state configuration. Our measurement has shown that the change from the normal configuration for ^{30}Mg to the intruder configuration for ^{31}Mg is visible only in a small kink in the changes in charge radii as there is already a significant deformation in the ground state for ^{30}Mg. Our measurements are in good agreement with predictions of deformation parameters from the macroscopic-microscopic model [Zhi06].

To complete the work on the magnesium isotopes the radii for the neutron-deficient $^{21-24}$Mg will be measured in 2010, again combining β detection with classical optical detection. These results together with the results presented in this thesis will give an insight to the evolution of nuclear shape throughout the whole *sd* shell.

A. Basic Formulas for Collinear Laser Spectroscopy

A.1. Relativistic Doppler Formula

The Doppler shifted frequency that a particle with rest mass m moving with the velocity $v = \beta c$ experiences from a laser superimposed in parallel or anti-parallel direction is given by

$$\nu' = \nu_{laser} \times \frac{1 \pm \beta}{\sqrt{1-\beta^2}}\,, \tag{A.1}$$

where the - applies for collinear geometry and the + for anti-collinear laser-particle geometry. The β can be calculated from the energy conservation for a particle being accelerated by the potential difference U in a homogeneous electric field according to

$$eU = mc^2 \left(\frac{1}{\sqrt{1-\beta^2}} - 1 \right) . \tag{A.2}$$

This can be solved for β:

$$\beta = \sqrt{1 - \left(\frac{mc^2}{eU + mc^2} \right)^2} . \tag{A.3}$$

The result can be inserted in Eq. A.1 and the Doppler shifted frequency as a function of the acceleration voltage is

$$\nu' = \nu_{laser} \frac{\left(eU + mc^2\right)}{mc^2} \left(1 \pm \sqrt{1 - \left(\frac{mc^2}{eU + mc^2} \right)^2} \right) . \tag{A.4}$$

A.2. Relativistic Isotope Shift Formula

The isotope shift between two isotopes of mass m_1 and m_2 with the resonance positions given by the total acceleration voltages U_1 and U_2 can be calculated by

$$\Delta\nu_{IS} = \nu_{laser} \times \left\{ \frac{\left(eU_1 + m_1c^2\right)}{m_1c^2} \left(1 \pm \sqrt{1 - \left(\frac{m_1c^2}{eU_1 + m_1c^2} \right)^2} \right) \right. \tag{A.5}$$

$$\left. - \frac{\left(eU_2 + m_2c^2\right)}{m_2c^2} \left(1 \pm \sqrt{1 - \left(\frac{m_2c^2}{eU_2 + m_2c^2} \right)^2} \right) \right\} \tag{A.6}$$

with the negative sign for collinear and the positive sign for anti-collinear geometry.

A.3. Differential Doppler Formula - Doppler Factor

Starting from the classical approximation of the Doppler shift

$$\nu' \approx \nu_{laser} \times \left(1 \pm \sqrt{\frac{2eU}{mc^2}}\right) , \tag{A.7}$$

the Doppler factor is the differential change $\partial\nu'$ in the frequency for a voltage change ∂U:

$$\partial\nu' = \frac{\nu_{laser} e}{\sqrt{2eUmc^2}} \partial U \tag{A.8}$$

A.4. Systematic Uncertainty of the Voltage Determination in the Isotope Shift

In the non-relativistic treatment of the Doppler effect the isotope shift is given by

$$\Delta\nu = \nu_0 \left(\sqrt{\frac{2eU_1}{m_1c^2}} - \sqrt{\frac{2eU_2}{m_2c^2}}\right) . \tag{A.9}$$

With the substitutions $U_1 = U_{\text{source}} + U^{(1)}_{\text{offset}}$ and $U_2 = U_{\text{source}} + U^{(2)}_{\text{offset}}$, where $U^{(i)}_{\text{offset}}$ denotes the offset voltage applied to the optical detection setup, and $m_2 = m_1 + \Delta m \equiv m + \Delta m$ this can be modified to

$$\Delta\nu = \nu_0 \sqrt{\frac{2eU_{source}}{mc^2}} \left(\sqrt{\frac{U^{(1)}_{\text{offset}}}{U_{\text{source}}}} - \sqrt{\frac{U^{(2)}_{\text{offset}}/U_{\text{source}}}{\Delta m/m}}\right) . \tag{A.10}$$

A Taylor expansion of the square root and the approximation $1 + \Delta m/(2m) \approx 1$ gives the final result for an approximated isotope shift:

$$\Delta\nu \approx \nu_0 \sqrt{\frac{2eU_{\text{source}}}{2mc^2}} \left(\frac{\Delta m}{m} - \frac{\Delta U}{U_{\text{source}}}\right) , \tag{A.11}$$

with $\Delta U = U^{(2)}_{\text{offset}} - U^{(1)}_{\text{offset}}$. Based on Eq. A.11 the error propagation for the systematic voltage uncertainty can be calculated. The result for the relative uncertainty of U_{offset} $\sigma\left(\Delta U\right)^{\text{rel}}$ is

$$\sigma\left(\Delta\nu\right)^{\text{offset}} = \nu_0 \sqrt{\frac{eU_{\text{source}}}{2mc^2}} \frac{\Delta U}{U_{\text{source}}} \sigma\left(\Delta U\right)^{\text{rel}} . \tag{A.12}$$

With the approximation that the isotope shift is mainly given by the mass shift, the expression can be modified to

$$\sigma\left(\Delta\nu\right)^{\text{offset}} \approx C \frac{m_A - m_{A'}}{m_A m_{A'}} \tag{A.13}$$

and thus shows the same mass dependence as the mass shift. This allows to omit this uncertainty in the change of the nuclear charge radii, if the mass shift constant is determined with a King plot. The voltage uncertainty is then implicitly included.

The uncertainty of the source voltage determination can be modified in a similar way and is given by

$$\sigma\left(\Delta\nu\right)^{\text{source}} = \nu_0/2 \sqrt{\frac{eU_{\text{source}}}{2mc^2}} \left(\frac{\Delta U}{U_{\text{source}}} + \frac{\Delta m}{m}\right) \sigma\left(U_{\text{source}}\right)^{\text{rel}} . \tag{A.14}$$

B. Instruction for the import of 3D models from Solid Edge to SIMION 8.0

We start with an assembled body (.asm) consisting of several parts (.par). SIMION is capable of importing 3D CAD files in .stl format. The construction file of the assembly needs to be converted stepwise to individual .stl files for each electrode. Isolators have to be omitted.

B.1. Selection of individual components belonging to one electrode

All parts not belonging to the electrode we want to export can simply be deleted. Please note that the file must not be saved! (A backup copy is recommended!) If some of the components are part of sub assemblies, then these sub assemblies have to be *opened* and the parts have to be deleted there (do not save!). In no case use the function "Bearbeiten" or "Modify" as every change will be saved immediately and the original file will be lost.

B.2. Insertion into a new part and saving to .stl

When only the parts of the single electrode are left, choose "Neues Teil erstellen" or "create new part". Now click the function "Einfügen–Kopie eines Teils" or 'Insert–part copy" and choose the main assembly you have worked on. You will see the one single electrode appear. Now you can save this part as e.g. "part-1.stl". Now all open files can be closed and you can proceed with the second electrode. By doing so in the same way you can be sure that all electrodes have their pre-defined positions, as they are all positioned with respect to the same coordinate system.

B.3. Conversion to the .pa♯ format of SIMION 8.0

For the conversion the SIMION add-on "SL-Tools" is used, which is included in SIMION 8.0. You choose the function "STL→PA" and the file to convert. To include several electrodes in one .pa♯, you simply replace the electrode number with "%" and SIMION will automatically look for all files belonging to this geometry. Using the function "scale" you can influence the resolution of your conversion. After refining and creation of the .pa0 file, the scale can be adjusted to match the real dimensions of your geometry.

C. FEM Structural Analysis for the Design of the Vacuum Chambers

The technical design of the vacuum housings not only needs to take into account the compatibility to existing flange standards and the careful design of seal grooves and sealing surfaces, but also the mechanical strength of the material. The ambient atmospheric pressure acting on a chamber under vacuum can easily result in a total force equivalent to the weight of several tons leading to elastic deformations of the surface and high mechanical tension on the joints. To ensure a wall thickness sufficient to keep the deformations small, a finite-element method (FEM) analysis [Fro05] was performed with the program FEMAP Express, included in the Solid Edge 3D CAD package. Therefore, the 3D body was divided up into a mesh of triangles with finite number of knots which are all subject to a force corresponding to the atmospheric pressure on one side and vacuum on the other side. A global boundary condition was then defined by fixing the outer part of the body, which corresponds to screwing the top part of the switchyard to the chamber. A system of coupled ordinary differential equations defined by Hooke's law of elasticity was then solved numerically by the program with the objective to minimize the potential energy of the whole system. The result is the color-coded overview of the deflection of each knot in the mesh, shown in Fig. C.1, which supports the decision of choosing a wall thickness of 1 mm.

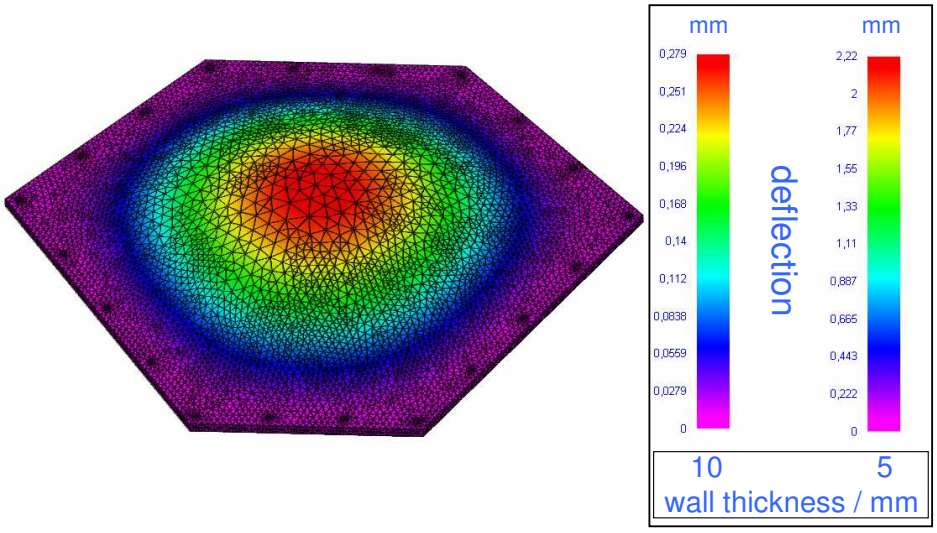

Figure C.1.: FEM calculation of the mechanical deflection of the stainless steel 304 switchyard cover under atmospheric pressure. The caption to the right shows the deflection for two wall thicknesses, 10 mm and 5 mm. As a result of this calculation the vacuum chamber was finally machined from 10 mm steel metal sheet as the resulting deflection also expected to happen at the bottom part of the chamber, carrying the electrostatic deflectors, is negligible.

Bibliography

[Ä01] J. Äystö. *Development and applications of the IGISOL technique.* Nuclear Physics A, 693:477–494, 2001.

[Alc84] C. B. Alcock, V. P. Itkin, and M. K. Horrigan. *Vapor pressure of the metallic elements.* Can. Metall. Q., 23:309–313, 1984.

[Ant78] K. R. Anton, S. L. Kaufman, W. Klempt, R. Neugart, E. W. Otten, and B. Schinzler. *Narrowed optical lines observed in laser method for use with accelerated beams.* Hyperfine Interactions, 4(1):87–90, 1978.

[Aud03] G. Audi, A. H. Wapstra, and C. Thibault. *The 2003 atomic mass evaluation: (II). tables, graphs and references.* Nuclear Physics A, 729(1):337–676, 2003.

[Baa97] R. Baartman. *60 keV beam transport line and switchyard for ISAC.* American Physical Society, Particle Acceleration Meeting, page 2778, 1997.

[Bac74] M. Bacal and W. Reichelt. *Metal vapor confinement in vacuum.* Rev. Sci. Instrum., 45(6):769–772, 1974.

[Bat09] V. Batteiger, S. Knuenz, M. Herrmann, G. Saathoff, H. A. Schuessler, B. Bernhardt, T. Wilken, R. Holzwarth, T. W. Haensch, and Th. Udem. *Precision spectroscopy of the $3s - 3p$ fine-structure doublet in Mg^+.* Phys. Rev. A, 80(2):022503, Aug 2009. doi:10.1103/PhysRevA.80.022503.

[Ben86] N. Bendali, H.T. Duong, P. Juncar, J.M. Saint Jalm, and J.L. Vialle. *Na+ -Na charge exchange processes studied by collinear laser spectroscopy.* Journal of Physics B: Atomic and Molecular Physics, 19(2):233, 1986.

[Ber03] J. C. Berengut, V. A. Dzuba, and V. V. Flambaum. *Isotope-shift calculations for atoms with one valence electron.* Phys. Rev. A, 68(2):022502, Aug 2003. doi: 10.1103/PhysRevA.68.022502.

[Bet08] K. Bethge, G. Walter, and B. Wiedemann. *Kernphysik.* Springer, Berlin, 2008.

[Bru85] M. Bruegger, N. Hildebrand, T. Karlewski, N. Trautmann, A.K. Mazumdar, and G. Herrmann. *Operation of a high temperature ion source at the helium-jet on-line isotope separator facility HELIOS.* Nuclear Instruments and Methods in Physics Research Section A: Accelerators, Spectrometers, Detectors and Associated Equipment, 234(2):218 – 223, 1985. ISSN 0168-9002. doi:DOI: 10.1016/0168-9002(85)90908-8.

[Bur54] B. F. Burke, M. W. P. Strandberg, V. W. Cohen, and W. S. Koski. *The nuclear magnetic moment of S-35 by microwave spectroscopy.* Physical Review, 93(1):193–194, 1954.

[Cau99] E. Caurier and F. Nowacki. *Present status of shell-model techniques.* Acta Physica Polonica B, 30:705, 1999.

[Cau01] E. Caurier, F. Nowacki, and A. Poves. *Shell model studies of neutron-rich nuclei.* Nuclear Physics A, 693(1-2):374 – 382, 2001. ISSN 0375-9474. doi:DOI: 10.1016/S0375-9474(00)00579-0.

[Cau06] E. Caurier. *Shell-model code ANTOINE.* http://sbgat194.in2p3.fr/theory/antoine, 1989-2006.

[Cha09] F.C. Charlwood, K. Baczynska, J. Billowes, P. Campbell, B. Cheal, T. Eronen, D.H. Forest, A. Jokinen, T. Kessler, I.D. Moore, H. Penttilae, R. Powis, M. Rueffer, A. Saastamoinen, G. Tungate, and J. Aeystoe. *Nuclear charge radii of molybdenum fission fragments.* Physics Letters B, 674(1):23 – 27, 2009. ISSN 0370-2693. doi:DOI: 10.1016/j.physletb.2009.02.050.

[Cor83] F. D. Correll, L. Madansky, R. A. Hardekopf, and J. W. Sunier. *Nuclear moments of 9Li.* Physical Review C, 28:862–874, 1983.

[Dah90] D. A. Dahl, J. E. Delmore, and A. D. Appelhans. *SIMION PC/PS2 electrostatic lens design program.* volume 61, pages 607–609. AIP, 1990. doi:10.1063/1.1141932.

[Dem93] W. Demtroeder. *Laserspektroskopie.* Springer Verlag, Berlin, 1993.

[Dra06] G.W.F. Drake. *Handbook of Atomic, Molecular and Optical Physics.* Springer, New York, 2006.

[Dre68] M. J. Dresser. *The saha-langmuir equation and its application.* Journal of Applied Physics, 39(1):338–339, 1968. doi:10.1063/1.1655755.

[Eas86] D. A. Eastham, P. M. Walker, J. R. H. Smith, J. A. R. Griffith, D. E. Evans, S. A. Wells, M. J. Fawcett, and I. S. Grant. *Coincidence laser spectroscopy - a new ultrasensitive technique for fast ionic or atomic-beams.* Optics Communications, 60(5):293–295, 1986.

[Eng10] Photon Engineering. *FRED.* http://www.photonengr.com/index.html, 2010.

[Fed79] P. Federman and S. Pittel. *Unified shell-model description of nuclear deformation.* Phys. Rev. C, 20(2):820–829, Aug 1979. doi:10.1103/PhysRevC.20.820.

[Fir04] R.B. Firestone. *Nuclear data sheets for A = 21.* Nuclear Data Sheets, 103(2):269 – 324, 2004. ISSN 0090-3752. doi:DOI: 10.1016/j.nds.2004.11.003.

[Fir10] *LBL fission homepage.* http://ie.lbl.gov/fission/249cft.txt, 2010.

[Fri92] G. Fricke, J. Herberz, Th. Hennemann, G. Mallot, L. A. Schaller, L. Schellenberg, C. Piller, and R. Jacot-Guillarmod. *Behavior of the nuclear charge radii systematics in the s-d shell from muonic atom measurements.* Phys. Rev. C, 45(1):80–89, Jan 1992. doi:10.1103/PhysRevC.45.80.

[Fro05] P. Froehlich. *FEM Anwendungspraxis, Einstieg in die Finite Elemente Analyse.* Vieweg, Wiesbaden, 2005.

[Gei02] R. W. Geithner. *Nuclear Moments and Differences in Mean Square Charge Radii of Short-Lived Neon Isotopes by Collinear Laser Spectroscopy.* Dissertation, Johannes Gutenberg-Universitaet, 2002.

[Gei05] W. Geithner, B. A. Brown, K. M. Hilligsoe, S. Kappertz, M. Keim, G. Kotrotsios, P. Lievens, K. Marinova, R. Neugart, H. Simon, and S. Wilbert. *Nuclear moments of neon isotopes in the range from ^{17}Ne at the proton drip line to neutron-rich ^{25}Ne.* Phys. Rev. C, 71(064319), 2005.

[Gep00] Ch. Geppert. *Optimierung der Atomstrahlquelle und der Laser-Ionisationsregion fuer die resonante Laserionisations-Massenspektrometrie.* Diplomarbeit, Johannes Gutenberg-Universitaet Mainz, 2000.

[Gep10] Ch. Geppert. *Private communication*, 2010.

[Ham10] M. Hammen. *Konstruktion, Aufbau und Test eines effizienten Fluoreszenznachweises fuer die kollineare Laserspektroskopie am TRIGA Mainz.* Diplomarbeit, Johannes Gutenberg-Universitaet Mainz, 2010.

[Has64] J. B. Hasted. *Physics of Atomic Collisions.* Butterworths, London, UK, 1964.

[Her08] I.V. Hertel and C.P. Schulz. *Atome, Molekuele und optische Physik.* Springer, Berlin, 2008.

[Hub78] G. Huber, F. Touchard, S. Buettgenbach, C. Thibault, R. Klapisch, H. T. Duong, S. Liberman, J. Pinard, J. L. Vialle, P. Juncar, and P. Jacquinot. *Spins, magnetic moments, and isotope shifts of $^{21-31}Na$ by high resolution laser spectroscopy of the atomic D_1 line.* Phys. Rev. C, 18(5):2342–2354, Nov 1978. doi:10.1103/PhysRevC.18.2342.

[Huh98] M. Huhta, P. F. Mantica, D. W. Anthony, B. A. Brown, B. S. Davids, R. W. Ibbotson, D. J. Morrissey, C. F. Powell, and M. Steiner. *Anomalous p-shell isoscalar magnetic moments: Remeasurement of ^{9}C and the influence of isospin nonconservation.* Phys. Rev. C, 57:R2790, 1998.

[Iso10] *ISOLDE homepage.* http://isolde.web.cern.ch/ISOLDE/, 2010.

[Ita81] W. M. Itano and D. J. Wineland. *Precision measurement of the ground-state hyperfine constant of $^{25}Mg^{+}$.* Phys. Rev. A, 24(3):1364–1373, Sep 1981. doi: 10.1103/PhysRevA.24.1364.

[Jul92] R. E. Julies, W. A. Richter, and B. A. Brown. *The 0p shell revisited.* S. Afr. J. Phys., 15:35, 1992.

[Kau91] V. Kaufman and W. C. Martin. *Wavelengths and energy level classifications of magnesium spectra for all stages of ionization (Mg I through Mg XII).* Journal of Physical and Chemical Reference Data, 20(1):83–152, 1991. doi:10.1063/1.555879.

[Kei00] M. Keim, U. Georg, A. Klein, R. Neugart, M. Neuroth, S. Wilbert, P. Lievens, L. Vermeeren, B. Brown, and Isolde Collaboration. *Measurement of the electric quadrupole moments of ^{2629}Na.* The European Physical Journal A - Hadrons and Nuclei, 8(1):31–40, 2000. 10.1007/s100500070117.

[Ket08] J. Ketelaer, J. Kraemer, D. Beck, K. Blaum, M. Block, K. Eberhardt, G. Eitel, R. Ferrer, C. Geppert, S. George, F. Herfurth, J. Ketter, Sz. Nagy, D. Neidherr, R. Neugart, W. Noertershaeuser, J. Repp, C. Smorra, N. Trautmann, and C. Weber. *TRIGA-SPEC: A setup for mass spectrometry and laser spectroscopy at the research reactor TRIGA mainz.* Nuclear Instruments and Methods in Physics Research Section A:

Accelerators, Spectrometers, Detectors and Associated Equipment, 594(2):162 – 177, 2008. ISSN 0168-9002. doi:DOI: 10.1016/j.nima.2008.06.023.

[Kle79] W. Klempt, J. Bonn, and R. Neugart. *Nuclear moments and charge radii of neutron-rich Rb isotopes by fast-beam laser spectroscopy.* Physics Letters B, 82(1):47 – 50, 1979. ISSN 0370-2693. doi:DOI: 10.1016/0370-2693(79)90422-2.

[Koe03] U. Koester, V. N. Fedoseyev, A. N. Andreyev, U. C. Bergmann, R. Catherall, and J. Cederkaell et al. *On-line yields obtained with the ISOLDE RILIS.* Nuclear Instruments and Methods in Physics Research Section B: Beam Interactions with Materials and Atoms, 204:347 – 352, 2003. ISSN 0168-583X. doi:DOI: 10.1016/S0168-583X(02)01956-0. 14th International Conference on Electromagnetic Isotope Separators and Techniques Related to their Applications.

[Kon59] E J Konopinski. *The experimental clarification of the laws of beta-radioactivity.* Annual Review of Nuclear Science, 9(1):99–158, 1959. doi: 10.1146/annurev.ns.09.120159.000531.

[Kow06] M. Kowalska. *Ground state properties of neutron-rich Mg isotopes the "island of inversion" studied with laser and β-NMR spectroscopy.* Dissertation, Johannes Gutenberg-Universitaet Mainz, 2006.

[Kri10] A. Krieger. *Voltage calibration of the ISOLDE high voltage platforms using a high precision voltage divider and applying collinear fast beam spectroscopy.* submitted to Nucl. Instrum. Methods Phys. Res., Sect. B, (-):–, 2010.

[Lid97] D.R. Lide. *Handbook of Chemistry and Physics.* CRC Press, Boca Raton, Florida, 1997.

[Lun09] D. Lunney, C. Bachelet, C. Gunaut, S. Henry, and M. Sewtz. *COLETTE: A linear Paul-trap beam cooler for the on-line mass spectrometer MISTRAL.* Nuclear Instruments and Methods in Physics Research Section A: Accelerators, Spectrometers, Detectors and Associated Equipment, 598(2):379 – 387, 2009. ISSN 0168-9002. doi:DOI: 10.1016/j.nima.2008.09.050.

[Man98] P. F. Mantica, D. W. Anthony, B. A. Brown, B. Davids, G. Georgiev, M. Huhta, R. W. Ibbotson, P. A. Lofy, J. I. Prisciandro, and M. Steiner. *Isospin nonconserving effects in light, $T_z = -3/2$ nuclei.* AIP Conf. Proc., 455:66–71, 1998.

[Mat95] K. Matsuta, M. Fukuda, Tanigaki M., M. T. Minamisono, Y. Nojiri, M. Mihara, T. Onishi, T. Yamaguchi, A. Harada, M. Sasaki, T. Miyake, S. Fukuda, K. Yoshida, A. Ozawa, T. Kobayashi, I. Tanihata, J. R. Alonso, G. F. Krebs, and T. J. M. Symons. *Magnetic moment of proton drip-line nucleus ^9c.* Nucl. Phys. A, 588:153, 1995.

[Mat96] K. Matsuta, T. Minamisono, M. Tanigaki, M. Fukuda, Y. Nojiri, M. Mihara, T. Onishi, T. Yamaguchi, A. Harada, M. Sasaki, T. Miyake, K. Minamisono, T. Fukao, K. Sato, Y. Matsumoto, T. Ohtsubo, S. Fukuda, S. Momota, K. Yoshida, A. Ozawa, T. Kobayashi, I. Tanihata, J. R. Alonso, G. F. Krebs, and T. J. M. Symons. *Magnetic moments of proton drip-line nuclei O-13 and C-9.* Hyperfine Interactions, 97-8(1-4):519–526, 1996.

[Mat99] K. Matsuta, T. Onishi, M. Fukuda, T. Minamisono, H. Akai, M. Sasaki, T. Yamaguchi, T. Miyake, K. Sato, K. Minamisono, F. Ohsumi, Y. Muramoto, S. Oui, C. Ha, K. Tanaka, K. Kidera, A. Morishita, A. Kitagawa, M. Torikoshi, M. Kanazawa, T. Nishio, S. Koda, T. Ohtsubo, S. Fukuda, Y. Nojiri, S. Momota, A. Ozawa, K. Yoshida, T. Suzuki, T. Kobayashi, I. Tanihata, S. S. Hanna, J. R. Alonso, G. F. Krebs, and T. J. M. Symons. *Electromagnetic moments of short lived beta emitters F-21, Mg-23, Si-27 and Ca-39.* Hyperfine Interactions, 121(1-8):673–677, 1999.

[Maz76] A.K. Mazumdar, H. Wagner, W. Walcher, and T. Lund. *Connection experiments with a hollow cathode ion source and a helium gas jet system for on-line isotope separation.* Nuclear Instruments and Methods, 139:319 – 323, 1976. ISSN 0029-554X. doi:DOI: 10.1016/0029-554X(76)90692-3.

[Mer06] T. J. Mertzimekis, P. F. Mantica, A. D. Davies, S. N. Liddick, and B. E. Tomlin. *Ground state magnetic dipole moment of K-35.* Physical Review C, 73(2):024318, 2006.

[Mis93] V.I. Mishin, V.N. Fedoseyev, H.-J. Kluge, V.S. Letokhov, H.L. Ravn, F. Scheerer, Y. Shirakabe, S. Sundell, and O. Tengblad. *Chemically selective laser ion-source for the CERN-ISOLDE on-line mass separator facility.* Nuclear Instruments and Methods in Physics Research Section B: Beam Interactions with Materials and Atoms, 73(4):550 – 560, 1993. ISSN 0168-583X. doi:DOI: 10.1016/0168-583X(93)95839-W.

[Mit02] P. Mitra, G. Gangopadhyay, and B. Malakar. *Deformation constrained calculation for light nuclei in generalized hybrid derivative coupling model.* Physical Review C, 65(3):034329, 2002.

[Moe92] P. Moeller and J. R. Nix. *Nuclear pairing models.* Nuclear Physics A, 536(1):20 – 60, 1992. ISSN 0375-9474. doi:DOI: 10.1016/0375-9474(92)90244-E.

[Mol95] P. Moller, J. R. Nix, W. D. Myers, and W. J. Swiatecki. *Nuclear ground-state masses and deformations.* Atomic Data and Nuclear Data Tables, 59(2):185–381, 1995.

[Mye83] W.D. Myers and K.H. Schmidt. *An update on droplet-model charge distributions.* Nuclear Physics A, 410(1):61 – 73, 1983. ISSN 0375-9474. doi:DOI: 10.1016/0375-9474(83)90401-3.

[Neu81] R. Neugart. *Laser spectroscopy on mass-separated radioactive beams.* Nuclear Instruments and Methods in Physics Research, 186(1-2):165 – 175, 1981. ISSN 0167-5087. doi:DOI: 10.1016/0029-554X(81)90902-2.

[Ney05] G. Neyens, M. Kowalska, D. Yordanov, K. Blaum, P. Himpe, P. Lievens, S. Mallion, R. Neugart, N. Vermeulen, Y. Utsuno, and T. Otsuka. *Measurement of the spin and magnetic moment of ^{31}Mg: Evidence for a strongly deformed intruder ground state.* Physical Review Letters, 94(2):022501, 2005.

[Nil55] S. G. Nilsson. *Binding states of individual nucleons in strongly deformed nuclei.* Dan. Mat. Fys. Medd., 29(16), 1955.

[Nil69] S.G. Nilsson, C.F. Tsang, A. Sobiczewski, Z. Szymanski, S. Wycech, C. Gustafson, I.L Lamm, P. Moeller, and B. Nilsson. *On the nuclear structure and stability of heavy and superheavy elements.* Nuclear Physics A, 131(1):1 – 66, 1969. ISSN 0375-9474. doi:DOI: 10.1016/0375-9474(69)90809-4.

[Noe09] W. Noertershaeuser, D. Tiedemann, M. Žáková, Z. Andjelkovic, K. Blaum, M. L. Bissell, R. Cazan, G. W. F. Drake, Ch. Geppert, M. Kowalska, J. Kraemer, A. Krieger, R. Neugart, R. Sánchez, F. Schmidt-Kaler, Z.-C. Yan, D. T. Yordanov, and C. Zimmermann. *Nuclear charge radii of ^{7,9,10}Be and the one-neutron halo nucleus ^{11}Be.* Phys. Rev. Lett., 102(6):062503, Feb 2009. doi:10.1103/PhysRevLett.102.062503.

[Noe10] *Laser spectroscopy of radioactive isotopes.* http://www.gsi.de/forschung/ap/projects/laser/survey.html, 2010.

[Orm89] W. E. Ormand and B. A. Brown. *Empirical isospin non-conserving hamiltonians for shell-model calculations.* Nucl. Phys. A, 491:1, 1989.

[Ots01] T. Otsuka, R. Fujimoto, Y. Utsuno, B. A. Brown, M. Honma, and T. Mizusaki. *Magic numbers in exotic nuclei and spin-isospin properties of the NN interaction.* Physical Review Letters, 87:082502, 2001.

[Ots05] T. Otsuka, T. Suzuki, R. Fujimoto, H. Grawe, and Y. Akaishi. *Evolution of nuclear shells due to the tensor force.* Physical Review Letters, 95(23):232502, 2005.

[Oza06] A. Ozawa, K. Matsuta, T. Nagatomo, M. Mihara, K. Yamada, T. Yamaguchi, T. Ohtsubo, S. Momota, T. Izumikawa, T. Sumikama, Y. Nakashima, H. Fujiwara, S. Kumashiro, R. Matsumiya, M. Ota, D. Shinojima, and H. Tanaka. *Measurement of the spin and the magnetic moment of ^{23}Al.* Phys. Rev. C, 74:021301R, 2006.

[Per65] Julius Perel, Richard H. Vernon, and Howard L. Daley. *Measurement of cesium and rubidium charge-transfer cross sections.* Phys. Rev., 138(4A):A937–A945, May 1965. doi:10.1103/PhysRev.138.A937.

[Ple10] *Datenblatt Beschichtungen.* http://www.pleiger-laseroptik.de/pdf-Dateien/Datenblaetter202006.pdf, 2010.

[Pov06] B. Povh, K. Rith, C. Scholz, and F. Zetsche. *Teilchen und Kerne.* Springer, Berlin, 2006.

[Pri99] B. V. Pritychenko, T. Glasmacher, P. D. Cottle, M. Fauerbach, R. W. Ibbotson, K. W. Kemper, V. Maddalena, A. Navin, R. Ronningen, A. Sakharuk, H. Scheit, and V. G. Zelevinsky. *Role of intruder configurations in ^{26,28}Ne and ^{30,32}Mg.* Physics Letters B, 461(4):322 – 328, 1999. ISSN 0370-2693. doi:DOI: 10.1016/S0370-2693(99)00850-3.

[Rag89] P. Raghavan. *Table of nuclear moments.* Atomic Data and Nuclear Data Tables, 42(2):189–292, 1989.

[Ram01] S. Raman, C.W. Nestor Jr., and P. Tikkanen. *Transition probability from the ground to the first-excited 2+ state of even-even nuclides.* Atomic Data and Nuclear Data Tables, 78(1):1 – 128, 2001. ISSN 0092-640X. doi:DOI: 10.1006/adnd.2001.0858.

[Rav79] H. L. Ravn. *Experiments with intense secondary beams of radioactive ions.* Physics Reports, 54(3):201–259, 1979.

[Rei80] L. Von Reisky, J. Bonn, S.L. Kaufman, L. Kugler, E.-W. Otten, J.-M. Rodriguez-Giles, K.P.C. Spath, and D. Weskott. *An on-line mass separator for fission-produced alkali isotopes.* Nuclear Instruments and Methods, 172(3):423 – 430, 1980. ISSN 0029-554X. doi:DOI: 10.1016/0029-554X(80)90329-8.

[Rin96] P. Ring. *Relativistic mean field theory in finite nuclei.* Progress in Particle and Nuclear Physics, 37:193 – 263, 1996. ISSN 0146-6410. doi:DOI: 10.1016/0146-6410(96)00054-3.

[Rod10] D. Rodriguez, K. Blaum, W. Noertershaeuser, M. Ahammed, A. Algora, and G. Audi *et al. MATS and LASPEC: High-precision experiments using ion traps and lasers at FAIR.* Eur. Phys. J. Special Topics, 183:1, 2010.

[Sch00] F. Scheck. *Theoretische Physik 2.* Springer, Berlin, 2000.

[Sch08] F. Schwellnus, K. Blaum, C. Geppert, T. Gottwald, H. J. Kluge, C. Mattolat, W. Nortershauser, K. Wies, and K. Wendt. *The laser ion source and trap (LIST) - a highly selective ion source.* Nuclear Instruments and Methods in Physics Research Section B-Beam Interactions with Materials and Atoms, 266(19-20):4383–4386, 2008.

[Sie10] B. Sieber. *Aufbau und Test eines Detektorsystems zum Koinzidennachweis von Ionen und Photonen fuer die kollineare Laserspektroskopie am TRIGA-Forschungsreaktor.* Diplomarbeit, Johannes Gutenberg-Universitaet Mainz, 2010.

[Ste80] E. Stender, N. Trautmann, and G. Herrman. *Use of alkali halide clusters in a gas-jet recoil-transport system.* Radiochemical and Radioanalytical Letters, 42:291, 1980.

[Ste01a] D. A. Steck. *Rubidium 87 D line data.* http://steck.us/alkalidata/, 2001.

[Ste01b] P. Stevenson, M. R. Strayer, and J. Rikovska Stone. *Many-body perturbation calculation of spherical nuclei with a separable monopole interaction.* Phys. Rev. C, 63(5):054309, Apr 2001. doi:10.1103/PhysRevC.63.054309.

[Ste02] P. D. Stevenson, J. R. Stone, and M. R. Strayer. *Mean field calculation of Ne, Mg and Si nuclei at N=20 with the separable monopole interaction.* Physics Letters B, 545(3-4):291–297, 2002.

[Sug69] K. Sugimoto. *Magnetic moments and β-decay ft values of mirror nuclei.* Phys. Rev., 182:1051, 1969.

[Sug73] K. Sugimoto. *Proceedings of the international conference on nuclear moments and nuclear structure.* J. Phys. Soc. Jpn., 34, Supplement:197, 1973.

[Thi75] C. Thibault, R. Klapisch, C. Rigaud, A. M. Poskanzer, R. Prieels, L. Lessard, and W. Reisdorf. *Direct measurement of the masses of ^{11}Li and $^{26-32}Na$ with an on-line mass spectrometer.* Phys. Rev. C, 12(2):644–657, Aug 1975. doi: 10.1103/PhysRevC.12.644.

[Thu09] Th. Thuemmler, R. Marx, and Ch. Weinheimer. *Precision high voltage divider for the KATRIN experiment.* New. J. Phys., 11(103007), 2009.

[Uen96] H. Ueno, K. Asahi, H. Izumi, K. Nagata, H. Ogawa, A. Yoshimi, H. Sato, M. Adachi, Y. Hori, K. Mochinaga, H. Okuno, N. Aoi, M. Ishihara, A. Yoshida, G. Liu, T. Kubo, N. Fukunishi, T. Shimoda, H. Miyatake, M. Sasaki, T. Shirakura, N. Takahashi, S. Mitsuoka, and W.D. SchmidtOtt. *Magnetic moments of 17N and 17B.* Physical Review C, 53:21422151, 1996.

[Ure32] Harold C. Urey, F. G. Brickwedde, and G. M. Murphy. *A hydrogen isotope of mass 2 and its concentration.* Phys. Rev., 40(1):1–15, Apr 1932. doi:10.1103/PhysRev.40.1.

[Uts99] Yutaka Utsuno, Takaharu Otsuka, Takahiro Mizusaki, and Michio Honma. *Varying shell gap and deformation in $N \sim 20$ unstable nuclei studied by the monte carlo shell model.* Phys. Rev. C, 60(5):054315, Oct 1999. doi:10.1103/PhysRevC.60.054315.

[Uts05] Y. Utsuno. *Anomalous magnetic moment of ^9C and shell quenching in exotic nuclei.* Eur. Phys. J. A, 25:209, 2005.

[Vau72] D. Vautherin and D. M. Brink. *Hartree-fock calculations with skyrme's interaction. I. spherical nuclei.* Phys. Rev. C, 5(3):626–647, Mar 1972. doi:10.1103/PhysRevC.5.626.

[War90] E. K. Warburton, J. A. Becker, and B. A. Brown. *Mass systematics for A = 29-44 nuclei - the deformed A≈32 region.* Physical Review C, 41(3):1147–1166, 1990.

[War92] E. K. Warburton and B. A. Brown. *Effective interactions for the 0p1s 0d nuclear shell-model space.* Phys. Rev. C, 46:923, 1992.

[Wil71] R. L. Williams and L. Madansky. *B-13 nuclear magnetic dipole moment.* Physical Review C, 3(6):2149–2150, 1971.

[Wil80] B. H. Wildenthal and W. Chung. *Collapse of the conventional shell-model ordering in the very-neutron-rich isotopes of Na and Mg.* Phys. Rev. C, 22(5):2260–2262, Nov 1980. doi:10.1103/PhysRevC.22.2260.

[Wil84] B. H. Wildenthal. *Empirical strengths of spin operators in nuclei.* Progress in Particle and Nuclear Physics, 11:5 – 51, 1984. ISSN 0146-6410. doi:DOI: 10.1016/0146-6410(84)90011-5.

[Yor07a] D. T. Yordanov, M. Kowalska, K. Blaum, M. De Rydt, K. T. Flanagan, P. Lievens, R. Neugart, G. Neyens, and H. H. Stroke. *Spin and magnetic moment of ^{33}Mg: Evidence for a negative-parity intruder ground state.* Physical Review Letters, 99(21):212501, 2007.

[Yor07b] D.T. Yordanov. *From ^{27}Mg to ^{33}Mg: Transition to the Island of Inversion.* Dissertation, Katolieke Universiteit Leuven, 2007.

[Zhi06] Q. J. Zhi and Z. Z. Ren. *Systematic calculations on the ground state properties of Mg isotopes by the macroscopic-microscopic model.* Physics Letters B, 638(2-3):166–170, 2006.

Publications

1. D. Rodriguez, K. Blaum, W. Nörtershäuser, M. Ahammed, A. Algora, G. Audi, J. Äystö, D. Beck, M. Bender, J. Billowes, M. Block, C. Böhm, G. Bollen, M. Brodeur, T. Brunner, B.A. Bushaw, R.B. Cakirli, P. Campbell, D. Cano-Ott, G. Cortes, J.R. Crespo Lopez-Urrutia, P. Das, A. Dax, A. De, P. Delheij, T. Dickel, J. Dilling, K. Eberhardt, S. Eliseev, S. Tenauer, K.T. Flanagan, R. Ferrer, J.-E. Garca-Ramos, E. Gartzke, H. Geissel, S. George, C. Geppert, M.B. Gomez-Hornillos, Y. Gusev, D. Habs, P.-H. Heenen, S. Heinz, F. Herfurth, A. Herlert, M. Hobein, G. Huber, M. Huyse, C. Jesch, A. Jokinen, O. Kester, J. Ketelaer, V. Kolhinen, I. Koudriavtsev, M. Kowalska, J. Krämer, S. Kreim, A. Krieger, T. Kühl, A.M. Lallena, A. Lapierre, F. Le Blanc, Y.A. Litvinov, D. Lunney, T. Martinez, G. Marx, M. Matos, E. Minaya-Ramirez, I. Moore, S. Nagy, S. Naimi, D. Neidherr, D. Nesterenko, G. Neyens, Y.N. Novikov, M. Petrick, W.R. Pla, A. Popov, W. Quint, A. Ray, P.-G. Reinhard, J. Repp, C. Roux, B. Rubio, R. Sanchez, B. Schabinger, C. Scheidenberger, D. Schneider, R. Schuch, S. Schwarz, L. Schweikhard, M. Seliverstov, A. Solders, M. Suhonen, J. Szerypo, J.L. Tain, P.G. Thirolf, J. Ullrich, P. Van Duppen, A. Vasiliev, G. Vorobjev, C. Weber, K. Wendt, M. Winkler, D. Yordanov and F. Ziegler MATS and LaSpec: High-precision experiments using ion traps and lasers at FAIR *European Physical Journal, Special Topics* 183, 1-123 (2010)

2. B. Cheal, E. Mane, J. Billowes, M. L. Bissell, K. Blaum, B. A. Brown, F. C. Charlwood, K. T. Flanagan, D. H. Forest, C. Geppert, M. Honma, A. Jokinen, M. Kowalska, A. Krieger, J. Krämer, I. D. Moore, R. Neugart, G. Neyens, W. Nörtershäuser, M. Schug, H. H. Stroke, P. Vingerhoets, D. T. Yordanov, and M. Zakova Nuclear Spins and Moments of Ga Isotopes Reveal Sudden Structural Changes between N =40 and N =50 *Physical Review Letters*, 104, 252502 (2010)

3. M. Zakova, Z. Andjelkovic, M. L. Bissell, K. Blaum, G. W. F. Drake, C. Geppert, M. Kowalska, J. Krämer, A. Krieger, T. Neff, R. Neugart, M. Lochmann, R. Sanchez, F. Schmidt-Kaler, D. Tiedemann, Z.-C. Yan, D. T. Yordanov, C. Zimmermann, and W. Nörtershäuser. Isotope shift measurements in the 2s1/2 to 2p3/2 transition of Be+ and extraction of the nuclear charge radii for 7,10,11Be. *Journal of Physics G-Nuclear and Particle Physics*, 37:055107, 2010.

4. M. Eibach, T. Beyer, K. Blaum, M. Block, K. Eberhardt, F. Herfurth, C. Geppert, J. Ketelaer, J. Ketter, J. Krämer, A. Krieger, K. Knuth, S. Nagy, W. Nörtershäuser, and C. Smorra. Transport of fission products with a helium gas-jet at Triga-Spec. *Nuclear Instruments and Methods in Physics Research A*, 613:226–231, 2010.

5. K. T. Flanagan, P. Vingerhoets, M. Avgoulea, J. Billowes, M. L. Bissell, K. Blaum, B. Cheal, M. De Rydt, V. N. Fedosseev, D. H. Forest, C. Geppert, U. Koster, M. Kowalska, J. Krämer, K. L. Kratz, A. Krieger, E. Mane, B. A. Marsh, T. Materna, L. Mathieu, P. L. Molkanov, R. Neugart, G. Neyens, W. Nörtershäuser, M. D. Seliverstov, O. Serot, M. Schug, M. A. Sjoedin, J. R. Stone, N. J. Stone, H. H. Stroke, G. Tungate, D. T. Yordanov, and Y. M. Volkov. Nuclear spins and magnetic moments of Cu-71,Cu-73,Cu-75: Inversion of π 2p(3/2) and π 1f(5/2) levels in Cu-75. *Physical Review Letters*, 103(14):142501, 2009.

6. J. Krämer, K. Blaum, M. De Rydt, K.T. Flanagan, C. Geppert, M. Kowalska, P. Lievens, R. Neugart, G. Neyens, W. Nörtershäuser, H.H. Stroke, P. Vingerhoets, and D.T. Yor-

danov. Nuclear ground-state spin and magnetic moment of ^{21}Mg. *Physics Letters B*, 678:465–469, 2009.

7. W. Nörtershäuser, D. Tiedemann, M. Zakova, Z. Andjelkovic, K. Blaum, M. L. Bissell, R. Cazan, G. W. F. Drake, C. Geppert, M. Kowalska, J. Krämer, A. Krieger, R. Neugart, R. Sanchez, F. Schmidt-Kaler, Z. C. Yan, D. T. Yordanov, and C. Zimmermann. Nuclear charge radii of Be-7,Be-9,Be-10 and the one-neutron halo nucleus Be-11. *Physical Review Letters*, 102(6):062503, 2009.

8. R. Sanchez, M. Zakova, C. Geppert, J. Krämer, A. Krieger, D. Tiedemann, and W. Nörtershäuser. Frequency-comb-based measurements of lithium and beryllium isotopes for nuclear structure studies. *Canadian Journal of Physics*, 87:825–834, 2009.

9. R. Sanchez, M. Zakova, Z. Andjelkovic, B. Bushaw, K. Dasgupta, G. Ewald, C. Geppert, H.-J. Kluge, J. Krämer, M. Nothhelfer, D. Tiedemann, D. Winters, and W. Nörtershäuser. Absolute frequency measurements on the 2s→3s transition of lithium-6,7. *New Journal of Physics*, 11:073016, 2009.

10. J. Ketelaer, J. Krämer, D. Beck, K. Blaum, M. Block, K. Eberhardt, G. Eitel, R. Ferrer, C. Geppert, S. George, F. Herfurth, J. Ketter, Sz. Nagy, D. Neidherr, R. Neugart, W. Nörtershäuser, J. Repp, C. Smorra, N. Trautmann, and C. Weber. Triga-spec: A setup for mass spectrometry and laser spectroscopy at the research reactor Triga mainz. *Nuclear Instruments and Methods in Physics Research A*, 594:162–177, 2008.